Search for Very High Energy Gamma Radiation From the Starburst Galaxy IC 342

Andrew Merriman B.Sc.

Presented for the award of

Master of Science

Galway-Mayo Institute of Technology

Supervisor: Dr. Patrick Moriarty

Submitted to the Higher Education and Training Awards Council

July, 2010

To Mum, Dad, Niamh, Gran and Grandad.

Search for Very High Energy Gamma Radiation From the Starburst Galaxy IC 342

Andrew Merriman

Abstract

This thesis describes a search for very high energy (VHE) gamma-ray emission from the starburst galaxy IC 342. The analysis was based on data from the 2003 − 2004 observing season recorded using the Whipple 10-metre imaging atmospheric Cherenkov telescope located on Mount Hopkins in southern Arizona. IC 342 may be classed as a non-blazar type galaxy and to date only a few such galaxies (M 87, Cen A, M 82 and NGC 253) have been detected as VHE gamma-ray sources. Analysis of approximately 24 hours of good quality IC 342 data, consisting entirely of ON/OFF observations, was carried out using a number of methods (standard Supercuts, optimised Supercuts, scaled optimised Supercuts and the multivariate kernel analysis technique). No evidence for TeV gamma-ray emission from IC 342 was found. The significance was 0.6 σ with a nominal rate of 0.04 $\pm$ 0.06 gamma rays per minute. The flux upper limit above 600 GeV (at 99.9 % confidence) was determined to be 5.5 $\times$ 10^{-8} m^{-2} s^{-1}, corresponding to 8 % of the Crab Nebula flux in the same energy range.

Acknowledgements

The completion of this thesis marks the end of a journey in my life, opens up new paths and new beginnings, and there are several people whom I would like to thank for this.

Firstly I wish to thank Dr. Pat Moriarty, my supervisor, whose guidance, direction and patience is especially appreciated. My sincerest thanks to you for your continuing support and your tireless work in helping bringing this thesis to completion. Also, I would like to give grateful thanks to Dr. Malachy Thompson, for without his kindness this research may never have come to pass.

I would also like to mention the friendship of many others at G.M.I.T. who were also carrying out research during my time here: Mark, Lisa, Joanne, Brian, Karen, the two Gavins, the two Brendans, Nóirín, Linda, Magsie, Deirdre, Victor and Gary. My warmest and deepest thanks to you all.

Part of my research was carried out at UCD and I would like to express my thanks to my colleagues whom I worked with there, particularly Dr. John Quinn, James and Andrew for their hospitality.

I would like to thank the VERITAS Collaboration for making the data available for this research and for all the technical support at the Whipple Observatory.

The research project was made possible through the award of a grant under the programme for Technological Sector Research: STRAND 1 (Post-Graduate R&D Skills Programme), a part of the National Development Plan, and this funding is gratefully acknowledged.

Finally, I would like to thank my Family, who are forever a source of love and happiness, and whose continued support during my time away from home helped me to accomplish this wonderful feat. My forever love to you all.

Contents

List of Figures

List of Tables

Chapter 1

The High-Energy Universe and Charged Particles

1.1 Introduction

Cosmic rays are highly energetic charged particles which are created in extreme environments in the universe. They were first discovered in 1912 by Victor Hess, who noticed that an electroscope discharged more rapidly with increasing altitude. Since cosmic rays are charged particles, their trajectories are influenced by interstellar magnetic fields throughout space and thus their arrival path to Earth may not have been their original destination path from their source. As a result, cosmic rays arrive at Earth from random directions with little or no information as to their point origin (although the very highest energy cosmic rays should be virtually undeflected magnetic fields, no unambiguous source has yet been identified). Although the very highest energy cosmic rays are deflected very little by magnetic fields, so far there is no clear indication of their origin.

High-energy electromagnetic radiation does not suffer from the same influences. As electromagnetic radiation is uncharged, the trajectories are not distorted by interstellar magnetic fields and therefore any electromagnetic radiation detected on Earth may be projected back to its point of origin. Gamma radiation is the term used to describe the range of electromagnetic radiation above 0.1 MeV (frequency $> 10^{19}$ Hz and wavelength $< 10^{-11}$ m) and it is the very high energy (VHE, $E \sim 100$ GeV $-$ 100 TeV) gamma-ray range that is of interest in this thesis.

Region	Wavelength (m)	Frequency (Hz)	Photon Energy (eV)
Radio	> 0.1	$< 3 \times 10^{9}$	$< 10^{-5}$
Microwave	$0.1 - 1 \times 10^{-4}$	$3 \times 10^{9} - 3 \times 10^{12}$	$10^{-5} - 0.01$
Infrared	$1 \times 10^{-4} - 7.5 \times 10^{-7}$	$3 \times 10^{12} - 4.3 \times 10^{14}$	$0.01 - 2$
Visible	$7.5 \times 10^{-7} - 3.8 \times 10^{-7}$	$4.3 \times 10^{14} - 7.5 \times 10^{14}$	$2 - 3$
Ultra Violet	$3.8 \times 10^{-7} - 1 \times 10^{-9}$	$7.5 \times 10^{14} - 3 \times 10^{17}$	$3 - 1 \times 10^{3}$
X-Ray	$1 \times 10^{-9} - 1 \times 10^{-12}$	$3 \times 10^{17} - 3 \times 10^{19}$	$1 \times 10^{3} - 1 \times 10^{5}$
Gamma Ray	$< 10^{-12}$	$> 3 \times 10^{19}$	$> 10^{5}$

Table 1.1: Regions of the electromagnetic spectrum.

Whilst low to medium energy gamma rays may be detected by satellites orbiting the Earth, VHE gamma rays typically pass through satellites undetected (though the Large Area Telescope on board the Fermi satellite is capable of detecting gamma rays up to ~ 300 GeV (Fermi Webpage, 2008)). Furthermore, the flux of VHE or TeV gamma rays is too low to be sampled effectively by orbiting instruments, so we must endeavour instead to sample VHE gamma rays at the Earth's surface. Unfortunately gamma rays cannot be directly detected at the Earth's surface because they interact with the atmosphere. Were it not for this interaction in the Earth's atmosphere, shielding us from the TeV gamma rays, this ionising energy would reach ground level and seriously affect life on Earth. Although direct detection is not feasible, it is possible to detect VHE gamma rays indirectly. The interaction of gamma rays with the Earth's atmosphere and the methods used to detect them will be discussed in Chapter 2.

1.2 Gamma-Ray Production Processes

Many astrophysical systems emit radiation that is thermal in origin, described by the Planck radiation formula:

$$I'(\lambda, T) = \frac{2hc^2}{\lambda^5} \frac{1}{e^{hc/\lambda kT} - 1} \tag{1.1}$$

where I' is the energy density at wavelength λ for a blackbody at temperature

T, $h = 6.626 \times 10^{-34}$ J.s is Planck's constant, $c = 2.998 \times 10^{8}$ m s^{-1} is the speed of light and $k = 1.381 \times 10^{-23}$ J K^{-1} is Boltzmann's constant. However, thermal processes cannot produce VHE gamma rays. Wien's displacement law, which derives from the Planck radiation formula, gives

$$\lambda_m T = \alpha = 2.898 \times 10^{-3} \text{ K.m, constant} \tag{1.2}$$

where λ_m is the wavelength of peak emission for a blackbody at temperature T. Since photon energy is given by

$$E = \frac{hc}{\lambda} \tag{1.3}$$

the photon energy (E_m) at the peak of the blackbody spectrum at temperature T may be written as:

$$E_m = \frac{hc}{\lambda_m} = \frac{hcT}{\alpha} \propto T \tag{1.4}$$

so

$$E_m \text{ (J)} = 6.859 \times 10^{-23} \; T \text{ (K)} \tag{1.5}$$

or

$$E_m \text{ (eV)} = 4.281 \times 10^{-4} \; T \text{ (K)} \tag{1.6}$$

Therefore, for an astrophysical system with temperature T even as high as 10^7K, the peak thermal photon energy will be less than 5 keV; the thermal flux drops rapidly at higher energy: at 100 keV, it is less than 10^{-35} of the flux at E_m. We must therefore look to *non*-thermal processes for the origin of radiation in the GeV $-$ TeV range.

VHE gamma rays may be expected to originate from regions where there is evidence of energetic charged particles or strong magnetic fields. Non-thermal processes which can give rise to electromagnetic radiation include acceleration

Energy Range (eV)	Energy Band	Energy Type	Detection Technique
$0.1 \times 10^6 - 3 \times 10^7$	MeV	Low/Medium Energy	Satellite
$3 \times 10^7 - 1 \times 10^8$	MeV − GeV	High Energy	Satellite
$1 \times 10^8 - 1 \times 10^{11}$	GeV − TeV	Very High Energy	Ground-Based
$> 10^{11}$	> TeV	Ultra High Energy	Ground-Based

Table 1.2: The gamma-ray energy range in the electromagnetic spectrum. Adapted from Weekes (2003).

of charged particles, collisions of high-energy particles, radioactive decay of nuclei or particles, and particle-antiparticle annihilation. In this chapter, the production processes of VHE gamma rays are described and some potential astrophysical sources of such radiation are discussed.

1.2.1 Synchrotron Radiation

When a charged particle accelerates at relativistic velocity due to spiralling around a magnetic field, the electromagnetic energy emitted is called synchrotron radiation (see Figure 1.1). The force felt by a charged particle in a magnetic field is perpendicular to the direction of the magnetic field and to the direction of the charged particle's velocity. This causes the charged particle to spiral around the direction of the field and since circular motion represents acceleration, i.e., a continuous change in velocity, the charged particle radiates photons of a characteristic energy corresponding to the radius of a circle. A continuous spectrum of polarised radiation perpendicular to the direction of the magnetic field is emitted. The shape of this continuous spectrum is dependent on the strength of the magnetic field and the energy of the charged particle. The resulting synchrotron radiation is emitted in a collimated beam in the direction of the charged particle motion, a process referred to as relativistic beaming. The emission is beamed tangentially along the instantaneous direction of motion of the charged particle. The opening angle of the collimated beam is determined by the charged particle mass, m_p, and charged particle energy, E_p, by the following relationship:

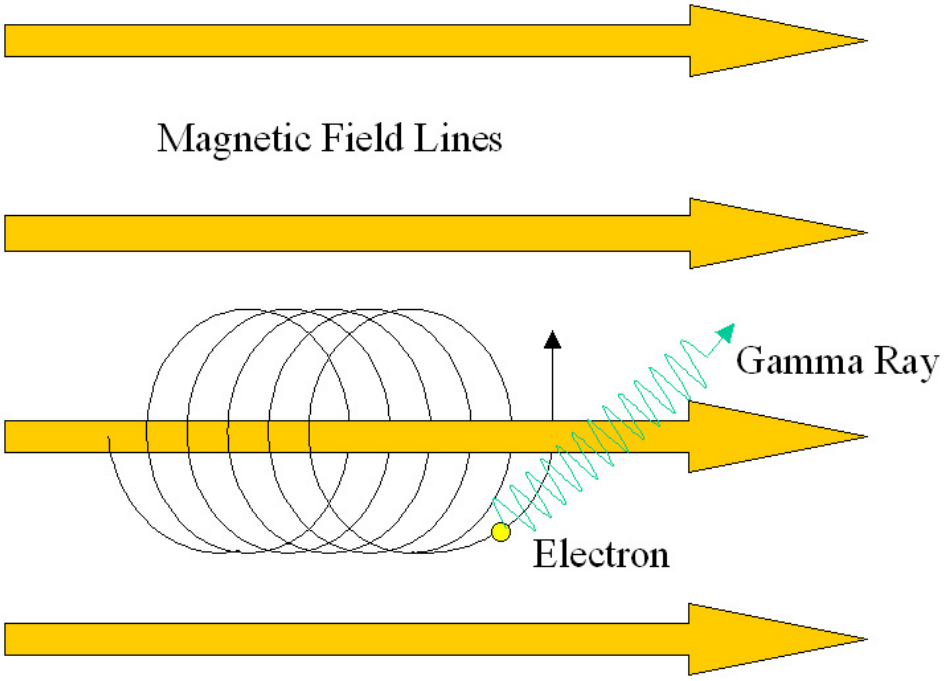

Figure 1.1: An illustration of synchrotron radiation, where a charged particle is spiralling around magnetic field lines, emitting gamma rays.

$$\theta = \frac{m_p c^2}{E_p} \tag{1.7}$$

Thus, the higher the energy of the charged particle, the more collimated the beam. It is the high degree of polarisation and the continuous spectrum of frequency which make synchrotron radiation easily determinable. Either a charged particle of relativistic speeds or a very intense magnetic field must be present to produce VHE gamma rays by synchrotron radiation alone. However, the observation of synchrotron radiation in other regions of the electromagnetic spectrum indicates the presence of relativistic electrons which may produce VHE gamma rays by inverse-Compton scattering and Bremsstrahlung.

1.2.2 Inverse-Compton Scattering

The Compton effect is the scattering of a high-energy photon with a low-energy charged particle, for example, an electron, in which there is a transfer of energy from the photon to the electron. This energy loss by the photon corresponds

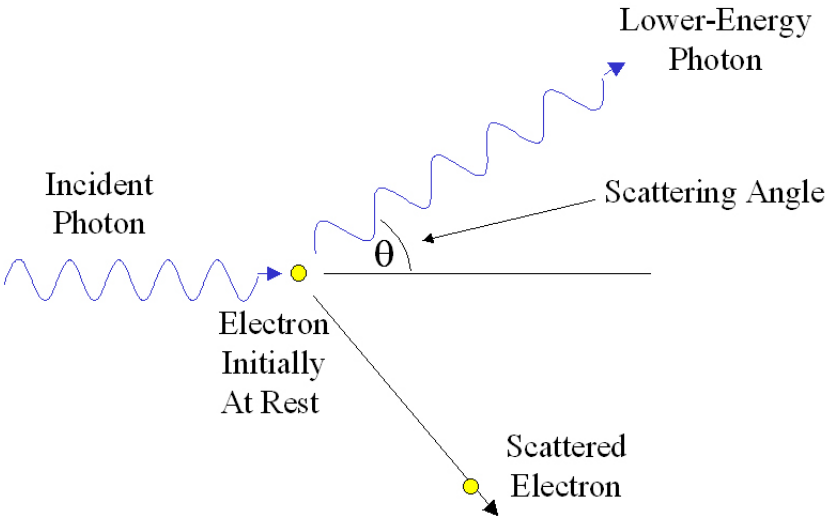

Figure 1.2: Compton scattering. During collision, a photon imparts some of its energy to a charged particle (assumed to be initially at rest).

to an increase in wavelength, $\Delta\lambda$, which is dependent on θ, the collision angle between the electron and the photon (see Figure 1.2):

$$\Delta\lambda = \frac{h}{m_e c}(1 - \cos\theta) \tag{1.8}$$

The energy transfer to the electron therefore depends on the scattering angle of the photon. Maximum energy transfer occurs when the photon direction is reversed after collision, whilst minimum energy is transferred when the scattering angle is 90°. The Compton effect is shown in Figure 1.2 for a photon incident on an electron at rest.

Inverse-Compton scattering is the reverse process, in which a high-energy charged particle, e.g., an electron, collides with a low-energy photon. During the collision the electron transfers some of its energy to the photon, depending on the scattering angle of the collision. As a result, the photon energy will increase and the electron lose energy. This is shown in Figure 1.3. In the collision between a relativistic electron with energy $E_e = \gamma m_e c^2$ (where $\gamma = \frac{1}{\sqrt{1-v^2/c^2}}$ for electron velocity v) and a photon of energy $\varepsilon = h\nu$, the increase in photon energy depends on γ. For sufficiently high electron energy, the process

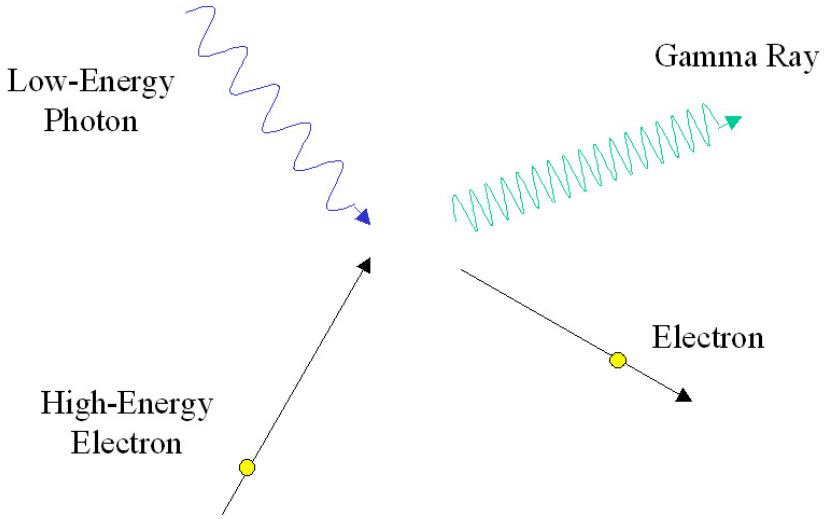

Figure 1.3: Inverse-Compton scattering. During collision, a high-energy charged particle imparts energy to a low-energy photon creating a higher-energy photon.

can turn a radio photon into a gamma-ray photon. Inverse-Compton scattering can occur where there is a high density of high-energy charged particles and a large supply of low-energy photons. The low-energy photons may belong to the cosmic background radiation ($T = 2.7$ K), which has an energy density of 0.4×10^{-13} J.m^{-3}. Alternatively, as mentioned above, the low-energy photons may be the synchrotron photons emitted by the energetic electron population itself (synchrotron self-Compton).

The energy transferred to the photon depends on the scattering angle at which the electron and photon meet. For maximum energy transfer (E_{max}), the particles must meet head-on, reversing the photon direction in the collision, while minimum energy (E_{min}) will be transferred when the scattering angle is 90°.

The cross-section for electron-photon interaction is given by the Klein-Nishina formula:

$$\sigma_{KN} = \pi r_e^2 \frac{1}{\eta}\left[\left(1 - \frac{2(\eta+1)}{\eta^2}\right)\ln(2\eta+1) + \frac{1}{2} + \frac{4}{\eta} - \frac{1}{2(2\eta+1)^2}\right] \qquad (1.9)$$

where $\eta = \gamma\varepsilon/m_e c$, and $r_e = 2.818 \times 10^{-15}$ m is the classical electron radius.

For low-energy collisions, the cross-section is simply the Thomson cross-section $\sigma_T = \frac{8}{3}\pi r_e^2$, independent of energy. However, for very high energy electron-photon interactions ($\varepsilon >> m_e c^2$) the Klein-Nishina formula reduces to:

$$\sigma \approx \frac{3}{8}\sigma_T \frac{m_e c^2}{\gamma\varepsilon}\left[\ln\left(\frac{2\gamma\varepsilon}{m_e c^2}\right) + \frac{1}{2}\right] \propto \frac{\ln E_e}{E_e} \tag{1.10}$$

so that the interaction probability decreases at higher energies. In this regime, the electron energy loss through scattering becomes independent of the incident photon energy, and the scattered photon energies range from

$$E_{min} \approx \frac{m_e c^2}{4\gamma} \tag{1.11}$$

to

$$E_{max} \approx E_e = \gamma m_e c^2 \tag{1.12}$$

Using a power-law energy distribution for the electrons, $dN_e/dE_e \propto E_e^{-\alpha}$, the inverse-Compton spectrum takes the form of a two-component distribution peaking between the Thomson and Klein-Nishina regimes.

1.2.3 Bremsstrahlung

When a charged particle is decelerated in the Coulomb field of a nucleus it emits photons. Figure 1.4 illustrates this process. The energy lost by the charged particle generates the photons. This process is known as Bremsstrahlung (German for "braking radiation"). The rapid deceleration of a high-energy charged particle can impart a large portion of the particle energy to the radiated photon. Bremsstrahlung photons generated by cosmic-ray electrons can have photon energy in the gamma-ray range of the electromagnetic spectrum. Bremsstrahlung photons generated by cosmic-ray electrons will have a power-law spectral distribution similar to the energy distribution of the electrons. Thus the identification

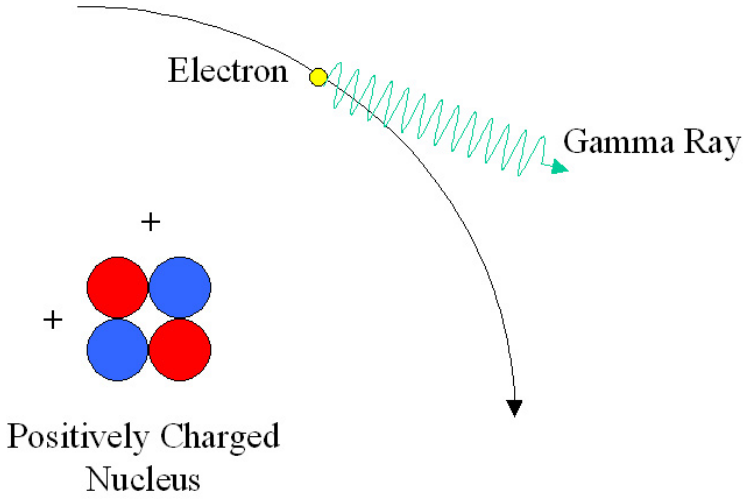

Figure 1.4: The generation of a gamma-ray photon by the deceleration of a charged particle in the electromagnetic field of a nucleus. This process is known as Bremsstrahlung or "braking radiation".

of Bremsstrahlung photons by their spectral distribution could determine the sites of cosmic-ray electron production. The development of electromagnetic cascades in the Earth's upper atmosphere, an important element in ground-based gamma-ray detection which will be discussed in Section 2.3.1, also depends heavily on the Bremsstrahlung process.

1.2.4 Particle Decay

Gamma rays can also be generated as a result of proton interactions. A very common interaction in high-energy astrophysical systems is the collision of cosmic-ray protons with stationary hydrogen gas. This proton-proton interaction can produce unstable by-products including particles such as neutral pions, π^0. The neutral pion decays with a half-life of 0.83 $\times 10^{-16}$ s into two gamma rays:

$$p + p \rightarrow \pi^0 \ / \ \pi^+ \ / \ \pi^- + \text{ other fragments} \tag{1.13}$$

$$\pi^0 \rightarrow \gamma + \gamma \tag{1.14}$$

When the neutral pion decays at rest, each gamma ray has an energy of

$E_\gamma = \frac{1}{2} m_\pi c^2 = 67.5$ MeV, where m_π is the rest mass of the neutral pion. However, neutral pions are rarely created at rest, and since they suffer no energy loss by ionisation, they usually decay in flight. TeV gamma rays can be produced by neutral pions travelling at relativistic speeds. The decay of pions is also important for the development of hadronic cosmic-ray showers in the atmosphere (see Section 2.3.2).

1.2.5 Particle-Antiparticle Annihilation

When a particle and its antiparticle interact, they annihilate each other and the energy may be emitted as two gamma-ray photons. For example, an interaction between an electron, e^-, and a positron, e^+, will yield:

$$e^- + e^+ \rightarrow \gamma + \gamma \tag{1.15}$$

The rest mass of an electron is 0.511 MeV. Therefore the energy of each emitted gamma ray occurring from an electron-positron annihilation at rest will be 0.511 MeV. Annihilation interactions of more massive charged particles yield higher energies.

1.2.6 Dark Matter Annihilation

Dark matter, which accounts for about 22 % of the content of the Universe, is theorised to be made up of hypothetical particles called weakly interacting massive particles (WIMPs). Such particles are predicted by supersymmetry theories. The lightest supersymmetric WIMP is the neutralino, which is its own antiparticle. Thus, two neutralinos can mutually annihilate and release secondary particles including quarks, leptons and bosons as well as gamma rays. Such annihilations would create characteristic gamma rays, which in principle could be distinguished from gamma rays from other sources. However, no convincing evidence for gamma rays from dark matter annihilation has so far been obtained.

1.3 Sources and Potential Sources of VHE Gamma Radiation

VHE gamma rays are generated in the most extreme astrophysical systems in the universe. The complex structures of some of these dynamic objects such as supernovae and active galactic nuclei, which can generate high-energy charged particles, are not reproducible in laboratories on Earth. Although the LHC (large hadron collider) at CERN is now accelerating protons up to 7 TeV (CERN Webpage, 2010), this is still far below the energies reached in some astrophysical contexts: cosmic-ray particles with energies as high as 10^8 TeV have been recorded (Andringa and The Pierre Auger Collaboration, 2010).

1.3.1 Supernova Remnants

When a sufficiently massive star reaches the end of its life, it undergoes a violent explosion known as a supernova, releasing energy $\sim 10^{44}$ J. Supernovae occur, on average, roughly every 30 years within our Galaxy. The duration of the explosion can be in the order of seconds, expelling particles and other material into space at high velocities, up to one-tenth the speed of light. The gaseous cloud comprising the constituents of the former star is termed a supernova remnant (SNR). In such systems, up to 10 % of the energy released may go into particle acceleration through shock acceleration. SNRs can be categorised into three types; shell-type, plerionic and composite.

If the supernova remnant displays emission from a spherical shell and has no central power source, the remnant is shell-type. Most of the radiation from shell-type remnants comes from shock interactions of the filamentary shell with the interstellar medium into which it expands. VHE gamma-ray emission could be produced as a result of acceleration in the supernova shock front of hadrons, which produce neutral pions in collisions, with the neutral pions then decaying to gamma rays.

A supernova remnant which displays emission from a filled centre is known as a plerion. Plerions are thought to be powered by a central spinning neutron star

(a pulsar) or a black hole (depending on the mass of the original star) which is surrounded by a magnetically supported non-thermal plasma. Relativistic electrons are produced by shock acceleration in the pulsar-driven wind and lose energy via synchrotron radiation, with inverse-Compton scattering boosting the radiation to VHE gamma rays. In a plerion such as the Crab Nebula, the high-energy electrons emit radio to X-ray synchrotron radiation as they travel through the magnetic field of the inner nebula with electrons being continually injected into the nebula from the pulsar. The Crab Nebula was the first gamma-ray source reliably detected at TeV energies (Weekes et al., 1989) and has also been detected by other experiments including HEGRA (Lucarelli et al., 2003). This source is now regarded as a standard candle for TeV observations, since its TeV emission appears to be steady.

Composite SNRs are a cross between shell-type and plerion remnants. They may appear shell-like, plerionic or both depending on the energy range observed.

1.3.2 Pulsars

Pulsars are rapidly rotating, highly magnetised neutron stars. Electrons travelling along the strong dipole magnetic field can emit synchrotron radiation along its axis of the dipole, which is inclined with respect to the rotational axis.

The power to produce emission from pulsars is generated by the slowing down of the spinning neutron star. It was shown by Pacini (1967), Gold (1968) and Goldreich and Julian (1969) that if a spinning neutron star were to exist in a vacuum, an intense surface electric field would exist parallel to the magnetic field lines ejecting charged particles from the neutron star surface and quickly forming a co-rotating plasma, called the magnetosphere, distributed in such a way as to balance the electric and magnetic fields. Such a co-rotating plasma is not completely possible since portions of the plasma, beyond what is known as the light cylinder, would be forced to move faster than the speed of light. The magnetic field lines become open at this point and particles can be ejected from the magnetosphere. Under certain circumstances, charges cannot be easily

replenished from the surface of the neutron star and the outflow of particles from the system can lead to a deficit in the charge density in certain regions of the magnetosphere, just above the surface of the neutron star at the pole (the polar cap) and along the edge of the closed magnetosphere near to the light cylinder (the outer gap). In these regions, the electric field is not constrained by the plasma to be perpendicular to the magnetic field and particle acceleration can occur. The polar cap model (Sturrock, 1971; Ruderman and Sutherland, 1975), the outer gap model (Cheng et al., 1986; Romani, 1996; Hirotani, 2001) and the slot-gap model (Muslimov and Harding, 2004; Harding et al., 2008) are the three main emission mechanisms proposed for pulsars.

1.3.3 Pulsar Wind Nebulae

Pulsars can drive powerful winds of highly relativistic particles. Confinement of these winds leads to the formation of strong shocks, produced in collisions of the relativistic winds with the surrounding interstellar gas, which may accelerate particles to $\sim$ PeV energies. Evidence for high-energy electrons in pulsar wind nebulae (PWNe) is provided by the observation of both synchrotron emission in the radio range through to the high-energy gamma-ray range and inverse-Compton radiation in the high-energy and VHE gamma-ray ranges. The synchrotron photon energy flux of the highly relativistic PWN electron population is proportional to both the total number of electrons and the magnetic field energy density. As a result of interactions of relativistic particles with the magnetic field and low-energy synchrotron radiation, the non-thermal gamma radiation (up to $\sim$ 100 TeV) is produced by low-energy processes. The ratio of X-ray to gamma-ray emission is then related to the magnetic field in the pulsar wind nebula. Given the general difficulty of estimating the magnetic field in such objects, it is hard to probe the spatial and energy distributions of the accelerated particles with X-ray observations alone. Measurements of high-energy gamma-ray radiation resulting from inverse-Compton scattering have a considerable advantage in that they provide a direct view of the parent par-

ticle population if the target photon fields are spatially uniform and have a well-known density.

It was recently found by H.E.S.S. that (on a statistical basis) pulsars with high spin-down energy-loss rates are accompanied by VHE emission. With the increasing number of detections of PWNe and PWN candidates powered by high spin-down flux pulsars, VHE gamma-rays are likely to be a useful tool for discovering more of these types of objects (Aharonian et al., 2007).

The best-studied example of a PWN is the Crab Nebula, which exhibits strong non-thermal emission across most of the electromagnetic spectrum from radio to > 50 TeV gamma-rays (Hillas et al., 1998; Tanimori et al., 1998; Aharonian et al., 2004).

1.3.4 Binary Systems and Microquasars

Binary systems in which a dense, compact, collapsed object (a neutron star or a black hole) is tightly orbited by a companion star are good candidates for VHE gamma-ray emission. The intense gravity of the compact object pulls matter from the companion star to form an accretion disk around the compact object, with X-rays originating from the inner region of the accretion disk. Such X-ray binaries are often classified as low-mass X-ray binaries (LMXBs) or high-mass X-ray binaries (HMXBs) depending on the mass of the companion star. VHE gamma rays could be generated if charged particles are accelerated to high energies in shock fronts arising from interaction between the intense stellar winds of the compact object and companion star or from interactions of the stellar winds with the accretion disc.

Some X-ray binary systems are observed to have collimated jets. Black-hole X-ray binaries with relativistic jets mimic (on a much smaller scale) many of the phenomena seen in quasars and are thus often called microquasars. The key difference is the distinct order of magnitude of the most significant parameters, especially the mass of the compact object (Paredes, 2005). These parameter differences are summarised in Table 1.3. The presence of relativistic jets, indi-

cated by radio observations of microquasars, would suggest that particles can be accelerated to high energies, similar to those observed in AGN.

To date, VHE emission has been detected from four binary systems (all of them involving a compact object and a massive companion star): LS 5039, LS I +61 303, PSR B1259−63 and Cyg X-1. LS 5039 was first identified as a VHE emitter by the H.E.S.S. Collaboration (Aharonian et al., 2005a). Although this object is usually considered a microquasar, the jet is weak, and the VHE emission is modulated at the orbital period suggesting that this emission is not associated with the jet (Aharonian et al., 2006a). The VERITAS Collaboration and the MAGIC Collaboration discovered VHE gamma-ray emission from LS I +61 303 (Acciari et al., 2008; Albert et al., 2006a). The emission is highest close to apastron, when the compact object is furthest from the Be companion star, and is not detected at periastron. LS I +61 303 was originally thought to be a microquasar but the nature of the compact object is not at all clear. In the case of PSR B1259−63 (Aharonian et al., 2005c), detected at VHE energies by the H.E.S.S. group, the compact object is known to be a pulsar with a period of 47.7 ms orbiting a Be star in a highly eccentric 3.5 yr orbit (Manchester et al., 1995). Cyg X-1 is a HMXB in which a blue supergiant star orbits a putative black hole. The MAGIC Collaboration reported VHE emission from Cyg X-1 (Albert et al., 2007), although the signal was detected only in one 79-minute interval and has not been confirmed by other instruments.

In addition to these sources, a fifth object, HESS J0632+057, may also be an example of this class of "gamma-ray binaries". This object is one of only two unidentified VHE gamma-ray point sources and its VHE emission has been shown to be variable (Acciari et al., 2009b). It is possibly associated with a massive Be star (MWC 148) and may resemble LS I +61 303 or LS 5039.

For all of these systems, it seems likely that the VHE emission arises from mechanisms similar to those operating in PWNe rather than being associated with any jet features.

Feature	Quasars	Microquasars
Black-hole mass	Several million solar masses	Few solar masses
Accretion-disk size	$\sim 10^9$ km	$\sim 10^3$ km
Mean temperature of the accretion disk	Several thousand degrees	Several million degrees
Characteristic wavelength of the disk radiation	UV and optical	X-rays to gamma rays
Distance travelled by jets	Millions of light-years	Few light-years

Table 1.3: Some differing parameters between quasars and microquasars. Adapted from Kaufman Bernadó (2004).

1.3.5 Active Galactic Nuclei

Active galactic nuclei (AGN) are galaxies with a central unresolved nucleus which is much brighter than the rest of the galaxy. The emission is spread widely across the electromagnetic spectrum and is spatially unresolved except in the radio band, where there is sometimes evidence of collimated outflows or jets of charged particles travelling at relativistic speeds, as shown for example in Figure 1.5. The emission shows fluctuations on timescales from years to minutes; from causality arguments the short time scale variation implies a very compact emission region. The emission is mainly dominated by non-thermal processes. To date, only three classes of extragalactic objects, blazars, radio galaxies and starburst galaxies have been detected at VHE gamma-ray level. Blazars, which include BL Lacertae objects and FSRQs, are a class of AGN whose collimated jets are orientated within a few degrees of our line of sight. Non-blazar sources detected in TeV gamma rays include the FR1 galaxy M 87 (Aharonian et al., 2003, 2006b), and the starburst M 82 (Acciari et al., 2009a; Abdo et al., 2010). The main elements of AGN are discussed in more detail in Chapter 4.

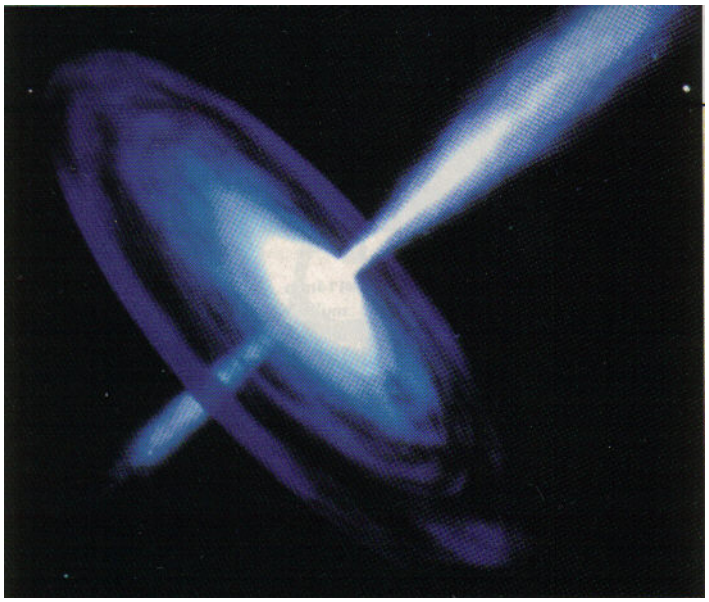

Figure 1.5: Artist's impression of an active galactic nucleus (Berry, 1995).

1.3.6 Gamma-Ray Bursts

Gamma-ray bursts (GRBs) are intense flashes of gamma rays which generally appear to last for milliseconds up to seconds and come at random times and from random directions in the sky. They are often followed by "afterglow" emission at longer wavelengths (X-ray, UV, optical, IR and radio). Gamma-ray bursts are described as either long or short depending on whether their duration is longer or shorter than 2 seconds, but whether they are long or short, gamma-ray bursts can briefly be the brightest gamma-ray objects in the sky. Quantifying their duration is difficult as it depends upon the slew time of the telescope, and the sensitivity and timing resolution of the detecting system. GRB models of long duration gamma-ray bursts suggest that the intense, but brief, emission of energy may be caused by the core-collapse of a rapidly rotating high-mass star into a singularity, resulting in collimated emission. Short-duration gamma-ray bursts, which make up less than half of all gamma-ray bursts, differ from long gamma-ray bursts, not just in duration but also in their energy distribution. Short-duration gamma-ray bursts appear to be due to other processes, possibly the collision of two neutron stars orbiting in a binary system. To date, TeV emission has not been detected in association with any GRB.

1.4 Thesis Overview

The main goal of this work is to search for emission of TeV gamma rays from the starburst galaxy IC 342. From October 2003 to April 2004, IC 342 was observed with the Whipple 10-metre telescope, which is located on Mount Hopkins, southern Arizona. The data recorded were subjected to a range of analyses.

Chapter 2 discusses the range of instrumentation and techniques used to detect VHE gamma rays. Chapter 3 describes the design and operation of the Whipple 10-metre telescope. Chapter 4 deals with the basic features of AGN and starburst galaxies. Chapter 5 describes the range of analysis methodologies used. Chapter 6 discusses the results of applying these analysis methodologies to the recorded data.

Chapter 2

Detection of Very High Energy Gamma Radiation

2.1 Introduction

Gamma rays with energies above $\sim$ 1 TeV cannot be detected directly. On the one hand, they are absorbed high in the Earth's atmosphere. On the other hand, the collection areas and detector thicknesses possible with satellites are too small (because of payload limitations) for the very low flux and high penetrating power of the radiation. Moreover, it is not possible to focus gamma-ray photons. At somewhat lower energies in the GeV range, detectors making use of electron-positron pair production can be carried on satellites while at even lower energies in the MeV range, scintillation detectors (e.g., sodium iodide) can be used.

2.2 Satellite-Based Gamma-Ray Detection

For photon energy above a few MeV, the interaction length in matter is of the order 30 g cm^{-2}. Since the Earth's atmosphere is about 1030 g cm^{-2} thick, the only method of directly detecting high-energy gamma radiation is with space-based instruments. However, satellite detectors have small effective collection areas due to size and weight restrictions imposed on them for launching from Earth, and this limits the highest energies which can be detected by satellites.

The first gamma-ray detector placed into orbit was carried on board the Explorer-XI satellite in 1961. In total, it detected less than 100 gamma-ray pho-

tons, and these appeared to come from random directions. Such a background detection was expected for cosmic rays which originate from random directions in the interstellar medium. In 1972 NASA launched the Small Astronomy Satellite (SAS-2) (Fichtel et al., 1975), followed later in 1975 by the European COS-B satellite (Swanenburg et al., 1981), and it was with the advent of these satellites that point sources of gamma-ray photons were first detected. Among the results achieved by these satellites was the detection of pulsed gamma-ray emission from Vela and from the Crab Nebula.

The success of these missions provided the impetus for larger and more sensitive instruments to improve detection in this field.

2.2.1 The Compton Gamma-Ray Observatory

The Compton Gamma-Ray Observatory (CGRO) was launched by space shuttle in April 1991. The instruments on board the CGRO were of much higher technical specification than its predecessors, including a much larger effective collection area, and greater angular and energy resolution. The satellite itself carried four different detectors which when combined provided energy range coverage from 30 keV to 30 GeV. The instruments on board the CGRO were:

- COMPTEL: The Compton Telescope operated in the energy range 0.75 MeV to 30 MeV (Zhang et al., 2002). COMPTEL was important to nuclear astrophysics where reactions occur in events such as novae and supernovae.

- BATSE: The Burst And Transient Source Experiment operated in the 20 keV to 1 MeV energy range. BATSE employed eight independent sodium iodide scintillator detectors, one at each corner of the satellite, to provide a continuous view of all parts of the sky not obscured by the Earth. While an individual BATSE module could not record the direction the direction of the incident gamma ray, the relative strength of the burst signal in each module resulted in an approximate triangulation of the burst position.

- OSSE: The Orientated Scintillator Spectrometer Experiment operated in the 100 keV to 10 MeV energy range and comprised four independent collimated scintillators which allowed the detector to focus on a single source. The independent modules could also view a background region simultaneously for comparison with the source region, allowing OSSE to detect sources much weaker than those routinely observed by BATSE.

- EGRET: The Energetic Gamma-Ray Experiment Telescope operated in the 30 MeV to 30 GeV energy range (Tavani et al., 1999). The EGRET experiment was of the most interest to the VHE gamma-ray community since it operated at the high end of the energy spectrum of all the experiments based on board the CGRO. The EGRET instrument was a pair-production telescope, similar in design to SAS-2 and COS-B but with a much larger effective collection area and greater sensitivity.

  EGRET consisted of a spark chamber, divided into two parts. Electron-positron pairs generated by incident gamma rays passing through the upper section of the spark chamber were traced through the remainder of the upper and lower chambers into a sodium iodide crystal where their energy was deposited and detected. An anti-coincidence shield eliminated triggering of events caused by cosmic rays. The CGRO, of which EGRET was an element, de-orbited in June 2000 (Harris, 2002). A diagram of EGRET is shown in Figure 2.1. Figure 2.2 and Figure 2.3 show sky maps of gamma-ray sources and gamma-ray bursts detected by EGRET and BATSE, respectively.

2.2.2 INTEGRAL

The INTErnational Gamma-Ray Astrophysics Laboratory was launched in October 2002 (Beckmann et al., 2005) and consists of four instruments: a gamma-ray spectrometer (20 keV − 8 MeV), an imager (15 keV − 10 MeV), an X-ray monitor (3 eV − 35 keV) and an optical monitor, allowing simultaneous observations of a source in the visible, X-ray and gamma-ray bands.

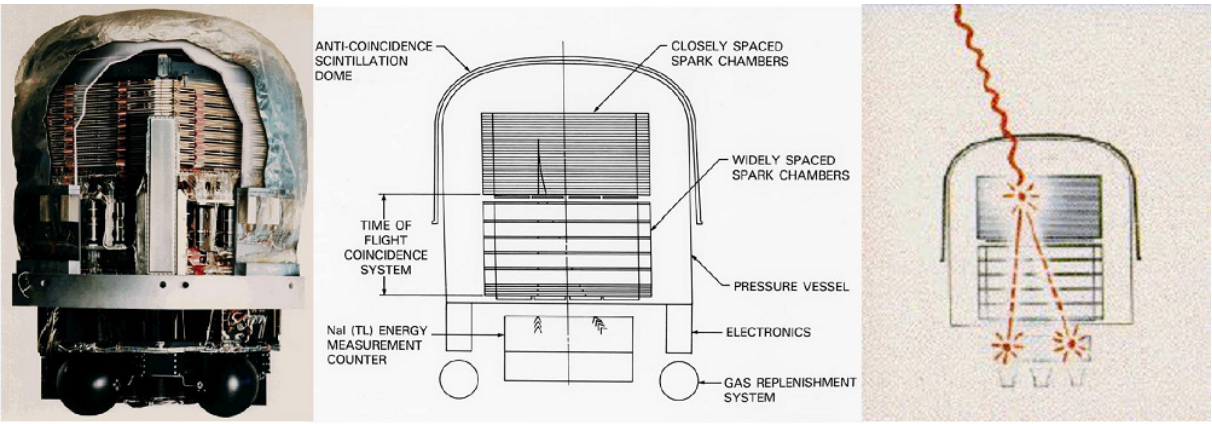

Figure 2.1: Schematic and operational diagram of EGRET. Images taken from http://imagine.gsfc.nasa.gov/docs/features/bios/thompson/egret.html and http://heasarc.gsfc.nasa.gov/docs/cgro/egret/egret_doc.html#sec1.

2.2.3 Swift

The Swift gamma-ray burst explorer is a joint European (U.K., Italy and France) and U.S. satellite which was launched in November 2004 (Burrows et al., 2005). On board Swift is the Burst Alert Telescope (BAT) which can detect and locate gamma-ray bursts (GRBs) to arcminute precision. The satellite can then swiftly reposition itself so that the other two instruments on board, the X-Ray Telescope (XRT) and the Ultra Violet Optical Telescope (UVOT), will detect the afterglow of GRBs and locate them to sub arcsecond positions.

2.2.4 AGILE

The Astro-rivelatore Gamma a Immagini L'Eggero (Light Imaging Detector for Gamma-ray Astronomy) is an Italian mission launched in April 2007 (AGILE Webpage, 2007; Longo, 2007). AGILE was the first gamma-ray telescope to use solid-state detection instead of the spark chamber detection method. This results in excellent angular resolution but confined to a limited energy resolution. AGILE can detect gamma-ray photons in the 30 MeV $-$ 50 GeV energy range (Mereghetti et al., 1999; Pellizzoni et al., 2003).

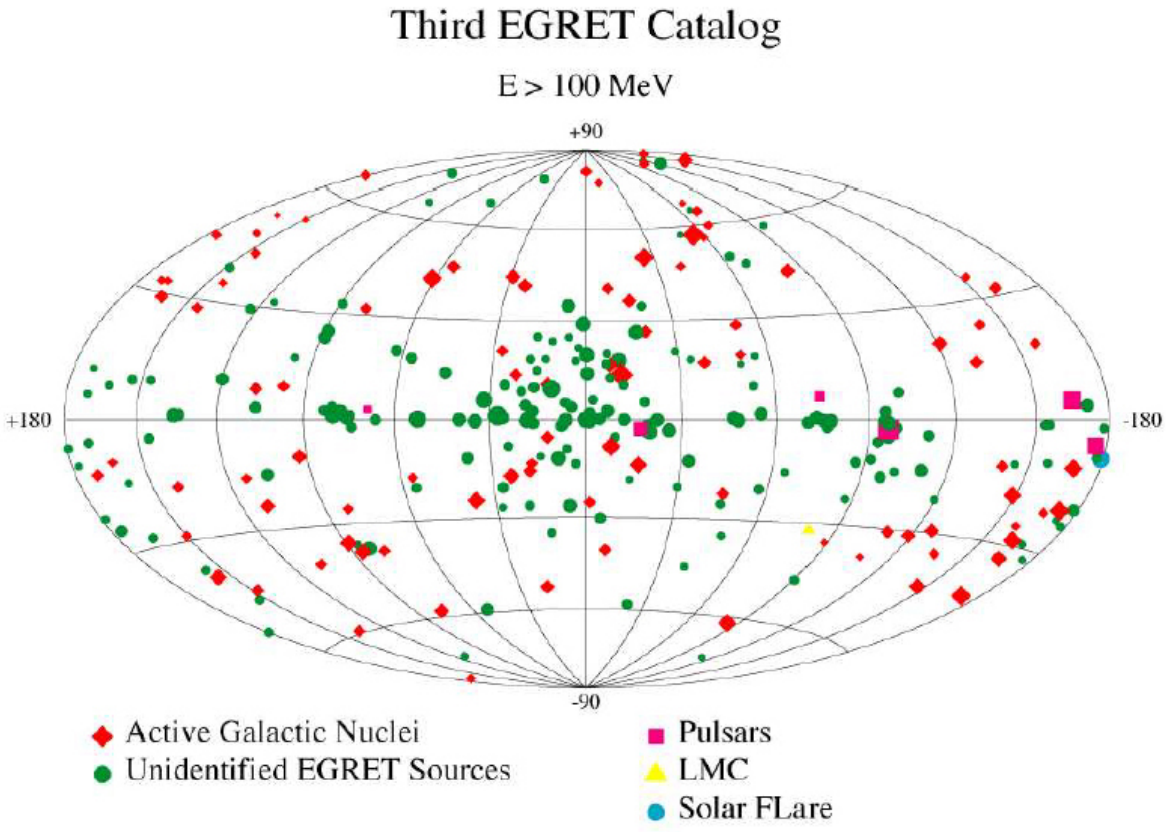

Figure 2.2: The third EGRET catalogue of high-energy gamma-ray sources (Hartman et al., 1999).

2.2.5 Fermi

The Fermi Gamma-ray Space Telescope (formally known as the Gamma-ray Large Area Space Telescope, GLAST) launched in June 2008 (Fermi Webpage, 2008) is a next-generation satellite gamma-ray detector. The Fermi satellite carries two telescopes: the Large Area Telescope (LAT) and the Gamma-ray Burst Monitor (GBM). The LAT detects gamma-ray sources in the 20 MeV to 300 GeV energy range (Chen et al., 2004), employing silicon detector strips to give precise tracking of electron-positron cascades. Each silicon strip is surrounded by a plastic anti-coincidence shield to prevent triggering by events not associated with gamma rays. The energy measurement is provided by a segmented caesium iodide scintillation calorimeter, located between the silicon strips. The GBM employs 12 sodium iodide scintillation detectors and 2 bis-

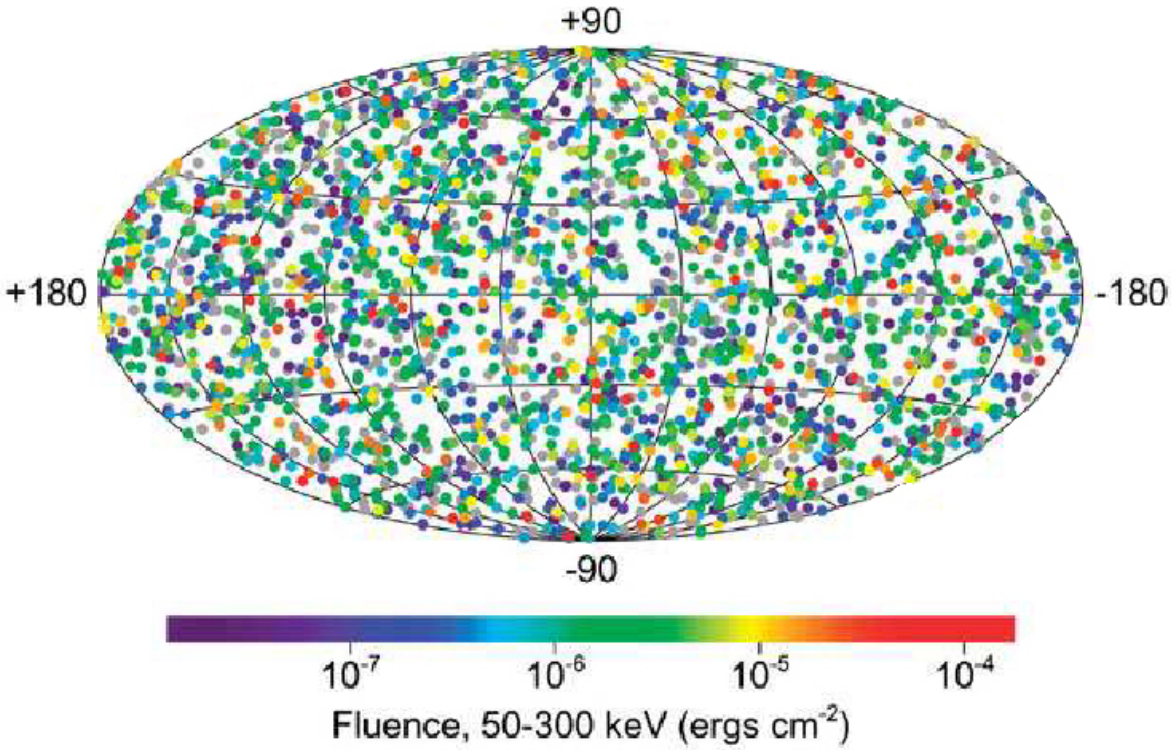

Figure 2.3: Map of the sky showing the distribution of gamma-ray bursts, based on observations by BATSE, on-board the CGRO. Image taken from http://cossc.gsfc.nasa.gov/docs/cgro/batse/.

muth germanate scintillation detectors, and continues the work of BATSE by providing positional and spectral information for gamma-ray bursts.

As Fermi does not use any consumables such as spark chamber gas, it is expected to have a larger duty cycle than EGRET (on board the CGRO). Although it is only twice as heavy as EGRET, Fermi outperforms its predecessor by a factor of ~ 30. An exciting feature of Fermi is the overlap in detectable energy range with newer ground-based telescopes.

2.3 Ground-Based Gamma-Ray Detection

Gamma rays in the VHE energy range and above are so energetic that it is very difficult to produce them even in the most extreme astrophysical environments, and the flux falls rapidly with increasing energy. As a result satellite-based

Satellite Name	Operating Period	Energy Range
SAS-2	1972 − 1973	20 MeV − 1 GeV
COS-B	1975 − 1982	2 keV − 5 GeV
CGRO	1991 − 2000	30 keV − 30 GeV
INTEGRAL	2002 − Present	15 keV − 10 MeV
Swift	2004 − Present	0.2 keV − 150 keV
AGILE	2007 − Present	30 MeV − 50 GeV
Fermi	2008 − Present	20 MeV − 300 GeV

Table 2.1: A summary of some space-based gamma-ray detectors.

detectors have very limited gamma-ray photon detection at the highest energies. As mentioned earlier in this chapter, satellite-based detectors have small effective collection areas due to size and weight restrictions imposed on them for launching from Earth. Ground-based detectors can overcome the problem of having a small effective collection area but must rely on detecting the radiation indirectly because incident gamma-ray photons collide and interact with the Earth's atmosphere. Such collisions of high-energy photons produce secondary charged particle cascades in the upper atmosphere where the energy of the incident gamma-ray photon is transferred to the cascade of the secondary charged particles which propagate towards the ground. This burst of secondary charged particles is termed an extensive air shower (EAS) and it is by detection of radiation from these shower particles that gamma-ray photons can be detected indirectly at ground level.

Only a tiny proportion of extensive air showers in the Earth's atmosphere are generated by gamma-ray photons. The vast majority of EASs are generated by cosmic-ray protons and heavier nuclei which arrive at Earth from random directions. However, gamma-ray-initiated showers and cosmic-ray-initiated showers have different characteristics, which proves significant for discrimination purposes.

2.3.1 Gamma-Ray-Induced Showers

A gamma-ray-induced extensive air shower is initiated when a high-energy gamma ray interacts with the Earth's atmosphere to produce a relativistic electron-positron pair (see Figure 2.4). This electron-positron pair will then radiate gamma rays via Bremsstrahlung in the electric field of atmospheric nuclei. In turn, these gamma rays can produce more electron-positron pairs which can undergo further Bremsstrahlung and so on, creating a particle avalanche or cascade. The resulting cascade of photons, electrons and positrons travels in the direction of the original incident gamma ray. A small amount of lateral broadening of the shower occurs due to Coulomb scattering of shower electrons off loosely-bound atomic electrons, forming a disc some metres thick perpendicular to the trajectory of the initial incident gamma ray.

The cascade initially develops exponentially and, depending on the energy of the incident gamma ray, can contain thousands of particles. The growth of the shower is halted when the photon energy drops below $\sim$ 86 MeV, when ionisation losses begin to dominate over radiative losses. The resulting shower energy then dissipates via ionisation of atmospheric atoms. Most of the charged particles are generated at a height of 6 km $-$ 10 km above sea level in the atmosphere.

A very small muonic component can occur in the shower due to photon-photon collisions or photonuclear production of pions which can then decay into muons. These mechanisms are listed in Equations 2.1, 2.2 and 2.3.

$$\gamma + \gamma \rightarrow \mu^+ + \mu^- \tag{2.1}$$

$$\gamma + p \rightarrow n + \pi^+ \tag{2.2}$$

$$\gamma + n \rightarrow p + \pi^- \tag{2.3}$$

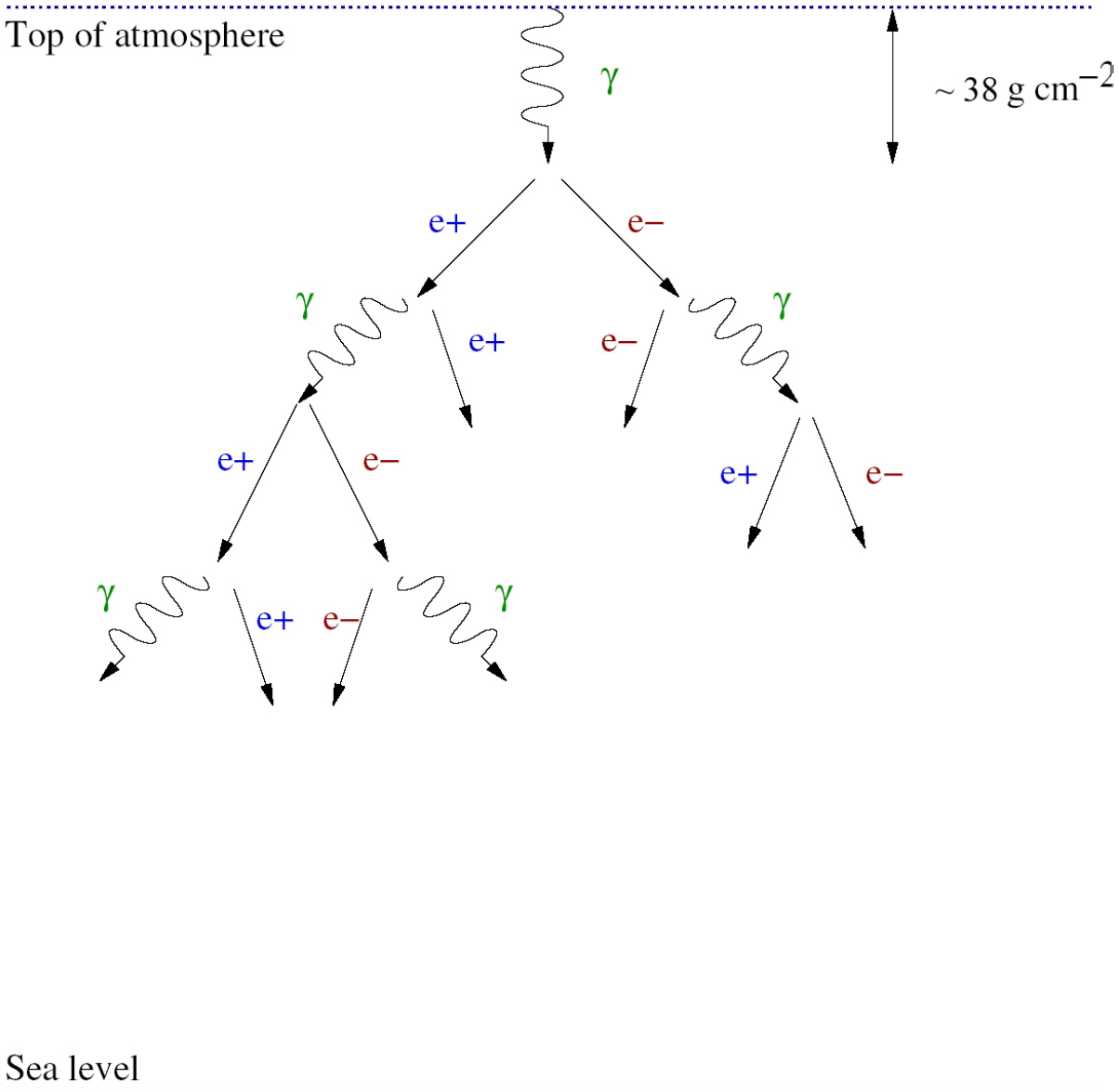

Figure 2.4: Structure of an extensive air shower (EAS) produced by the interaction of a very high energy gamma-ray photon with the Earth's atmosphere (adapted from Gammell (2004)). Note that this diagram is not to scale.

2.3.2 Cosmic-Ray-Induced Showers

The vast majority of extensive air showers are initiated by cosmic rays (hadrons), most of which are protons. When such a high-energy charged particle collides with an atmospheric nucleus (e.g., nitrogen or oxygen), part of the energy is converted into matter. The fragments of the incident nucleus and the new secondary particles formed travel through the atmosphere at high velocity until another nuclear reaction takes place in which more particles are created and so on. The number of charged particles in this cascade increases until the shower reaches its maximum development, the point at which the particles begin to be absorbed by the atmosphere (see Figure 2.5).

The interactions in the nuclear cascade can lead to the production of π mesons. The uncharged π^0 decay into two gamma-ray photons, which in turn can initiate electromagnetic cascades as discussed in Section 2.3.1. Charged pions decay into muons and (anti)neutrinos, so in contrast to gamma-ray-induced showers, hadronic showers have a large muonic component.

$$p + p \rightarrow \pi^0 \ / \ \pi^+ \ / \ \pi^- + \text{ other fragments} \tag{2.4}$$

$$\pi^0 \rightarrow \gamma + \gamma \tag{2.5}$$

$$\pi^+ \rightarrow \mu^+ + \nu_\mu \tag{2.6}$$

$$\pi^- \rightarrow \mu^- + \bar{\nu}_\mu \tag{2.7}$$

Some of the muons can subsequently decay into electrons and neutrinos via the following reaction:

$$\mu^+ \rightarrow e^+ + \bar{\nu}_\mu + \nu_e \tag{2.8}$$

$$\mu^- \rightarrow e^+ + \nu_\mu + \bar{\nu}_e \tag{2.9}$$

As hadron-initiated showers have three separate components, there is a much larger variation from shower to shower compared to a purely electromagnetic

shower. The pions created in the collisions between the cosmic rays and the atmospheric nuclei can be emitted at wide angles to the incident cosmic-ray direction. This results in a shower which has a much larger transverse momentum component and greater asymmetry than the purely electromagnetic showers.

The interaction length for the initiating cosmic ray is ~ 80 g cm^{-2}, which means that on average, nucleonic cascades will develop deeper in the atmosphere than those initiated by gamma rays, which have a much shorter interaction length of ~ 38 g cm^{-2}.

2.3.3 Cherenkov Emission

During their brief existence in the extensive air shower, charged particles possess a large amount of energy derived from the initial gamma-ray or cosmic-ray particle and may travel at velocities faster than the local speed of light. When a charged particle travels at velocity v through a dielectric medium, at a speed higher than the local speed of light for that medium, electromagnetic radiation is emitted. This is known as Cherenkov radiation, after the Russian scientist who first discovered the phenomenon in 1934. This radiation is emitted not by the charged particle, but by the local medium which the particle traverses.

As a charged particle travels through a medium, it induces transient electric dipoles in the local medium. If the charged particle travels at a velocity $v > \frac{c}{n}$ (where n is the local refractive index), no dipoles are created in the region *ahead* of the travelling charged particle: the charged particle is essentially travelling faster than its own electric field. As the charged particle passes through the medium ($v > \frac{c}{n}$), it polarises molecules in the surrounding medium; these molecules then emit a pulse of radiation in the UV/visible region of the electromagnetic spectrum as they relax to the unpolarised state. As the charged particle travels, these pulses interfere constructively to produce a coherent wavefront at an angle θ with respect to the direction of the motion of the charged particle. In a way, this is the optical equivalent of a sonic boom. This is illustrated in Figure 2.6. The angle θ is given by:

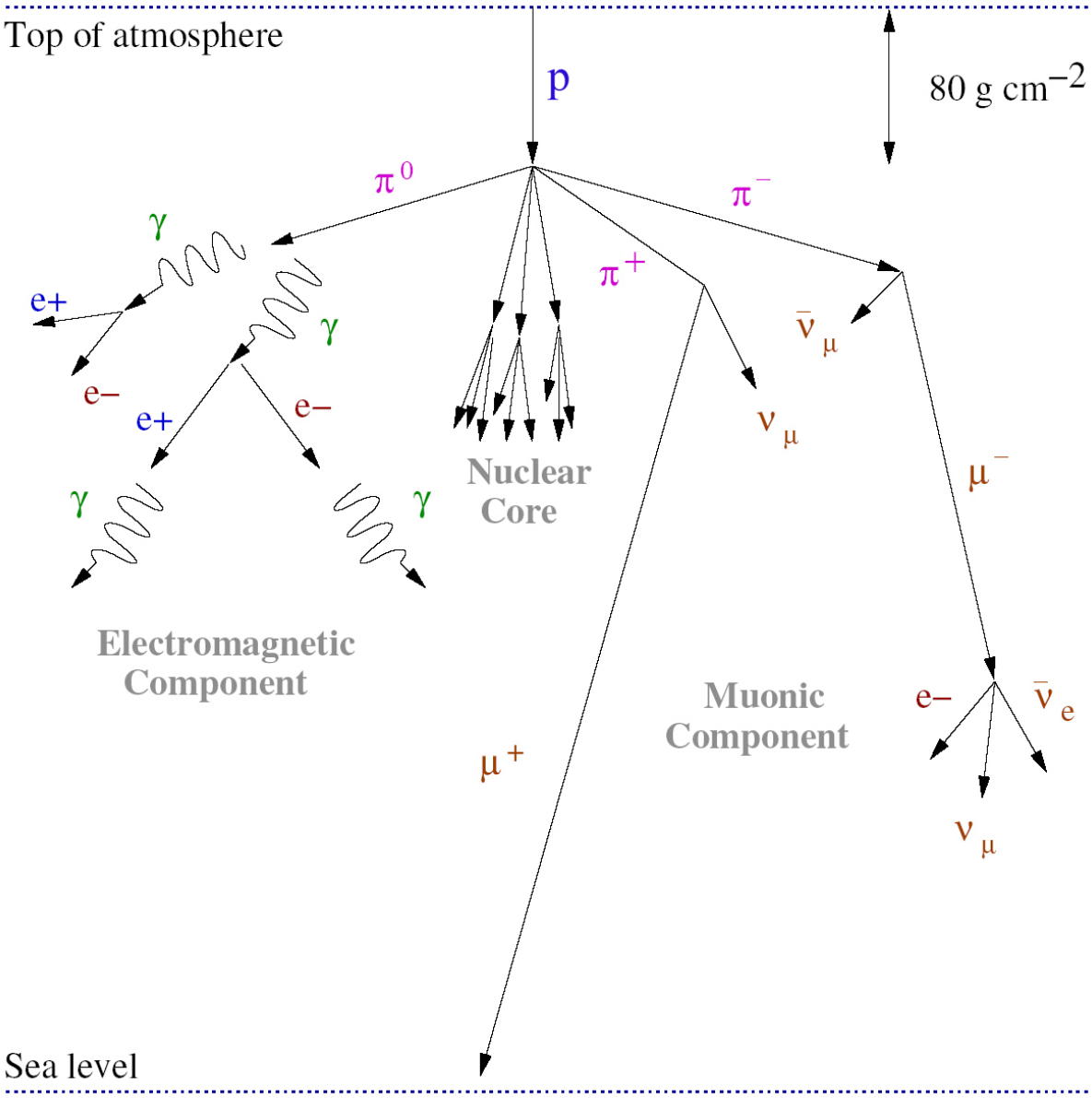

Figure 2.5: Structure of an extensive air shower (EAS) produced by the interaction of a very high energy cosmic-ray particle with the Earth's atmosphere (from Gammell (2004)). Note that this diagram is not to scale.

$$\cos\theta = \frac{\frac{c}{n}t}{vt} = \frac{1}{\beta n} \tag{2.10}$$

where t is time, v is the velocity of the charged particle and β ($\approx v/c$) is the ratio of the particle velocity to the velocity of light in a vacuum.

The Cherenkov light distribution produced from a gamma-ray-initiated EAS differs from that of a cosmic-ray-initiated EAS. Cherenkov light retains the original direction of the incident photon. When a Cherenkov telescope is tracking a VHE gamma-ray source, the Cherenkov image of an EAS produced by a gamma ray from that source will point toward the centre of the camera since the axis of the EAS will be orientated parallel to the optic axis of the telescope. Cosmic-ray showers, however, arrive randomly distributed and the resulting EAS images point in all directions in the camera. Moreover, gamma-ray showers produce narrow, compact, elliptical Cherenkov images, whereas cosmic-ray-initiated showers produce images which are much broader and asymmetrical. Figure 2.7 shows Monte Carlo simulations of EASs induced by gamma rays and cosmic rays.

The differences in shape between the Cherenkov images from EASs can be used to discriminate between gamma-ray-initiated events and cosmic-ray-initiated events. Taking into account the characteristics such as shape, length, size and orientation expected for a gamma-ray-like Cherenkov image enables us to reject most of the unwanted background noise (i.e., cosmic rays) while retaining a large proportion of the gamma-ray component. This imaging technique results in much improved ability to detect gamma rays and screen out cosmic rays.

2.3.4 Imaging Atmospheric Cherenkov Telescopes

An imaging atmospheric Cherenkov telescope (IACT) can directly record the Cherenkov light images of EASs, allowing us to discriminate between gamma-ray and cosmic-ray events. The Cherenkov light from an EAS spreads over an

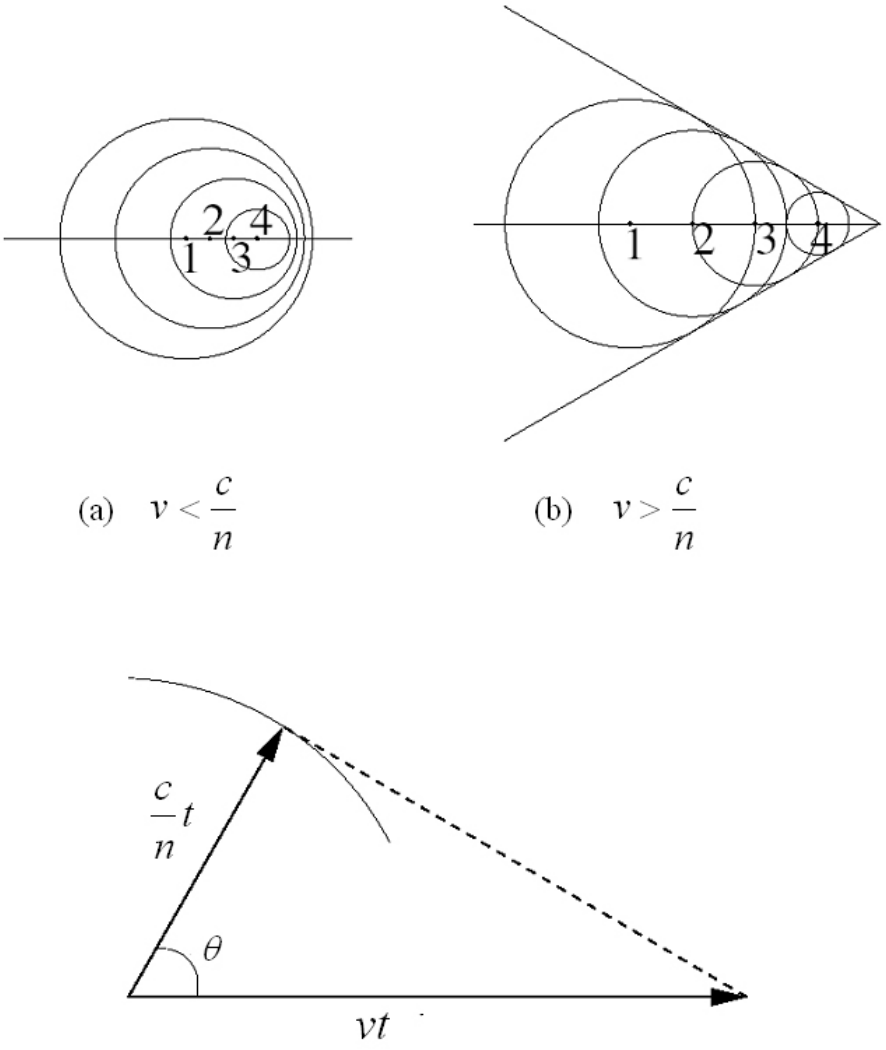

Figure 2.6: Propagation of pulses from moving charged particles in a dielectric medium in the cases where the charged particle is moving (a) slower and (b) faster then the speed of light in the medium. Constructive interference between the potentials occurs along the emission wavefront depicted in (c).

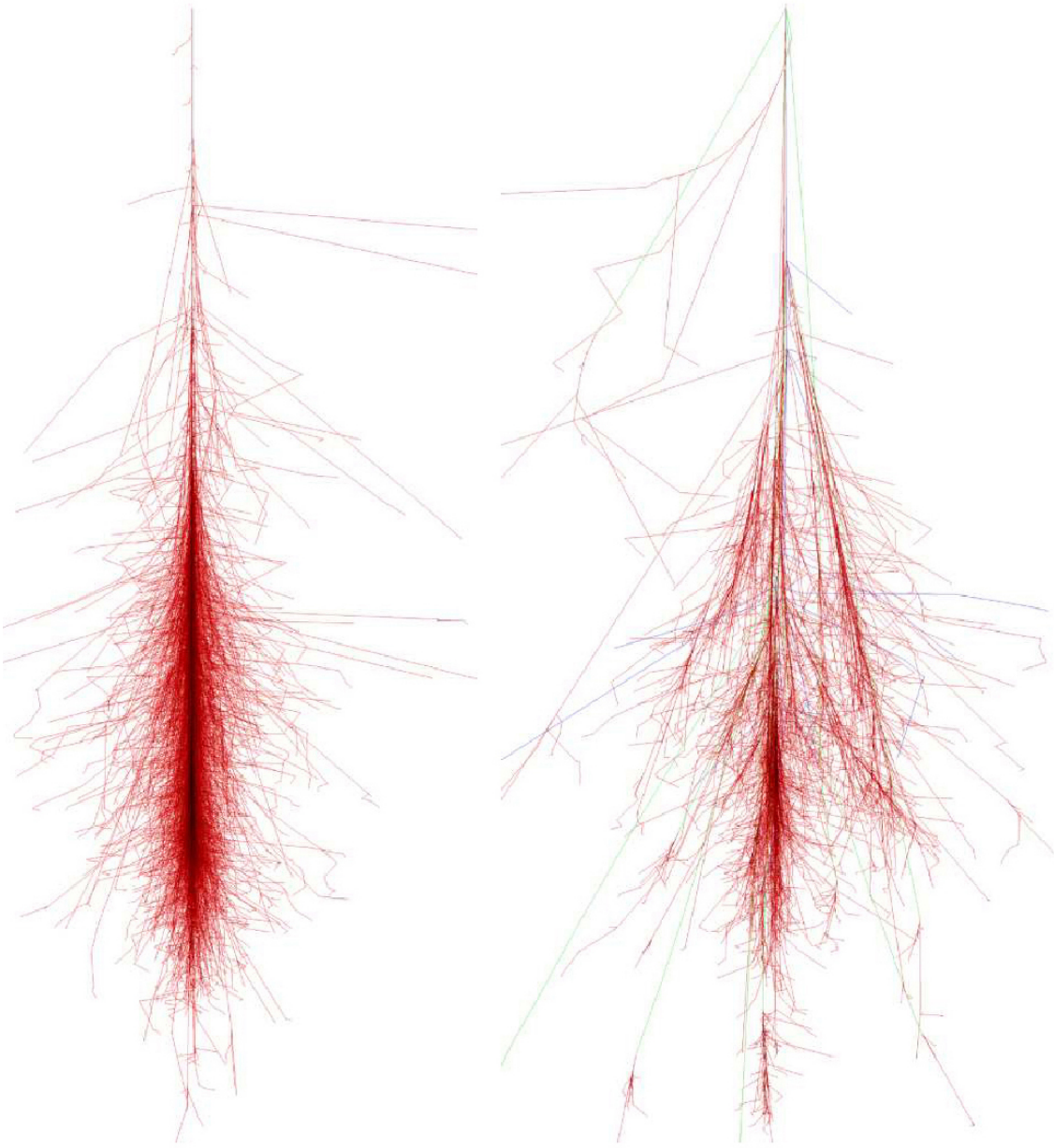

(a) 0.1 TeV photon shower

(b) 0.1 TeV proton shower

Figure 2.7: Monte Carlo simulations of extensive air showers can be used to map the development of an EAS cascade. Shown here are the longitudinal developments of a cascade initiated by (a) a single 0.1 TeV photon and (b) a single 0.1 TeV proton. Red tracks are used to indicate gamma rays, electrons and positrons. Remaining tracks consist of the muonic component of the shower (from Cogan (2006)). The longitudinal scale of this cascade is from sea level to $\sim$ 25 km a.s.l. and lateral $\sim$ 1 km radius from the cascade axis.

Properties	Gamma Ray	Cosmic Ray
Interaction length into atmosphere	~ 38 g cm^{-2}	~ 80 g cm^{-2}
EAS initiates	High in the atmosphere	Deeper down in the atmosphere
EAS transverse shape	Narrow	Broad
Cherenkov light	Mostly blue	Blue & larger UV component
Cherenkov image shape	Narrow, elliptical, well-formed	Broad, more amorphous
Cherenkov image orientation	Points towards centre of camera	No preferential direction

Table 2.2: A summary of gamma-ray and cosmic-ray shower properties.

area of $\sim 10^4$ m^2 at ground level, and the effective collection area of an IACT is comparable to this. This is illustrated in Figure 2.8. The detector is basically a light collector which reflects light onto a camera situated in its focal plane and records an image. The reflector surface is comprised of small tesselated polished mirrors. Whilst the mirrors are profiled to achieve the best image quality, it is the camera which is decisive for good Cherenkov image sensitivity. The camera is composed of an array of photomultiplier tubes (PMTs), accompanied by fast signal-processing electronics. The size of each PMT determines the angular resolution of the telescope while the number of PMTs determines the field of view. High sensitivity and good time resolution are very important as the Cherenkov pulses are extremely weak and short (typically lasting less then 5 ns), and very short electronic gate intervals help to eliminate the effect of night-sky brightness fluctuations. In this way, IACTs have become the most sensitive technique for observing TeV gamma rays. Figure 2.9 shows the four main types of image seen by an IACT telescope. The Cherenkov light image of an EAS produced by a gamma ray will point towards the centre of the camera since

the axis of the EAS will be orientated parallel to the optic axis of the IACT telescope. This is shown in Figure 2.9 (a). Figure 2.9 (b) shows an IACT image of a cosmic ray. A cosmic-ray image will generally not point towards the centre of the camera since the axis of the EAS is not orientated parallel to the optic axis of the IACT telescope. Figure 2.9 (c) shows an instantly recognisable image of a muon ring and Figure 2.9 (d) shows random fluctuations of background sky noise when the IACT telescope is triggered in the absence of a Cherenkov signal.

2.3.5 Cherenkov Wavefront Detectors

The energy threshold of ground-based telescope detectors is primarily dependent on their mirror area. To lower the threshold by a factor of ten requires an increase in mirror area by two orders of magnitude. Solar power plants, with their large mirror areas, can be utilised as instruments of VHE gamma-ray detection during the night. Each heliostat mirror can move independently to follow a source and can be aligned to reflect the light collected to a secondary mirror located high up on a tower. From this, each heliostat can be focused onto a single PMT. Rather than determining the initiator of the EAS via the shape of the Cherenkov image (as with IACTs), the duration or arrival time and Cherenkov photon density is used to determine the direction and energy of the Cherenkov light. Two such Cherenkov wavefront detectors (CWD) are CELESTE and STACEE.

- CELESTE: The Cherenkov Low Energy Sampling and Timing Experiment was situated on the former Électricité de France solar plant in the French Pyrenees at the Thémis site at an altitude of 1650 m (Holder and The CELESTE Collaboration, 2001). The solar array consisted of forty 54-m^2 heliostats which directed the Cherenkov light, via secondary optics at the top of a 100 m tall tower, towards PMTs instrumented with flash analogue to digital converters (FADCs). CELESTE operated from October 1999 to June 2004 (Brion, 2004) and in its first year detected the Crab Nebula above 50 GeV with a significance of 5.7 σ (de Naurois, 2001)

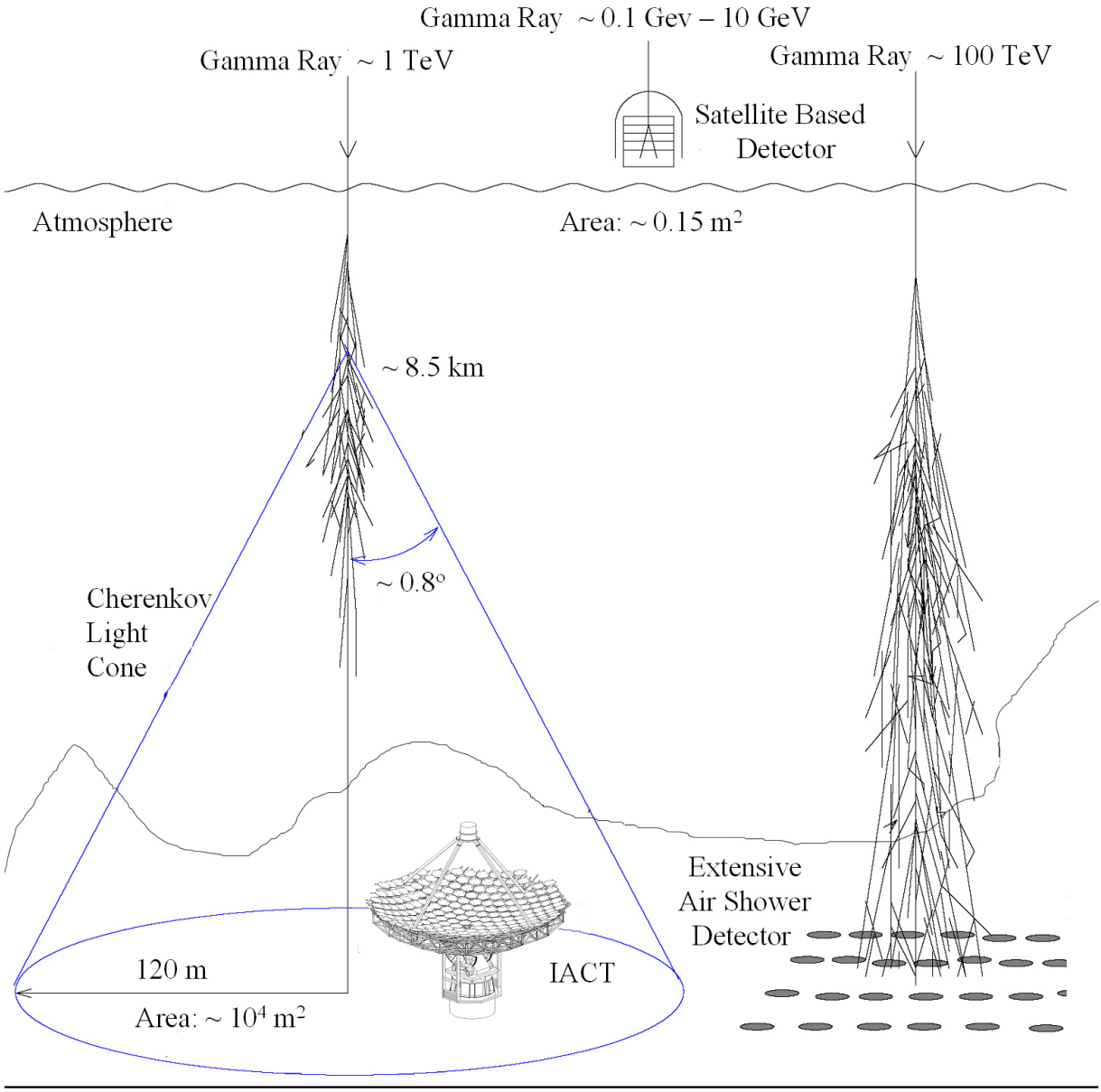

Figure 2.8: Ground-based gamma-ray detectors. Adapted from Quinn (1997).

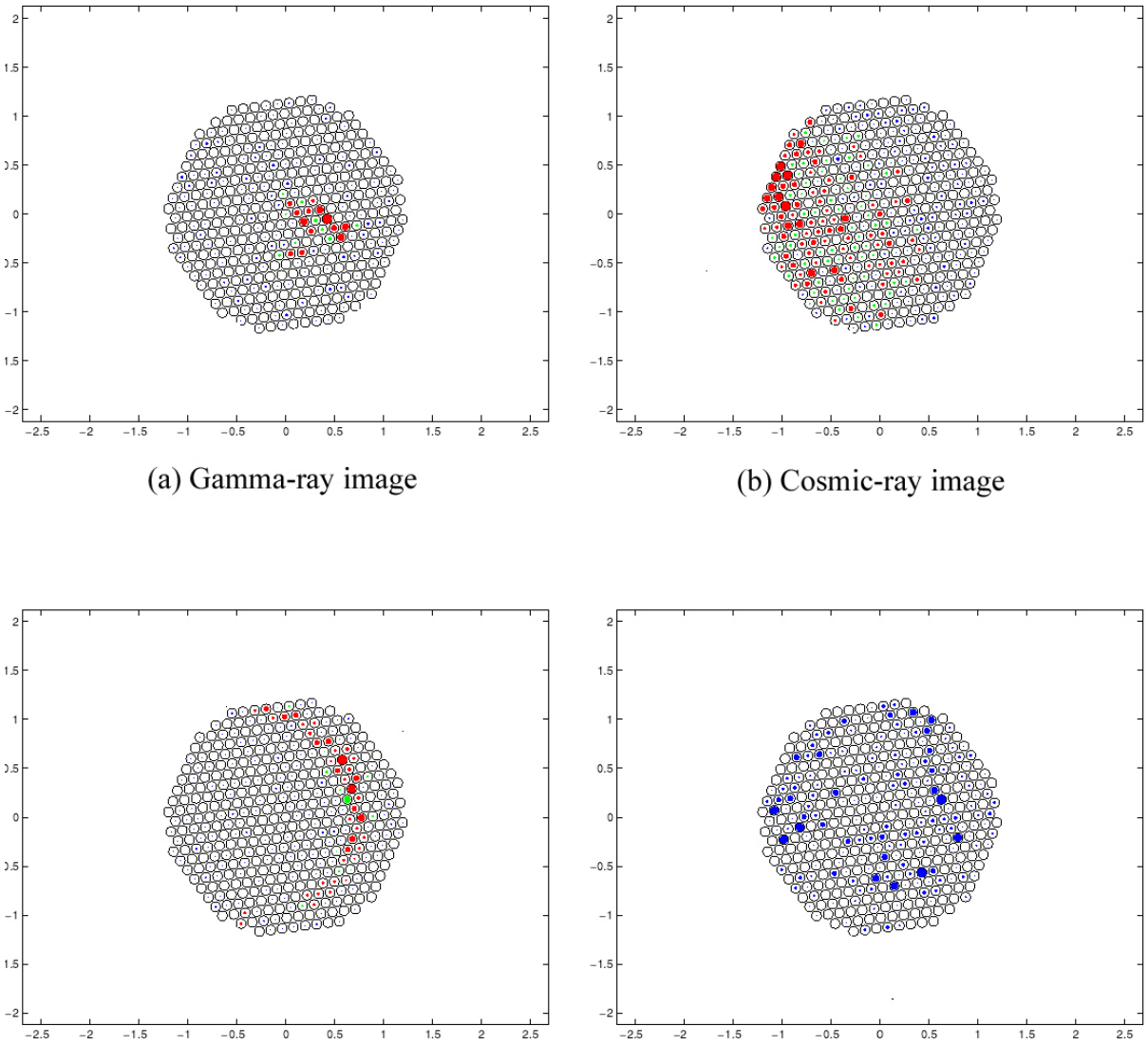

(a) Gamma-ray image

(b) Cosmic-ray image

(c) Local muon image

(d) Sky noise

Figure 2.9: The four main types of event seen by an IACT telescope.

and detected Mrk 501 above 100 GeV with a weak significance of 2.9 σ (Smith et al., 2006).

- STACEE: The Solar Tower Atmospheric Effect Experiment (see Figure 2.10) was located at the National Solar Thermal Test Facility (NSTTF), at Sandia National Laboratories in Albuquerque, New Mexico, USA. STACEE was in a state of development from 1997 and has been fully operational since spring 2002 (Gingrich et al., 2005). Sixty-four of the 220 heliostats, each of area 37 m^2, were used during clear moonless nights to collect Cherenkov light from air showers and direct it onto five secondary mirrors located near the top of a 61 m tower. The total collection area of the sixty-four heliostats was over 2300 m^2. The secondary mirrors focused the Cherenkov light into groups of PMTs such that each PMT viewed a single heliostat. STACEE detected Mrk 421 above 100 GeV with a detection significance of 5.9 σ (Carson et al., 2007) and detected the Crab Nebula above 190 GeV with a detection significance of 6.75 σ (Oser et al., 2001). STACEE was decommissioned in June 2007.

2.3.6 Extensive Air Shower Detectors

At TeV energies, the number of particles that reach ground level is too small for reconstruction of the shower parameters with standard air-shower arrays, made of several detectors spread over a large area. Since extensive air shower detectors (EASDs) trigger on shower size, they can operate at a lower threshold energy if they have the ability to detect these small showers. An instrument capable of sampling a larger fraction of the EAS can be achieved by operating at very high altitude in order to approach the maximum size development of low-energy showers, using a full covering layer of counters to provide high-resolution sampling of the showers and covering the detector array with a layer of lead to increase the number of charged particles by conversion of shower photons (thereby lowering the energy threshold and reducing the time fluctuations of the shower front).

EASDs where water (rather than a lead layer) covers the array of detectors are known as water-Cherenkov EASDs. In such a setup, charged particles entering the detector travel at a velocity greater than the local phase velocity of light in water and emit Cherenkov radiation. A double layer of PMTs, placed around the water pool are employed to detect the Cherenkov light. The upper layer detects the shower front and the bottom layer detects emission from highly penetrating muons. Since cosmic-ray showers are muon-rich and gamma-ray showers are muon-deficient, any shower with high muon content may be rejected as background noise. The arrival times and the density of charged particles at each detector can be used to determine the arrival direction and estimate the energy of the shower initiator, respectively.

EASDs are not restricted to night-time observations and may be operated twenty-four hours a day; they also have a large field of view. However, because extensive air shower detectors only cover a fraction of the ground compared to the shower radius of curvature, they usually have a high energy threshold. Two examples of EASDs, Milagro and ARGO-YBJ, are shown in Figure 2.10.

- Milagro: Milagro was a water-Cherenkov extensive air shower detector (w-C EASD) located at the Fenton Hill site of Los Alamos National Laboratory, about 56 km west of Los Alamos, New Mexico, USA, at an altitude of 2630 m above sea level (750 g cm^{-2}) (Atkins et al., 2004). The reservoir measured 80 m $\times$ 60 m $\times$ 8 m (depth), contained 23 million litres of water (Morales, 2002) and was covered by a light-tight barrier. The PMT layers were arranged on a 2.8 m $\times$ 2.8 m grid. The top layer of PMTs, which lay under 1.4 m of water, contained 450 PMTs whilst the bottom layer of PMTs, which lay under 6 m of water, contained 273 PMTs. Milagro detected the Crab Nebula and Mrk 421 at significance levels of 6.3 σ and 5.8 σ, respectfully. Milagro was decommissioned in June 2008.

- ARGO-YBJ: The Astrophysical Radiation with Ground-based Observatory at Yangbajing is an extensive air shower detector which has been

successfully operated 4300 m above sea level (corresponding to a vertical atmospheric depth of 606 g cm^{-2}) in Tibet, China (30°.11 N, 90°.53 E) since 1990. ARGO-YBJ currently consists of 761 fast-timing scintillation counters covering 50400 m^2 and 28 high-density scintillation counters around the fast-timing counter array. In the inner 36900 m^2, fast-timing counters are deployed at 7.5 m lattice intervals (Amenomori et al., 2005). The detector is composed of a single layer of resistive plate chambers (RPCs) grouped into units called "clusters" (5.7 m × 7.6 m). Each cluster is made up of 12 RPCs (1.225 m × 2.850 m) and each RPC is read out using 10 pads, with dimensions 55.6 cm × 61.8 cm, representing the pixels of the detector. The clusters are arranged in a central full coverage carpet (130 clusters, ∼ 5600 m^2, ∼ 93 % of active surface) surrounded by a sampling guard ring (∼ 40 % of coverage) in order to increase the effective area and improve the core location reconstruction. The detector is connected to two independent data-acquisition systems, corresponding to shower and scaler operation modes (Aielli et al., 2009).

2.4 Present Status and Next-Generation Ground-Based Detectors

Imaging atmospheric Cherenkov telescopes have proven to be the most sensitive and effective of all ground-based gamma-ray detectors in operation to date. Described here are five such systems currently operating: Whipple, VERITAS, H.E.S.S., MAGIC, and CANGAROO. Whipple, VERITAS and MAGIC are located in the northern hemisphere, whilst CANGAROO and H.E.S.S. are located in the southern hemisphere. Although they are situated in different locations around the world, their scientific goals all overlap.

New ground-based gamma-ray detectors coming into operation will be designed with increased sensitivity in the VHE range and much lower energy thresholds and will overlap with new and upcoming satellite-based gamma-ray detectors. This will allow for observations at lower energies for the potential

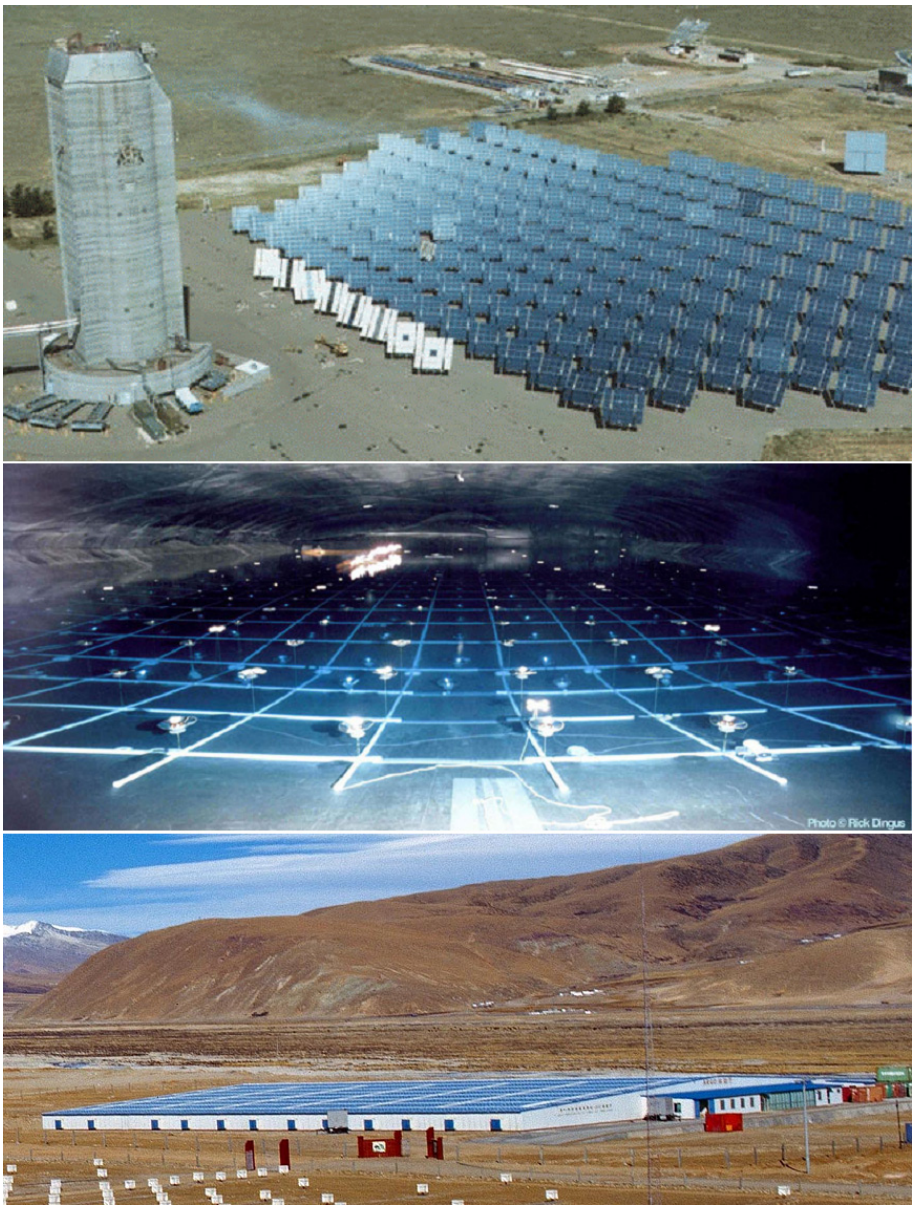

Figure 2.10: Some EAS detectors used for ground-based gamma-ray detection. From the top down they are STACEE (http://www.astro.ucla.edu/∼stacee/index.html), Milagro (http://www.lanl.gov/milagro/index.shtml) and ARGO-YBJ (http://english.ihep.cas.cn/rs/fs/200907/W020090818523546396863.jpg).

detection of new sources and more sensitive and expanded coverage of existing sources.

The design of the IACT instrument itself functions as the main element in the discrimination of background cosmic-ray or hadronic events from the required gamma-ray signal. Two major designs that dominate the IACT field and expanding the VHE gamma-ray astrophysical horizon are large-area detectors and detector arrays.

2.4.1 Large-Area Detectors

More gamma-ray events can be recorded with a larger effective collection area. Ideally, the effective collection area should be comparable to the area of the Cherenkov light pool on the ground. The amount of light recorded from an EAS increases with increasing mirror area, effectively increasing the signal-to-noise ratio, thus it is possible to lower the threshold (lower energy events may be recorded due to a lower triggering threshold).

The Whipple gamma-ray telescope operated by the VERITAS Collaboration at the Fred Lawrence Whipple Observatory was the first such large-area telescope to be constructed, with a mirror aperture of 10 metres. The telescope is operated by on Mount Hopkins in southern Arizona at 2320 m above sea level. This system, which was used for the observation in this work, is described in more detail in Chapter 3.

The Major Atmospheric Gamma Imaging Cherenkov telescopes are representative of a new generation of IACTs for gamma-ray astronomy. The MAGIC telescope design has been optimised to achieve a trigger threshold lower than was possible with previous IACTs: MAGIC-I is designed to reach a trigger threshold of 30 GeV at zenith (Albert et al., 2006b). MAGIC-I, completed in autumn 2003, is located on the Canary Island of La Palma, 2225 m above sea level, and has a parabolic reflector with diameter 17 m and focal length 17 m ($f/D = 1$, total surface area 234 m^2) (Bigongiari, 2005); the camera comprises 576 hemispherical PMTs. The reflector shape is parabolic to minimise the time

spread of Cherenkov light flashes on the focal plane. Aluminium mirrors were chosen instead of glass ones to reduce the weight of the reflecting surface and to allow for fast slewing of the telescope. For the same reason the telescope frame is made of carbon fibre tubes so that MAGIC-I can slew quickly in response to a GRB alert. In 2009, a second telescope, MAGIC-II was installed at a distance of 85 m from MAGIC-I. MAGIC-II was essentially the same characteristics as MAGIC-I except that camera of MAGIC-II uses improved PMTs. Using this stereoscopic arrangement a threshold of 25 GeV has so far been achieved (Aliu and The MAGIC Collaboration, 2008).

2.4.2 Detector Arrays

While lying in the Cherenkov light pool, an array of telescope detectors can record the image of an EAS stereoscopically from different points on the ground. Each detector records a different view of the EAS and on combining these different views, an image of the gamma-ray or cosmic-ray event is produced. The additional information gained by stereoscopic observations of EASs significantly improves event reconstruction, and can improve discrimination between gamma-ray and cosmic-ray events. The detector array also helps to eliminate accidental night-sky-brightness triggers and local muon events. Major detector arrays in operation today include:

- VERITAS: The Very Energetic Radiation Imaging Telescope Array System is a next-generation ground-based gamma-ray observatory designed to operate in the range from 50 GeV to 50 TeV (Cogan and the VERITAS Collaboration, 2004). The VERITAS array consists of four 12m telescopes located at the FLWO basecamp. VERITAS Telescope-1 was operated as a stand-alone IACT instrument from February 2005. The 4-telescope array became fully operational in early 2007.

  The VERITAS telescopes follow a Davies-Cotton optical design with 12 m aperture and 12 m focal length, making it an $f/1$ system. The reflector comprises 350 individual hexagonal mirror facets, each with an area of

0.322 m^2, providing a total mirror area of ~ 110 m^2. The focal plane instrumentation of each telescope is a 499-element PMT camera, with 0.15° angular spacing giving a field of view of 3.5°. The PMT signals are digitised by a custom-designed 500 MHz flash-analogue-to-digital converter (FADC) system. VERITAS employs a three-level trigger system: Level 1 corresponds to the discriminators on each pixel, Level 2 is a pattern trigger for each telescope and Level 3 is the array trigger. Regular observations with the full four-telescope array started in September 2007, with approximately 1000 hr per year of observations taken. In the summer of 2009, two important upgrades were made to VERITAS. Firstly, Telescope-1 was moved to give a better array configuration. Secondly, the facet alignment on individual telescopes was refined to give better image definition.

- CANGAROO: The Collaboration of Australia and Nippon for a GAmma-Ray Observatory in the Outback completed its final development phase CANGAROO-III, in 2004. CANGAROO-III is a stereoscopic system consisting of four IACTs located near Woomera, South Australia at 220 m above sea level. Each telescope has a 10 m diameter reflector consisting of 114 spherical mirror segments, each with diameter 0.80 m and radius of curvature 16.4 m. The segments are aligned on a parabolic frame of focal length 8 m. The total light-collecting area is 57 m^2. The four telescopes are located at the corners of a diamond with spacings of approximately 100 m (Enomoto et al., 2006; Mori and The CANGAROO Collaboration, 2001).

- H.E.S.S.: The High Energy Stereoscopic System is located 1.8 km above sea level in the Khomas Highlands of Namibia, Africa. H.E.S.S. has been operating since June 2002 (Punch and The H.E.S.S. Collaboration, 2005). The detector consists of four 13 m-diameter (Aharonian et al., 2005b) IACTs arranged in a square of side 120 m. Each telescope mount has a tessellated mirror of 107 m^2 area with a camera in the focal plane at 15

Experiment	Location	Detection Type	Operating Period	E_{th} (TeV)
HEGRA	La Palma, Spain	IACT × 5	1996 − 2002	0.5
CELESTE	Thémis, French Pyrenees	CWD	1999 − 2004	0.03
STACEE	New Mexico, USA	CWD	1997 − 2007	0.05
Milagro	New Mexico, USA	w-C EASD	1999 − 2008	0.1
ARGO-YBJ	Yangbajing, Tibet	EASD	1990 − present	0.2
MAGIC	La Palma, Canary Islands	IACT × 2	2003 − present	0.025
Whipple 10m	Arizona, USA	IACT × 1	1967 − present	0.4
VERITAS	Arizona, USA	IACT × 4	2005 − present	0.1
CANGAROO	Woomera, South Australia	IACT × 4	2004 − present	0.1
H.E.S.S.	Namibia, Africa	IACT × 4	2002 − present	0.1

Table 2.3: A summary of some ground-based gamma-ray detectors with their claimed energy thresholds (E_{th}).

m. Each camera contains 960 PMTs with pixel size 0.16°; the overall field of view is 5°. The array is now known as H.E.S.S.-I.

Phase II (H.E.S.S.-II) was initiated in 2008, and involved placement of a very large single telescope at the centre of the H.E.S.S.-I array. The mirror collection area of H.E.S.S.-II is ~ 600 m^2, almost six times as large as that of the H.E.S.S.-I telescopes. The camera has a 3°-wide field of view and comprises $\sim$ 2000 PMTs with pixel size 0.07°, which will provide better image resolution than the original H.E.S.S.-I detector array. Two different modes of operation are foreseen of H.E.S.S.-II. In coincidence mode, the new telescope will be triggered by the H.E.S.S.-I array. In the energy range between 0.1 TeV and a few tens of TeV, this will increase the sensitivity of the array by at least a factor of two compared to H.E.S.S.-I. In stand-alone mode, the energy threshold of the new telescope is expected to be $\sim$ 30 GeV (van Eldik, 2006).

- MAGIC-II: As described in Section 2.4.1, the MAGIC-II array came into operation in 2009.

Figure 2.11: Detector arrays used for ground-based gamma-ray detection. From the top down they are VERITAS (http://veritas.sao.arizona.edu/Images/New_Array.jpg), H.E.S.S. (http://www.mpi-hd.mpg.de/hfm/HESS/public/HESS_IMG/pages/image103.html) and CANGAROO (http://icrhp9.icrr.u-tokyo.ac.jp/image/04Mar/AD080.jpg).

Chapter 3

The Whipple 10-metre Imaging Atmospheric Cherenkov Telescope

3.1 Introduction

The Whipple 10m IACT at the Fred Lawrence Whipple Observatory was constructed in 1968 by the Smithsonian Astrophysical Observatory. It is located on Mount Hopkins in southern Arizona, at an altitude of 2320 metres above sea level. The Arizona climate is ideal for observations using the IACT technique as there are typically eight or nine months of mostly clear, dry nights annually. The primary objective of Whipple 10m telescope is the detection and study of gamma-ray sources. It is currently operated by the VERITAS Collaboration.

The Whipple 10m IACT was the first instrument to detect the Crab Nebula at TeV energies (Weekes et al., 1989). Many other IACTs have since detected the Crab Nebula at TeV energies, and it is now regarded as a standard candle for TeV observations, since its TeV emission appears to be steady.

3.2 The Telescope System

The Whipple 10m IACT system may be subdivided into three primary sections: the reflector, the camera and the electronics.

Figure 3.1: The Whipple 10m telescope, operated by the VERITAS Collaboration on Mount Hopkins in southern Arizona. Image taken from http://veritas.sao.arizona.edu/old/Photos/sunset_slide1.html.

3.2.1 The Reflector

The reflector is based on the Davies-Cotton design (Davies and Cotton, 1957). This type of a reflector consists of a large support structure with radius of curvature 7.3 m on which is mounted a 10 m diameter reflector comprising 248 identical hexagonal tessellated spherical mirror facets. Each mirror facet is coated with an aluminium substrate for high reflectivity in blue/ultraviolet light. The mirror facets are also anodised to protect them from weathering. The overall area of the reflector is 75 m^2 with a focal length of 7.3 m, the distance at which the camera is housed. The radius of curvature of each mirror facet (14.6 m) is twice that of the spherical support structure. This type of design has a number of advantages.

1. The use of a large number of small mirrors means that the reflector is relatively inexpensive to construct, maintain and repair compared with a single 10 m mirror.

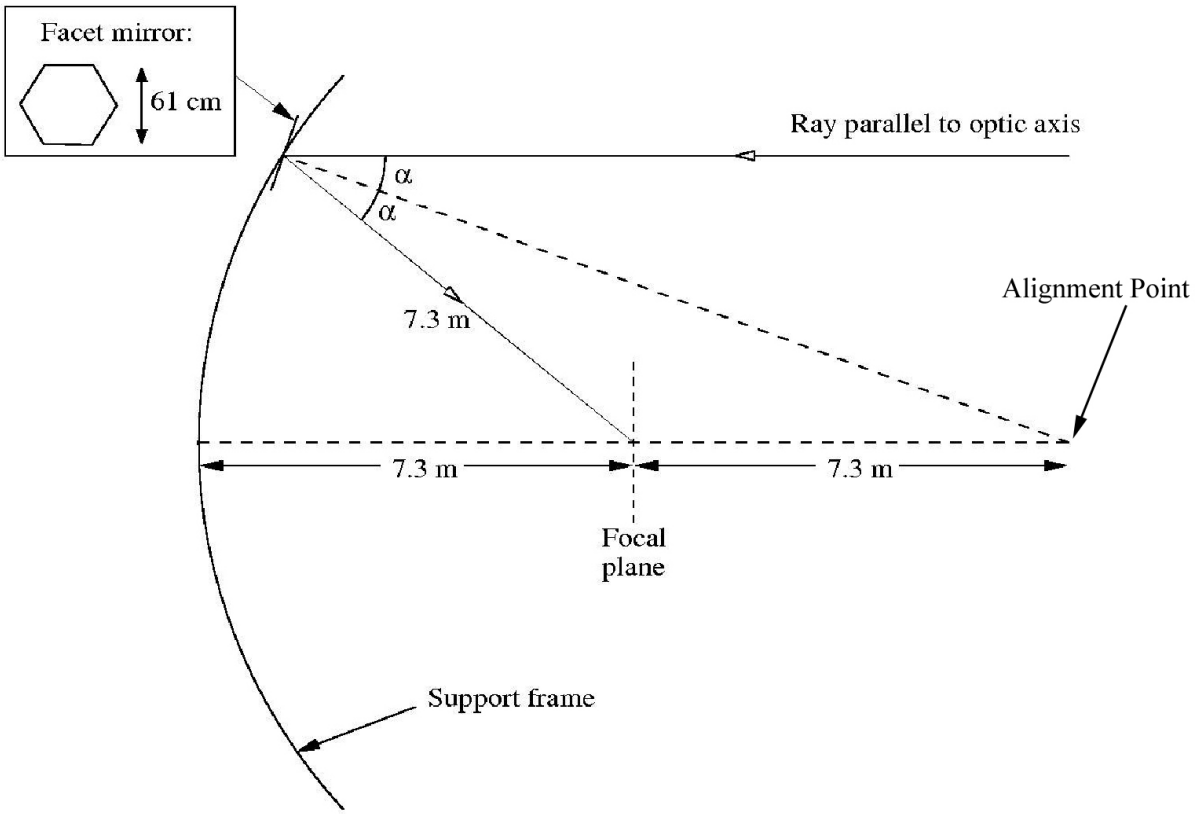

Figure 3.2: Optical configuration of Davies-Cotton design and reflector setup.

2. The alignment of the individual mirror facets is relatively simple. This is achieved by manually adjusting each mirror facet so that their central axes pass through a point at a distance of twice the focal length of the support frame from its centre along the axis frame (see Figure 3.2).

3. The overall structure of the telescope is strong and rigid.

4. Off-axis aberrations are small compared to parabolic reflectors.

The spherical design of the Whipple 10m telescope does have a distinct disadvantage, in that the system is anisochronous, i.e., there is a time difference between light travelling from different parts of the reflector to the camera. In general, light incident parallel to the telescope axis will reach the outer rim of the reflector earlier than light incident close to the axis. The difference in arrival times can be as broad as $\pm$ 6 ns. This is comparable to the duration of

the Cherenkov pulse from an EAS ($\sim$ 5 ns).

3.2.2 The Camera

Ultra high speed detection is required to capture the brief Cherenkov flashes, which typically last for only $\sim$ 10 ns. The Whipple 10m camera and electronics are designed to allow for exposure times comparable with the duration of the Cherenkov flashes.

The camera has undergone many upgrades since the telescope's inception. The camera configuration relevant to the observations carried out for this thesis is the one which was in use from January 2003 onwards. In this configuration, the camera consists of 379 half-inch Hamamatsu H3165 PMTs. [Prior to 2003, the camera included an extra 111 one-inch Hamamatsu R1398 PMTs located around the perimeter of the inner 379 PMTs as depicted in Figure 3.3. These outer PMTs were used primarily to test fibre-optic communications before their removal in January 2003]. The Hamamatsu PMTs have several features which make them ideal for imaging Cherenkov flashes. Firstly, they have response times of the order of nanoseconds, similar to the duration of atmospheric Cherenkov flashes. Secondly, they have high gain ($\sim 10^5 - 10^6$), reducing the need for preamplifiers which would lower the signal-to-noise ratio. Finally, they have high quantum efficiency ($\sim$ 20 %) in the ultraviolet/blue region of the spectrum, which is the region in which the Cherenkov emission peaks.

A downside to this type of PMT array is the amount of dead space between the PMTs due to the metal shielding and plastic coating which surrounds each photocathode. In actuality, the photocathode accounts for only about 35 % of the total area of each PMT, whilst shielding and coating, which serve to prevent deflection of the photoelectrons by the Earth's magnetic field, occupy the remaining area. To overcome this problem, light concentrators ("cones") are placed over the PMTs to recover light falling in the dead space between them and to eliminate extraneous off-axis light.

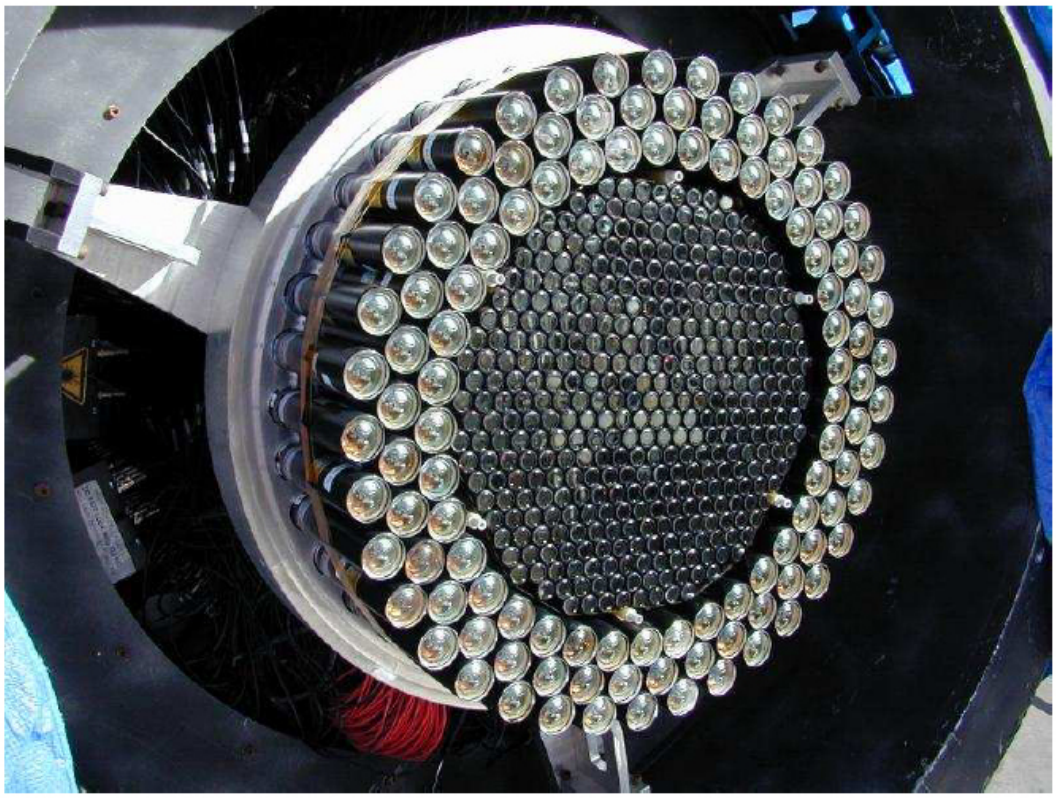

Figure 3.3: The 490-PMT camera used in the Whipple 10m telescope from 1999 to 2003. The outer 111 PMTs were removed in January 2003 to be used as part of the VERITAS prototype telescope. Image taken from http://veritas.sao.arizona.edu/old/Photos/G3Camera2.html

The high-voltage (HV) supply required by the PMTs is provided by three LeCroy HV modules located in the telescope mount counterweights. The PMT anode currents are displayed on a colour-coded graphical user interface (GUI) in the control building adjacent to the telescope. If the currents are too high, the HV to particular PMTs can be switched off to avoid non-linear response or photocathode damage. This may be caused by light from a bright star in the field of view of the camera. It may not be necessary to switch off PMTs for faint stars, although the affected PMTs will have higher noise levels due to the greater fluctuations in the night-sky brightness level. Each PMT has its own analogue-to-digital converter and constant-fraction discriminator, which will be discussed in more detail in Section 3.2.3.

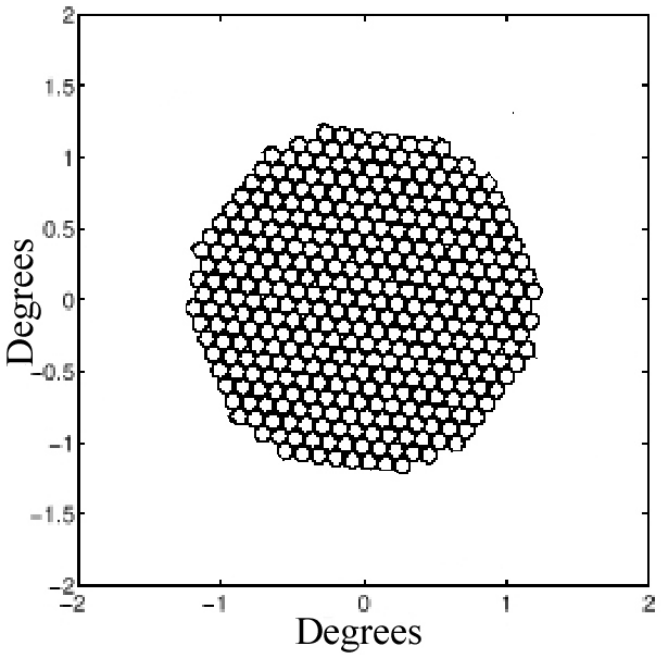

Figure 3.4: Angular map of the PMTs which comprise the Whipple camera.

3.2.3 The Data-Acquisition Electronics

The data-acquisition system for the Whipple 10m telescope is shown in Figure 3.6. The system, which consists of analogue-to-digital converters (ADCs), constant-fraction discriminators and trigger modules, is located in the control building. The signals from the 379 PMTs are transmitted to the control building via coaxial cable. The signal from each PMT is input to an amplifier which has a gain of ten. Each amplifier has three outputs: one output is sent to an ADC, one to the trigger electronics and one to the current monitor.

- Analogue-to-digital Converter: If the light incident on the PMTs contains a Cherenkov signal, each ADC integrates the analogue charge from the entire photoelectron pulse in a PMT and translates this into a digital value quoted in "digital counts" (d.c.), which is stored in a buffer. In travelling from the amplifier to the ADC, the PMT pulse typically broadens from $\sim$ 10 ns to $\sim$ 30 ns. Delay cables which transmit the signals from the amplifiers to the ADCs allow for a delay $\sim$ 120 ns so that the trigger electronics can determine whether or not the signal from the PMTs is a

true Cherenkov signal. If a Cherenkov signal is not present, the ADC inputs are disabled and no information is recorded.

- Constant-fraction Discriminators: The second output from the amplifier is fed into constant-fraction discriminators (CFDs), the first element of the triggering electronics. Only the inner 331 of the 379 PMTs are considered for triggering. When any PMT transmits a signal above a certain threshold, the CFDs output a pulse of preset duration for that PMT. The threshold determines how large the signal must be for a trigger to generated. The value of the threshold, measured in mV, is set by examining the bias curve, which is a plot of trigger rate against threshold height. The threshold used during the observations for this work was set at 34 mV. As the threshold is decreased, the trigger rate will increase as fainter images trigger the system. Below a certain threshold height, the rate of increase of the trigger rate increases almost exponentially. At this point the threshold point is so low that random noise in the PMTs can trigger the electronics. The CFD threshold is set slightly above this level so that the system triggers on as many Cherenkov events as possible without being triggered by random sky-brightness noise. Low-energy Cherenkov events which do not produce enough light to generate an electronic signal above the CFD threshold are not recorded. The CFD pulses are forwarded to two independent triggers, the multiplicity trigger and the pattern selection trigger.

- Multiplicity Trigger: The multiplicity trigger is activated whenever a specified number of simultaneous CFD outputs exceed the preset threshold. For the present work, threefold multiplicity was used, i.e., the multiplicity trigger will activate when any three PMT signals exceed the CFD threshold.

- Pattern Selection Trigger: The pattern selection trigger (PST) is designed to accept signals only if the three triggering PMTs are adjacent. This

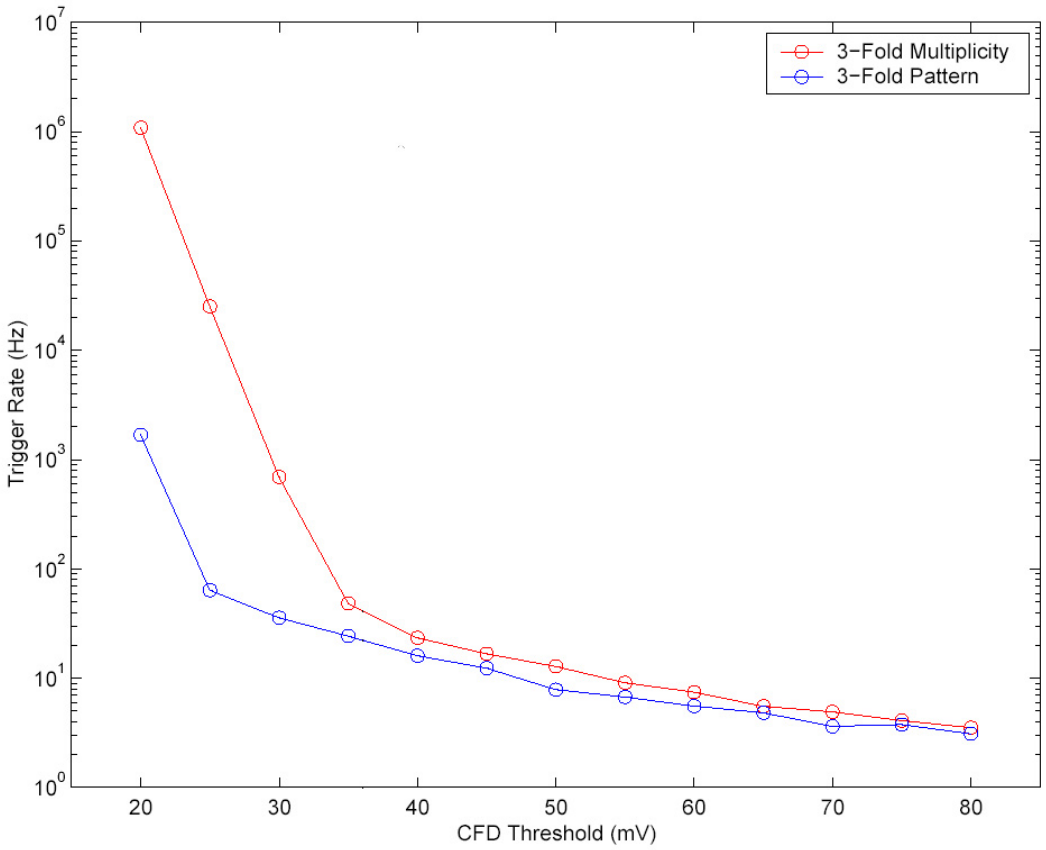

Figure 3.5: Bias curves of trigger rate versus constant-fraction discriminator threshold for multiplicity and pattern selection triggers.

reduces the incidence of triggers resulting from background night-sky noise fluctuations or PMT after-pulsing and allows the CFDs to operate at lower thresholds whilst still maintaining an acceptable overall trigger rate.

If an event passes the multiplicity trigger and PST criteria, a gate pulse from the trigger system enables input of the delayed signals from the amplifiers to the ADCs, and the resulting digital count values are recorded for all PMTs in the camera. Timing for the recorded signals is provided by a global positioning satellite (GPS) receiver and each signal is time-stamped with its coordinated Universal Time (UTC) value.

The digital count values for each event are stored on a data-acquisition (DAQ) computer along with telescope pointing information from the tracking system and the event time from the GPS clock. These data constitute the

Attribute	Value
Opening Diameter	10 m
Focal Length	7.3 m
F-Number	$f/0.73$
No. Of Mirror Facets	248
Curvature radius of dish	7.3 m
Curvature radius of facet-mirror	14.6 m
Energy Threshold	400 GeV
Angular Resolution	0.11°
Pointing Resolution	0.01°
Field Of View	5°
Slew Speed	1°/second
Reflecting Surface Area	75 m^2

Table 3.1: General dimensions and attributes of the Whipple 10m telescope.

raw data for the event and it is these data which are later analysed off-line to determine the gamma-ray content of the recorded events, as will be described in detail in Chapter 5.

3.3 Calibration and Diagnostic Techniques

The camera consists of an array of 379 PMTs each with its own HV supply, electric cabling and electronics. Due to normal variation in each of these components, each PMT will respond slightly differently to the same stimulus. To account for this, the differences in each PMT must be measured so that the camera can be uniformly calibrated. There are a number of ways to calibrate the camera and the system as a whole.

3.3.1 Pedestal Determination

The background night-sky brightness fluctuates above and below some mean value. Since the ADC can only record positive values, a small positive offset is added to the ADC input so that both positive and negative night-sky brightness fluctuations can be recorded. The resulting offset in the ADC output is called the "pedestal". In order to determine the value of the pedestal for each ADC, artificial triggers are generated once per second to record the signals from the

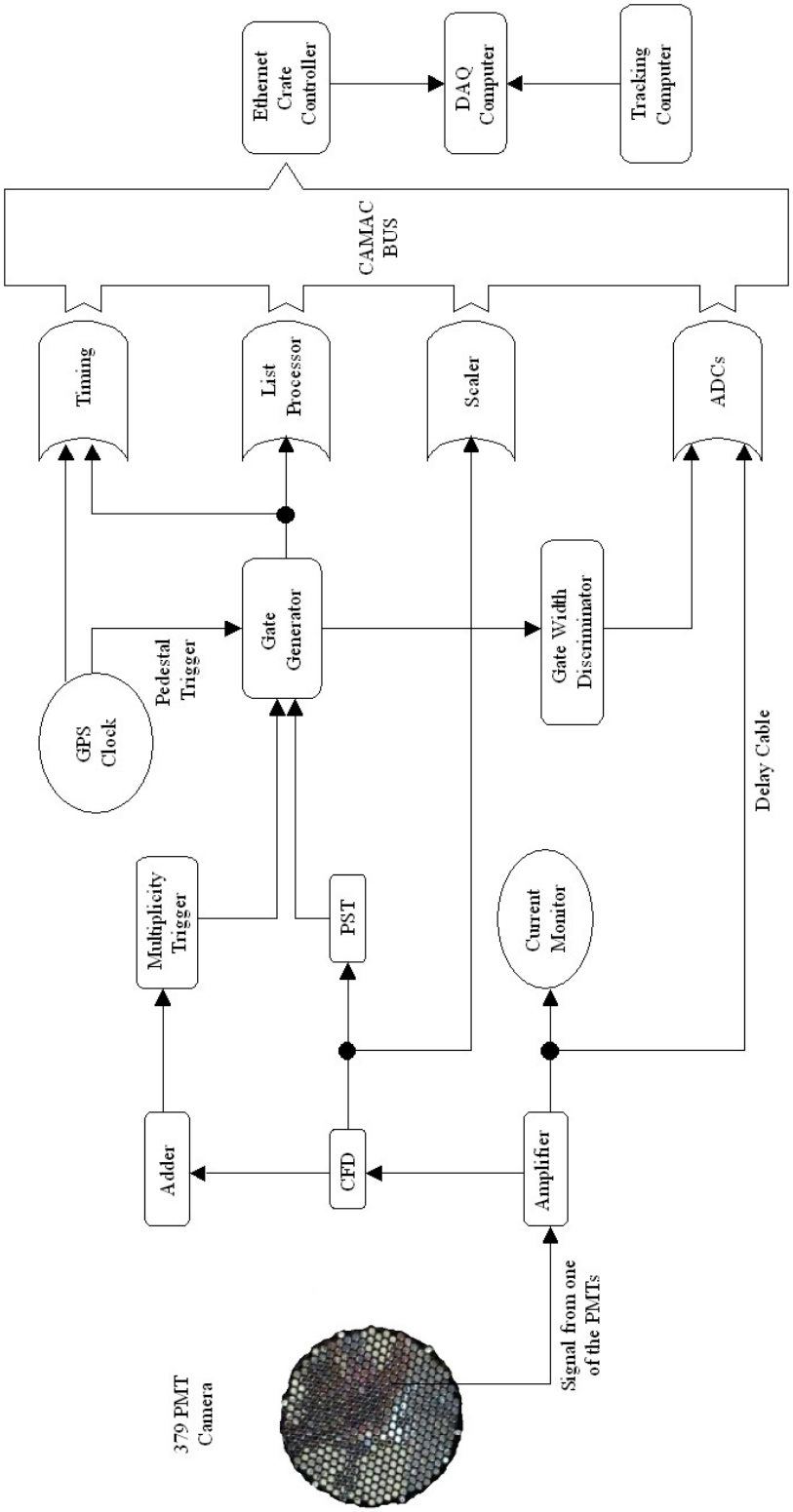

Figure 3.6: Data acquisition (DAQ) system for the Whipple 10m telescope.

PMTs in the absence of a real Cherenkov signal. These events are tagged so that they may be distinguished from real Cherenkov events; they are used to determine the mean pedestal value for each ADC. For analysis of Cherenkov events, the mean pedestal value is subtracted from the digital count value for each PMT. The pedestal variance is the spread of artificially-triggered ADC values and is a measure of the night-sky brightness fluctuations. A high or low pedestal variance for a PMT can be suggestive of a problem, either a hardware problem or the presence of a bright star in the field of view, and such PMTs are excluded from the subsequent analysis.

3.3.2 Nitrogen Run

The camera is an array of PMTs, whose characteristics (especially the gain) will not be uniform across the camera even if the PMTs are of the same model. A "nitrogen run" is used to overcome this problem by determining the relative gains of the PMTs. A nitrogen run consists of a one-minute exposure of the camera to optical flashes at a rate of $\sim$ 750 Hz from a nitrogen discharge lamp, positioned at the centre of the reflector. The light from the nitrogen lamp uniformly illuminates the camera and the duration of each flash is of the same order as that of atmospheric Cherenkov flashes. The signals from the PMTs will show a spread of values. The mean response of each PMT is compared with the overall mean response of all the PMTs, to give a "relative gain" value for each PMT across the camera. These relative gain values are then applied to observational data recorded on the same night to remove the effects due to the differing gains of the PMTs.

3.3.3 Zenith Run

A zenith run is a 10-minute observation recorded with the telescope positioned at an elevation close to zenith (90°). Zenith runs are used to determine the relative throughput or transparency for the night sky and as a check on overall system performance.

3.3.4 Pointing Check

The pointing accuracy of the telescope is checked nightly. This is achieved by pointing the telescope at a bright star close to an observation target, and noting the effect on the currents in the camera PMTs.

3.3.5 Operator Monitoring

Since the telescope moves on an alt-azimuth mount, stars in the field of view of an object under observation rotate in the camera plane as the object is being tracked across the night sky. In the case of bright stars, the movement must be monitored so that PMTs can be switched off if the currents become excessive. Failing to do so can result in photocathode damage or non-linear response in the PMTs.

3.4 Observing Methodology

Observing with the Whipple 10-metre telescope is dependent on the weather and on sky brightness. Optimum conditions for observing are clear, dark, moonless nights. Therefore, there are only approximately three weeks in every lunar cycle in which useful observations can be taken. The duration of these three weeks is known as a "dark run".

During a dark run, adverse weather conditions may also have an impact on the telescope and limit observing. No observations are made at wind speeds greater than $\sim$ 50 km/hour as steady observations cannot be made reliably and there is a danger of shear in the telescope structure. Lightning can also damage the telescope and as such no observations are made during the summer months when lightning storms are frequent. Overhanging cloud represents a great hindrance for observing Cherenkov light, as shown by Dowdall (2003). Cherenkov light can be absorbed by water vapour and the greater the content of water vapour in the atmosphere, the less likely it is that the telescope will detect Cherenkov flashes. Humidity also has a major influence on observing: high humidity can lead to arcing in the camera because of the high voltage ($\sim$

1000 V) between the anode and cathode in the PMTs.

When observations are possible, there are two alternative observing modes which may be employed: ON/OFF and tracking.

3.4.1 ON/OFF Mode

For an *ON* run the telescope is pointed at a gamma-ray source or potential source at a particular right ascension and declination. The telescope then tracks this position for approximately 28 minutes as the elevation and azimuth angles of the source change and the event data are recorded. Once the ON run is completed, the telescope is repositioned to right ascension thirty minutes less than that of the source being tracked but at the same declination. This allows for a two-minute slew time of the telescope, and a following 28-minute tracking of the new position which constitutes the *OFF* run. The data in the OFF run can then be used as a control in conjunction with the data recorded in the ON run to estimate and eliminate background due to non-gamma-ray Cherenkov events (e.g., cosmic rays) the subsequent off-line analysis (see Chapter 5). The gamma-ray signal, if present, is typically very weak, accounting for less than 1 % of the recorded events.

In some cases the OFF run is taken before the ON run at a right ascension 30 minutes *greater* than that of the source to be tracked. This may be done, for example, to facilitate recording of objects that would have a bright star in the field of view in an OFF run following the ON run.

3.4.2 Tracking Runs

A tracking run consists of an ON run with no corresponding following or preceding OFF run. This allows, for example, for continuous observation of a source whose characteristics may vary rapidly with time (such as flaring activity), where ON/OFF run observations could result in the loss of important time-profile information. Tracking runs are also used when night-sky conditions are considered to be poor. An OFF run may not be useful in a case where it

was known that the background rate was varying.

Control data for a tracking run can be derived from the ON-run data in conjunction with non-contemporaneous OFF-run data taken on the same source. All events which do not originate from the source direction are deemed to be background events. These events will be orientated randomly and will not point towards the centre of the camera. The orientation of these events is described using the parameter alpha (α), the angle between the major axis of the image and a line joining the image centroid to the centre of the camera (see Figure 5.2).

Figure 3.7 shows a plot of α distribution of events per 5° bin from the Crab Nebula. It can be seen that from $\sim$ 10° to 90°, the α-plots for ON and OFF runs match reasonably well, indicating that the background events for both runs are similar. If the ratio of events in the $20° - 65°$ region to those in the $0° - 15°$ region is known for the *OFF* run, then the number of background events expected in the $0° - 15°$ region for the *ON* run can be calculated from the events in the $20° - 65°$ region of the same run. This assumes that the shape of the α-plot is reasonably consistent and stable. The ratio of the number of events in the $0° - 15°$ region (N_{0-15}) to the number of events in the $20° - 65°$ region (N_{20-65}) for OFF runs defines a tracking ratio (R_{track}) given by:

$$R_{track} \pm \Delta R_{track} = \frac{N_{0-15}}{N_{20-65}} \pm \sqrt{\frac{N_{0-15}}{N_{20-65}^2} + \frac{N_{0-15}^2}{N_{20-65}^3}} \tag{3.1}$$

Once the tracking ratio has been established from a large number of OFF runs, it can be used to estimate the number of background events (N_{OFF}) in an unpaired ON (tracking) run as:

$$N_{OFF} = N_{ON}(20° - 65°) \times R_{track} \tag{3.2}$$

where $N_{ON}(20° - 65°)$ is the number of events in the ON run between $20° - 65°$.

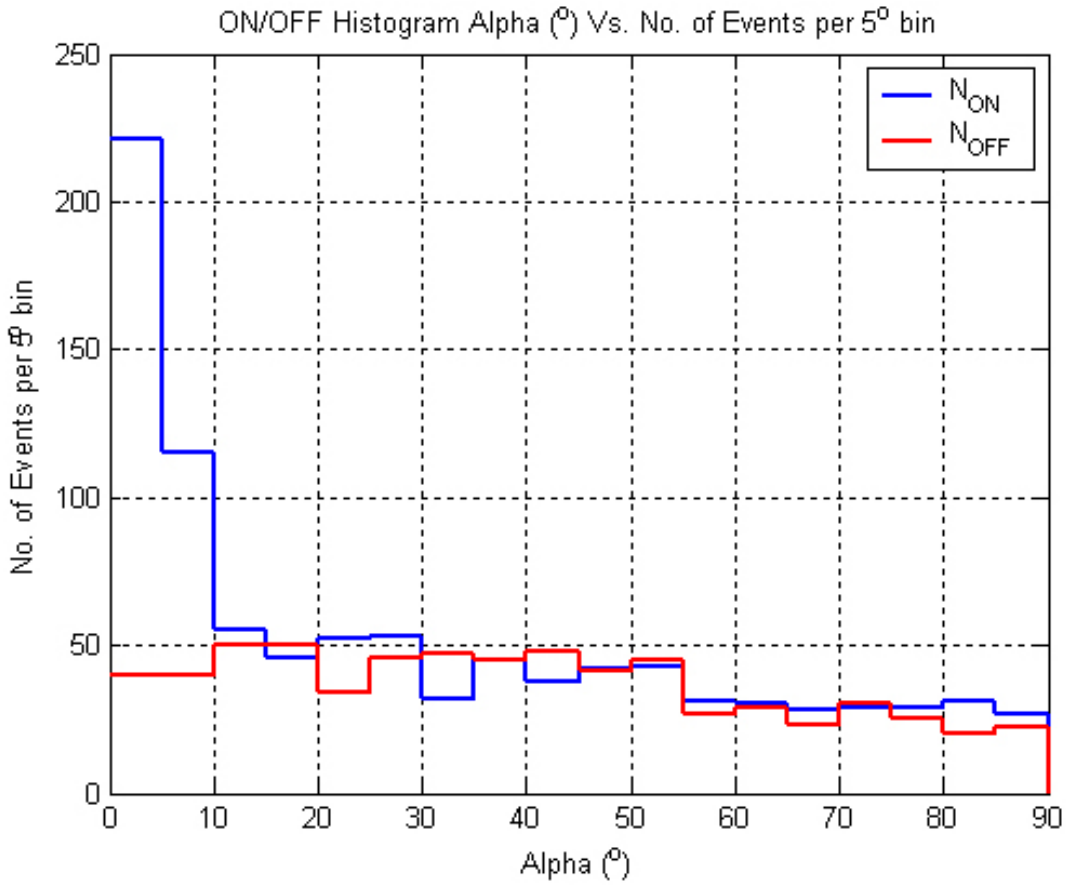

Figure 3.7: Sample α distribution plot of events per 5° bin from the Crab Nebula. Gamma-ray events will be orientated towards the centre of the camera, corresponding to small values of α. This distribution has an excess of events orientated within 10° of the centre of the camera indicating the presence of gamma rays from the source being observed.

Chapter 4

Active Galactic Nuclei and Starburst Galaxies

4.1 Introduction

Among the most extreme types of galaxy in the universe are active galactic nuclei (AGN). These are galaxies with a bright central nucleus which has a luminosity that outshines the billions of other stars which make up the galaxy. AGN make up about 1 % of all galaxies. AGN emit radiation across the entire range of the electromagnetic spectrum from radio waves to gamma rays and are characterised by non-thermal emission, broad emission lines, jet-like streams emanating from the poles of the central core of the nucleus and high, rapidly-varying luminosity. The intensity of this radiation is variable at all wavelengths and can vary on timescales from hours to years.

Current models of AGN structure are based on the idea of a supermassive black hole of approximately $10^6 - 10^8$ $M_\odot$ [1] located at the centre of the galaxy. If the the black hole is spinning whilst material is accreting onto it, energy may be extracted from it electromagnetically, giving rise to powerful jets propagating at relativistic speeds along the rotation axis. Using this model, it is possible to explain the different characteristics of AGN taking into account the differing observing angles, whether side-on or face-on views of these galaxies.

[1] $M_\odot$ = the mass of the Sun : 1.98×10^{30} kg.

4.2 AGN Types and Properties

Active galactic nuclei known as Seyfert galaxies were among the first AGN to be discovered. Seyfert galaxies are spiral galaxies and have been divided into two types, Seyfert I and Seyfert II. Seyfert I galaxies have broad emission lines, indicating hot and violent activity. Seyfert II galaxies have narrow emission lines implying cooler and less turbulent activity than their type I counterparts. Furthermore, Seyfert I galaxies have strong UV and X-ray emission whilst Seyfert II galaxies are more pronounced at IR wavelengths. In some broad emission line AGN, it is impossible to distinguish the host galaxy from the central bright nucleus. These galaxies are known as quasistellar objects (QSOs) or "quasars" and are believed to be Seyfert I type galaxies that either have a central core which has a brightness that outshines the surrounding galaxy or are so far away that the galaxy cannot be resolved from the central galactic core.

Based on radio observations, galaxies have been categorised as being either radio-loud or radio-quiet depending on their radio power. All Seyfert galaxies are radio-quiet as are approximately 90 % − 95 % of quasars. About 5 % − 10 % of quasars are radio-loud and fall in two categories: flat-spectrum radio quasars (FSRQs) and steep-spectrum radio quasars (SSRQs). FSRQs have a relatively flat spectrum in the GHz region, with spectral index $\alpha < 0.5$ in the 100 MHz to 30 GHz range. FSRQs tend to have a more compact core and high optical polarisation. SSRQs tend to have a radio spectrum with higher spectral index ($\alpha \geq 0.5$), and display more spatially extended emission which is generally associated with radio lobes. Unlike SSRQs, FSRQs exhibit superluminal motion (SL), a property which they share with BL Lacertae (BL Lac) objects. BL Lac objects and FSRQs are collectively referred to as "blazars" and are believed to have their relativistic jets orientated within a few degrees of our line of sight.

BL Lac objects are characterised by continuum optical spectra which are almost featureless, with very weak emission lines (if any), and they exhibit rapid optical variability. BL Lacs were at one time classified as "radio-selected BL Lacs" (RBLs) or "X-ray-selected BL Lacs" (XBLs), depending on how they

were first detected. A more recent classification describes BL Lacs as "high-frequency-peaked BL Lacs" (HBLs) or "low-frequency-peaked BL Lacs" (LBLs), depending on the position of the synchrotron peak in the spectral energy distribution.

Another type of AGN are radio galaxies classed as Fanaroff-Riley 1 (FR1) and Fanaroff-Riley 2 (FR2) depending on their radio morphology and power. FR1 galaxies have low luminosity ($L < 5 \times 10^{41}$ erg s^{-1}) and weaker optical emission, and their radio emission is mostly core-dominated. FR2 galaxies have high luminosity ($L \geq 5 \times 10^{41}$ erg s^{-1}), and their radio emission is more powerful toward the radio lobes.

4.3 Unification and Classification

AGN display many different properties, but it is possible that inherently similar AGN sources are being observed at different viewing angles and as such display different observational properties or characteristics. This suggests the need for a model which can unify apparently different classes of AGN.

From this unified model, it is possible to comprehend most of the different types of AGN in terms of different viewing angles and orientation. It is important to note that there are really two separate unification schemes by orientation: optical and radio. The optical scheme explains the presence or absence of broad-line emission by the orientation of the torus (see Figure 4.1), while the radio scheme explains the core-dominated (FSRQ) versus lobe-dominated (SSRQ) radio-loud AGN in terms of orientation with respect to the jet axis. The two schemes are related in that the axis of symmetry is almost certainly the same, but the viewing angle dependencies are quite different, one dominated by optical depth and structure of the obscuring dust and gas of the torus, the other by the beaming pattern of the relativistic jets, which depends on the Doppler factor (Urry, 2004). These considerations lead to relationships by viewing angle with respect to the jet direction and the observed properties of radio-loud and radio-quiet AGN.

Radio Loudness	Type 1 AGN	Type 2 AGN	Type 0 AGN
Radio-Quiet (85 % − 95 %)	Seyfert I QSO (90 % − 95 %)	Seyfert II	
Radio-Loud (5 % − 15 %)	BLRG FSRQ & SSRQ QSO (5 % − 10 %)	NLRG FR1 & FR2	Blazars BL Lac & FSRQ

Decreasing angle to the line of sight $\longrightarrow$

Table 4.1: AGN Taxonomy: A unified scheme classification system for active galactic nuclei, after Padovani (1997).

In this context, AGN may be subdivided into three classes depending on their optical and radio spectra. AGN with broad emission lines and bright continua, presumably from hot, high-velocity gas situated near to the black hole, are classified as Type 1 AGN. These include Seyfert I galaxies, quasars and broad-line radio galaxies (BLRG), encompassing FSRQs and SSRQs. In Type 1 AGN, there is believed to be an unobscured view of the core of the galaxy. AGN with narrow emission lines and weak continua are classified as Type 2 AGN. These include Seyfert II galaxies, narrow-line radio galaxies (NLRG), and FR1 and FR2 galaxies. In Type 2 AGN it is likely that there is no high-velocity gas present or that the line of sight to the galactic centre is obscured by cooler dust and gas or by the surrounding torus. Finally, AGN with unusual spectral characteristics are classified as Type 0 AGN. These include BL Lacs and many FSRQs. The primary difference between BL Lacs and other AGN is the lack of strong absorption or emission lines. This may indicate the absence of high-velocity clouds or the presence of relativistically beamed radiation in the jets (Quinn, 1997).

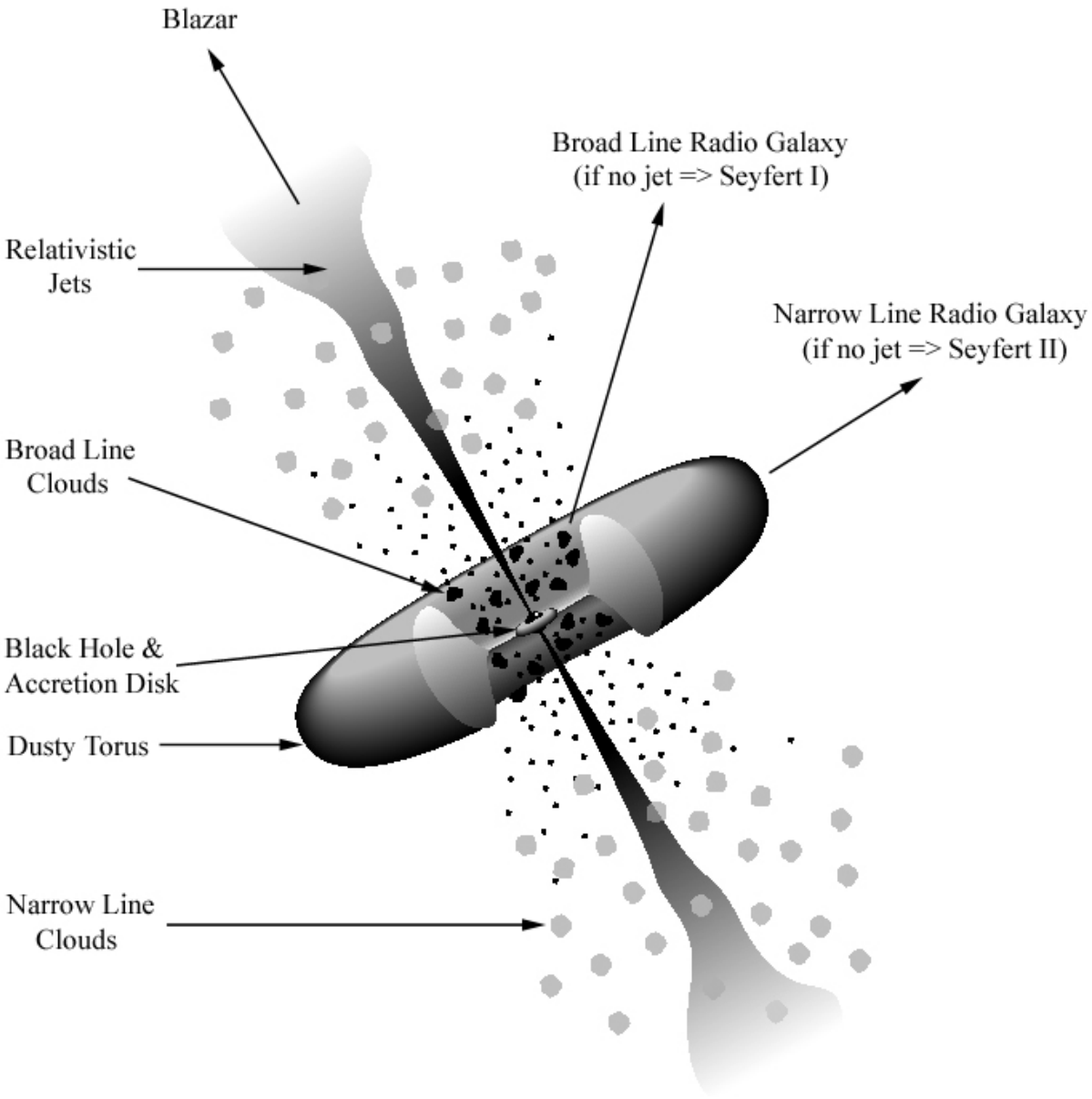

Figure 4.1: A schematic diagram of the current model for radio-loud AGN. Surrounding the central black hole is a luminous accretion disk. Broad emission lines are produced in clouds (dark blobs) orbiting above and below the accretion disk. A thick dusty torus obscures the broad-line region from transverse lines of sight. Narrow emission lines are produced in clouds (grey spots) much further from the central source. Radio jets, which emanate from the poles of the black hole, travel at relativistic speeds. From this unified model, it is possible to comprehend most of the different types of AGN in terms of different viewing angles and orientation (after Urry and Padovani (1995)).

4.4 The Standard AGN Model

The enormous energy emanating from AGN is believed to result from accretion of matter onto the compact body of a central core.

4.4.1 The Accretion Model

Consider a central compact core of mass, m, and radius, r, surrounded laterally by a stationary cloud of matter gravitationally attracted to the central core. If an element of mass, Δm, is accreted from the cloud of matter onto the central core, it must also deposit all of its gravitational energy, $\frac{Gm\Delta m}{r^2}$, onto the central core, where G is the gravitational constant and r is the radius of the central core. To maintain thermal equilibrium, the central core must radiate this energy. The gravitational energy deposited onto the central core is enormous and as a result the light radiated from the central core of some AGN is so intense that the surrounding star systems making up the AGN cannot be resolved from the central galactic core or nucleus.

The luminosity, L, of the central core may be written in terms of the gravitational energy deposited, ΔE, as

$$L = \frac{\Delta E}{\Delta t} = \frac{Gm\Delta m}{r^2 \Delta t} \tag{4.1}$$

where the central core accretes mass Δm in time Δt. From this it can be seen that the luminosity of the central core is proportional to the rate of change of its rest mass. This equation also implies that the more compact the central core, the greater the luminosity.

The compact object occupying the central core of AGN is postulated to be a supermassive black hole with mass in the range 10^6 $M_\odot$ $-$ 10^8 $M_\odot$. Although other types of central bodies have been suggested, black holes appear to be the most reasonable assumption for producing such large amounts of energy in such small and compact volumes.

4.4.2 Relativistic Jets

Relativistic jets emanate from both poles of the AGN and as such are orientated perpendicular to the accretion disk (see Figure 4.1). The emission of very high energy photons is due to shocks in the jet. The radiation is primarily synchrotron radiation in the radio band and Compton-upscattered emission off either the synchrotron radiation or external optical/UV photons at shorter wavelengths. When the emitting region has a bulk relativistic motion relative to an observer, the emission appears beamed towards the observer. A measure of the strength of the beaming toward a fixed observer is the Doppler factor ,δ, defined by:

$$\delta = \frac{1}{\gamma\left(1 - \beta\cos\theta\right)} \tag{4.2}$$

where $\gamma = (1-\beta^2)^{-\frac{1}{2}}$ is the Lorentz factor of the jet, $\beta = \frac{v}{c}$ and θ is the angle of the jet with respect to the line of sight. The Doppler factor is highly dependent on the angle between the jet and the observer's line of sight and is at a maximum ($\delta = \sqrt{\frac{1+\beta}{1-\beta}}$) at $\theta = 0^\circ$ with the jet pointing directly towards the observer. As an example, for $v = 0.995\ c$, $\gamma \sim 10$ and $\theta = 0^\circ$, the Doppler factor is ~ 20. For $\theta = 5^\circ$, this drops to $\delta \sim 11$. Therefore, the flux luminosity and photon energy seen by the observer can become very high for head-on observation, consistent with the idea that the observed properties of AGN are dependent upon viewing angle.

The bulk Lorentz factor varies for different models and conditions but leads to considerable relativistic beaming of radiation along the jet direction. Observational evidence for relativistic beaming includes detection of very high energy gamma radiation and apparent superluminal motion. Superluminal motion is a term which describes a source with an apparent velocity greater than the speed of light ($v > c$). This phenomenon can occur for emitting regions moving at high speeds ($v \rightarrow c$) at small angles to the line of sight, creating the illusion that a source is travelling faster than the speed of light when in fact a relativis-

tic source is following its own relativistic emission at small angles to the line of sight of the observer. An example of a relativistic jet is seen in Figure 4.2, which is a Hubble telescope image of the AGN M 87. The relativistic jet in Figure 4.2 originates from a disk of superheated gas swirling around a central black hole and is propelled and concentrated by the intense, twisted magnetic fields trapped within this matter. The light from the jet is synchrotron radiation produced by electrons spiralling around magnetic field lines in the jet. M 87 is 50 million light-years from Earth and is one of the nearest and most well-studied extragalactic jets.

Proton models have also been proposed to account for gamma radiation from relativistic jets (Mannheim, 1993). In these models, protons are accelerated to energies of 10^{18} eV at shock fronts propagating along the jet (Biermann and Strittmatter, 1987). These protons interact to produce neutral pions, which give rise to gamma radiation (Equation 1.14).

4.5 Starburst Galaxies

A starburst galaxy (SBG) is a galaxy which is currently experiencing a period of intense star-forming activity. This star-forming activity may last for several millions of years or more, which is still very small compared to the overall lifetime of a galaxy. During a starburst, stars can form at a rate tens or even hundreds of times greater than the star formation rates in normal galaxies. The starburst may occur over a region only a few thousand light-years in diameter. Many of the newly-formed stars are extremely massive and very bright, and as a result SBGs are among the most luminous galaxies in the Universe.

The most popular theory for the cause of a starburst is that it is triggered by a close encounter or collision with another galaxy. This collision sends shock waves through the galaxy. These shock waves interact with giant molecular clouds of gas and dust within the galaxy, causing them to collapse and form perhaps hundreds of stars. The most massive of these stars use up their fuel quickly and explode as supernovae, producing more shock waves and further

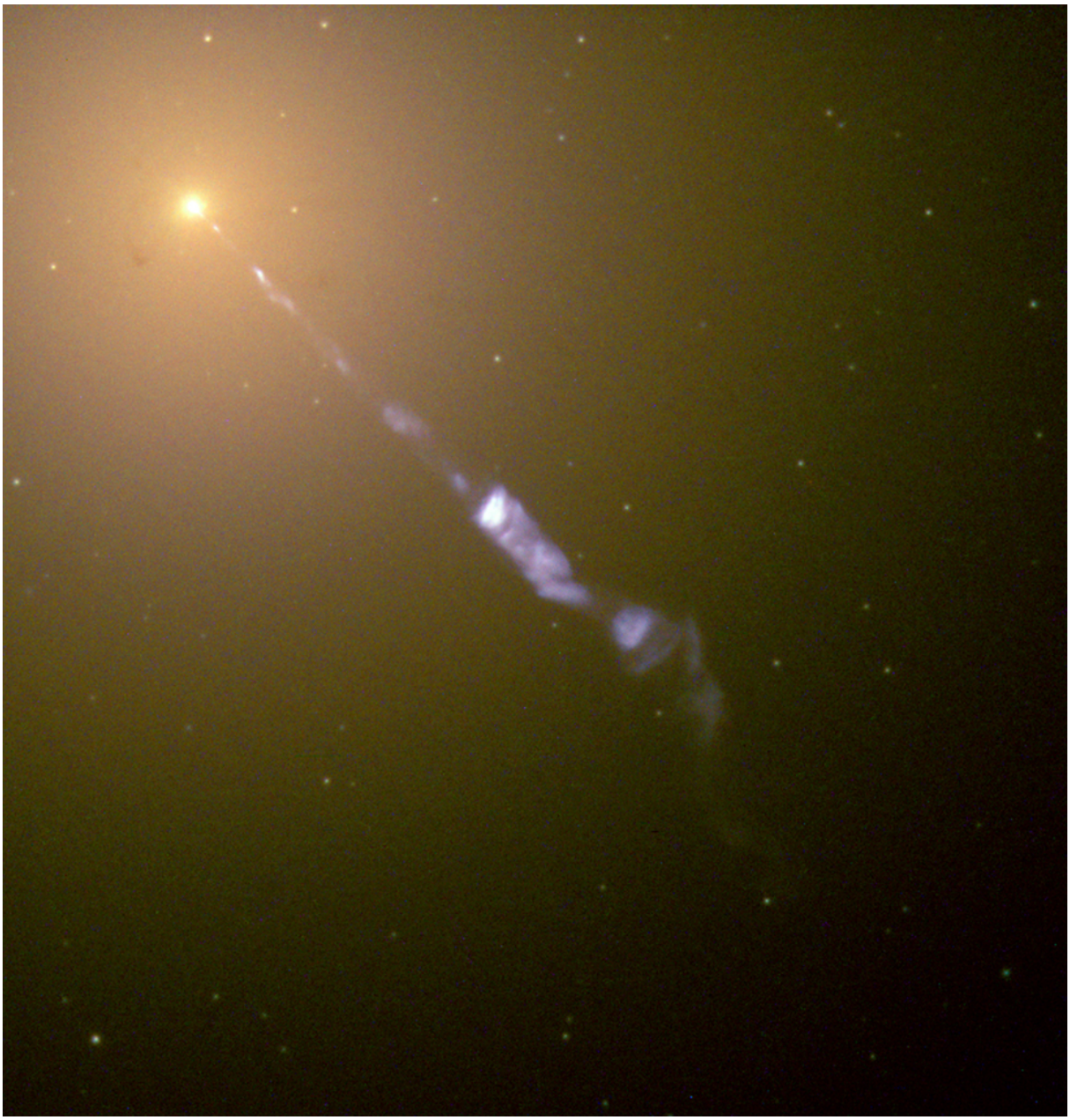

Figure 4.2: A Hubble telescope image of the AGN M 87. Image credited to NASA and The Hubble Heritage Team (STScI/AURA), (http://hubblesite.org/newscenter/archive/releases/2000/20/).

star formation. In this way, a chain reaction of star formation and supernova explosions can sweep through the central region of a galaxy, where most of the gas is located. The starburst ends when most of the gas has been used up or dissipated by the explosions.

Many of the new stars may remain surrounded by dust and gas for millions of years. Their light is absorbed by the dust, which radiates away the energy as infrared (IR) radiation. The rapid rate of supernova explosions in these galaxies produces expanding bubbles of gas at temperatures of millions of degrees. When the starburst is sufficiently intense, it can create a "superbubble" so hot and energetic that it expands out of the galaxy in what is called a superwind. Superwinds are thought to contain carbon, nitrogen, oxygen, iron and other heavy elements dispersed by supernova explosions and to be responsible for spreading these elements into intergalactic space.

Regions that currently are or have been subject to a strong process of star formation are good candidates for gamma-ray emission. They have large amounts of target material, and multiple shocks due to the presence of supernova remnants and the powerful stellar winds of their numerous young stars can accelerate particles to relativistic energies. They may even be sites where ultra high energy cosmic rays are produced.

4.5.1 Galaxies with High Star-Formation Rates

Although galactic cosmic rays (protons and nuclei) are widely believed to be mainly accelerated by the winds and supernovae of massive stars, definitive evidence of this origin remains elusive nearly a century after their discovery. The active regions of starburst galaxies have exceptionally high rates of star formation, and their large size, more than 50 times the diameter of similar regions in our Galaxy, uniquely enables reliable calorimetric measurements of their potentially high cosmic-ray density. The cosmic rays produced in the formation, life and death of massive stars in these regions are expected to produce diffuse gamma-ray emission through interactions with interstellar gas and radiation

(Acciari et al., 2009a).

The large masses of dense interstellar gas and the enhanced densities of supernova remnants and massive young stars expected to be present in such galaxies would suggest that SBGs, luminous infrared galaxies (LIRGs) and ultra-luminous infrared galaxies (ULIRGs) could have gamma-ray luminosities orders of magnitude greater than normal galaxies. Such environments will typically emit a large amount of infrared radiation, because abundant dust absorbs the UV photons emitted by the young massive stars and re-emits the energy as infrared radiation. Therefore, the infrared luminosity of a galaxy can be an indication of star formation taking place in it (Torres and Domingo-Santamaría, 2005). As an example, Figure 4.3 shows the SBG IC 342, a late-type spiral galaxy, located in the Maffei Group in the northern constellation of Camelopardalis. IC 342 is seen face-on and lies in a direction close to the plane of our own Milky Way Galaxy.

The most luminous galaxies in the infrared band are among the powerful galaxies known. LIRGs have been identified as a class, selected for emitting more energy in the far infrared ($\sim$ 50 μm $-$ 500 μm) than in all other wavelengths combined. LIRGs are defined as galaxies with infrared luminosities larger than 10^{11} $L_{\odot}$ [2]. Those with $L_{IR} > 10^{12}$ $L_{\odot}$ are called ULIRGs whilst those with $L_{IR} > 10^{13}$ $L_{\odot}$ are called Hyper-Luminous Infrared Galaxies (HyLIRGs) (Sanders and Mirabel, 1996). LIRGs are the dominant population of extragalactic objects in the local Universe, with ULIRGs the most luminous local objects. Current understanding of LIRGs and ULIRGs suggests that they arise from recent galaxy mergers in which much of the gas of the colliding objects, particularly that located at distances less than $\sim$ 5 kpc from each of the pre-merger nuclei, has fallen into a common centre (typically less than 1 kpc in extent), triggering a huge starburst (Melnick and Mirabel, 1990). The size of the inner regions of ULIRGs where most of the gas is found can even be as small as a few hundred parsecs. LIRGs not only possess a large amount of molecular gas,

[2] $L_{\odot}$ = the luminosity of the Sun: 3.839 $\times$ 10^{33} erg s^{-1} or 3.839 $\times$ 10^{26} W.

Figure 4.3: The starburst galaxy IC 342. Image taken from http://apod.nasa.gov/apod/ap080109.html.

but a large fraction of it is at high density. This increases the chances of star formation and of cosmic-ray production. These regions are larger than giant molecular clouds but have densities found only in small cloud cores and appear to be the largest star-forming regions in the local Universe. The cosmic-ray production rate in these regions can significantly exceed the average rate for the galaxy. No LIRGs or ULIRGs (or any other SBG) were detected in gamma rays by EGRET: upper limits were established for M 82, $F(E > 100 \text{ MeV}) < 4.4 \times 10^{-8}$ photons cm^{-2} s^{-1}, and NGC 253, $F(E > 100 \text{ MeV}) < 3.4 \times 10^{-8}$ photons cm^{-2} s^{-1} (Blom et al., 1999), the two nearest starburst galaxies. However, the Fermi-LAT has very recently detected M 82 (6.8 σ) and NGC 253 (4.8 σ) above 200 MeV (Abdo et al., 2010).

4.5.2 Molecular Clouds

Molecular clouds are regions in which the gas is mostly in molecular form; they behave as self-gravitating, magnetised, turbulent, compressible fluids. The main constituent of molecular clouds is molecular hydrogen (H_2). Molecular hydrogen is difficult to detect by infrared and radio observations, so the molecule most often used to determine the presence of H_2 is CO (carbon monoxide). The ratio between CO luminosity and H_2 mass is thought to be constant. Almost all known molecular clouds in the Milky Way Galaxy are detectable through CO emission. Giant molecular clouds have masses $\gtrsim 10^4$ $M_\odot$, are generally gravitationally bound and may contain multiple sites of star formation (Williams et al., 1999).

Mechanisms proposed for the formation of molecular clouds can be divided into three general categories: collisional agglomeration of smaller clouds, gravimetrically thermal instability and pressurised accumulation in shocks, either in supernova explosions or in galactic shocks (Blitz and Williams, 1999). It has been proposed that giant molecular clouds (GMCs) have form by coagulation of pre-existing molecular clouds and atomic gas through instability and/or large scale shocks. In high-density regions, where the vast majority of hydrogen is in molecular form, it seems likely that molecular clouds form from the coagulation of smaller clouds, whereas in the outskirts of galaxies where the gas is predominantly atomic the compression of gas in spiral density shock waves provides a more plausible formation mechanism.

It was thought that GMCs were long-lived, gravitationally-bound objects. The presence of supersonic turbulence (possibly powered by supernova explosions and the large-scale dynamics of the galactic disk itself) ensures that clouds do not immediately collapse to form stars, as this would predict a star-formation rate for the Milky Way Galaxy far higher than that observed. Locally unstable clumps, which build up their mass through competitive accretion, collapse to form protostars.

The current theory of cloud formation, and subsequently star formation, in

disk galaxies suggests that supersonic turbulence, generated by a combination of galactic rotation and supernova explosions, regulates the formation of protostellar cores inside the GMCs. Observationally, some of these clouds convert a small fraction of their mass into stars, before the cloud itself is destroyed by a combination of stellar feedback and the turbulence that built the cloud in the first place. Molecular clouds appear to be transient objects, representing the brief molecular phase during the evolution of dense regions formed by compressions in the diffuse gas, rather than long-lived, equilibrium structures (Ballesteros-Paredes et al., 2006). The low star-formation efficiency of molecular clouds may be due to the fact that they are short-lived (Booth et al., 2007).

Nevertheless, two questions related to the formation of GMCs have been settled in the last decade:

1. GMCs have lifetimes of $2 \times 10^7 < \tau < 1 \times 10^8$ yr, considerably shorter than a galactic rotation period.

2. In galaxies with strong, well-defined spiral arms, molecular clouds are generally confined to the spiral arms (Blitz and Williams, 1999).

Although molecular clouds are, by definition, regions in which the gas is primarily molecular by mass, much of the volume of such a cloud is not molecular. That is, the filling fraction of molecular gas can be as low as ~ 20 % and the cloud is inhomogeneous with large density variations from one location to another. The structure of molecular clouds reflects the conditions from which they form and determines the mass scale of stars which form from them (Blitz and Williams, 1999).

Molecular clouds are generally not in equilibrium, but tend to evolve secularly. They start as atomic gas that is compressed, increasing its mean density. The atomic gas may or may not be initially self-gravitating, but in either case compression causes the gas to cool via thermal instability and to develop turbulence via dynamical instabilities. Thermal instability and turbulence generates a range of substructures promoting fragmentation within the molecular cloud.

This builds a mass spectrum of proto-cores, some of which will collapse under their own gravity to form stars. Even though the self-gravity of the cloud as a whole is increased due to cooling and the compression, the free-fall time in the fragments is shorter. This ensures that collapse proceeds locally within the cloud, preventing monolithic collapse of the cloud. Only cores dense enough that self-gravity can overcome their magnetic and thermal energy can collapse (Padoan and Nordlund, 2002). This consideration prevents very low mass cores from forming stars and thus reduces the star-formation efficiency (Ballesteros-Paredes et al., 2006). The local efficiency of conversion of molecular clouds into stars would seem to depend primarily on stellar feedback evaporating and dispersing the cloud, and only secondarily on the presence of magnetic fields. Therefore, magnetic fields appear unlikely to be of importance in the structuring of molecular cloud cores, although they probably are important in the number of cores created. In dense clusters, star formation might be affected by dynamical interactions. Close encounters between newborn stars and protostellar cores can modify their accretion history and thereby influence the final stellar mass, as well as the size of protostellar disks and their ability to form planets and planetary systems.

A young stellar population releases a lot of energy into its surroundings through stellar winds, ionisation and supernova explosions. When gravitational collapse proceeds to star formation, ionising radiation begins to act on the surrounding molecular cloud. This can drive compressive motions that accelerate collapse in surrounding gas, or raise the energy of the gas sufficiently to dissociate molecular gas. Even if these forms of energy release do not drive the observed turbulence in the molecular cloud, they may contribute to the destruction of the cloud and prevent further star formation.

From observational evidence, Elmegreen (2000) discussed the idea that GMCs are short-lived entities that form, make stars and disperse again on their dynamical time scale. This short time-scale alleviates the need for an internal energy source to sustain the observed internal supersonic turbulence. Interstel-

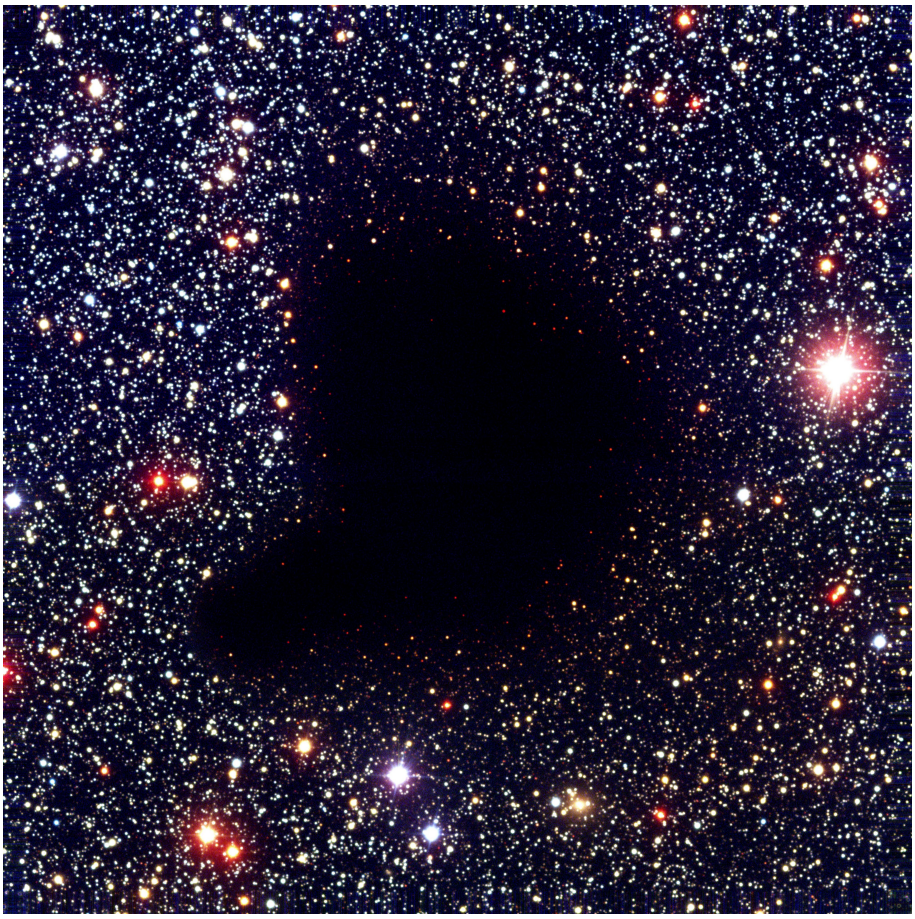

Figure 4.4: The Barnard 68 molecular cloud. Image taken from http://www.phys.ncku.edu.tw/~astrolab/mirrors/apod_e/ap060409.html.

lar turbulence seems to be driven from scales substantially larger than molecular clouds. Internal molecular cloud turbulence may well be a by-product of the cloud-formation mechanism itself, explaining why turbulence is ubiquitously observed on all scales.

An example of a molecular cloud can be seen in Figure 4.4. The Barnard 68 molecular cloud is a vast cloud of gas and dust located in the direction of constellation Ophiuchus at a distance estimated at 500 light-years from Earth. This cloud is so dense that it obscures the background stars. The association of molecular clouds with star formation is so strong that it is generally assumed that wherever there are young stars, one will always be able to find molecular gas (Blitz and Williams, 1999).

4.5.3 Molecular Emission

Gamma-ray measurements together with estimates of the gas content and photon field densities provide a tool to determine the cosmic-ray spectrum of the molecular cloud. This would in turn, provide an estimation of where gamma-ray production is most likely to occur within the molecular cloud. The interstellar hydrogen distribution (in its molecular form (H_2), atomic (HI), or ionised (HII)) is derived from radio surveys. H_2 has only a weak quadrupole signature and is not easily identified directly, but it can be traced from the emission lines of associated molecules that are radiatively or collisionally excited using appropriate calibrations or conversion factors. The most commonly used tracer for molecular hydrogen is the carbon monoxide molecule, CO (Dame et al., 2001). Although CO is much less abundant than H_2, it is a polar molecule with strong dipole rotational emission at millimetre wavelengths. CO is more easily traceable and its presence alongside H_2 is considered to be proportionally constant. Generally, the conversion factor between CO luminosity and molecular mass is estimated and constrained from measurements in our own Galaxy where masses of individual molecular clouds can be independently determined from cloud dynamics (Solomon et al., 1987).

Although CO traces most of the molecular gas mass in galaxies, it does not necessarily trace active star-forming regions where the gas density may be more than ten times higher than the average. These regions are better traced by high-dipole-moment molecules like HCN, CS and HCO^+. Consequently, these molecules have often been used as probes of physical conditions in giant molecular cloud cores. HCN and CS are probably the most frequently observed interstellar molecules after CO. Because of their higher dipole moments ($\mu \sim 2$ D-3 D)[3], they require about two orders of magnitude higher densities for collisional excitation than CO ($\mu \sim 0.1$ D). HCN is one of the most abundant high-dipole-moment molecules and can be used to trace molecular gas at densities $\eta(H_2)$

[3] μ = the electric dipole moment measured in units of debyes, D. The S.I. unit for μ is the coulomb metre, C m, where 1 C m = 2.9979×10^{29} D.

greater than $\sim 3 \times 10^4$ cm^{-3} compared to densities greater than ~ 500 cm^{-3} traced by CO (Gao and Solomon, 2004b). In general, the total FIR luminosity is a tracer of the star-formation rate, the CO luminosity is a measure of the total molecular gas content and the global HCN line luminosity is a measure of the total dense molecular gas content.

A tight linear correlation was found by Gao and Solomon (2004a) between the IR and HCN luminosities (L_{IR} and L_{HCN}) (in a log-log plot) with correlation coefficient $R = 0.94$, and an almost constant average L_{IR}/L_{HCN} ratio. The IR-HCN linear correlation is valid over three orders of magnitude including ULIRGs, the most luminous objects in the local Universe. The direct consequence of the linear IR-HCN correlation is that the global star-formation rate is linearly proportional to the mass of dense molecular gas in normal spiral galaxies, LIRGs and ULIRGs. This is strong evidence in favour of star formation as the power source in ULIRGs since star formation in these galaxies appears to be normal and as expected given the high mass of dense star-forming molecular gas.

The HCN-CO correlation is also much tighter than the IR-CO correlation. The non-linear correlation between L_{IR} and L_{CO} may be a consequence of the stronger and perhaps more physical correlations between L_{IR} and L_{HCN} and between L_{HCN} and L_{CO}. Thus, the star-formation rate indicated by L_{IR} depends on the amount of dense molecular gas traced by HCN emission, not the total molecular gas traced by CO emission. The HCN/CO ratio is an indicator of the dense molecular gas fraction and gauges the globally averaged molecular gas density. The HCN/CO ratio can therefore be a powerful starburst indicator. CO luminosity by itself leads to a rough prediction for IR luminosity that breaks down for LIRGs, especially for ULIRGs, whereas HCN luminosity is much better at predicting the IR luminosity for all galaxies including ULIRGs. Therefore, the star-formation rate indicated by L_{IR} in galaxies depends on the amount of dense molecular gas traced by L_{HCN}, not the total molecular gas content measured by CO. In particular, the IR-CO correlation may not have

a solid physical basis as it can be readily related to the stronger and perhaps more physical IR-HCN and HCN-CO correlations, which may be the origin of the correlation between IR and CO. This is reminiscent of the poor IR-HI correlation as compared with the better IR-CO correlation that became apparent two decades ago, when systematic CO observations of significant numbers of galaxies became available (Gao and Solomon, 2004a).

4.5.4 Superwinds

Superwinds are of cosmological interest as they transport large amounts of gas (in particular newly-synthesised heavy elements and energy) into the intergalactic medium (IGM). Quantifying this mass, metal and energy transport in local starburst galaxies is essential for understanding the significance of outflows from star-forming galaxies integrated over the history of the Universe. However, even the basic physical properties of local superwinds such as mass outflow rates, energy content, abundances and kinematics are uncertain. Measuring the physical properties of the hot gas driving these outflows is of crucial importance for several simple reasons (Strickland et al., 2000): the hot gas efficiently transports the majority of the energy in the outflow contains most of the newly-synthesised metals and ultimately controls the ejection of mass from the galaxy (although the majority of the mass of the outflow may be in ambient interstellar material swept up by the wind, this gas is accelerated to high velocity by the hot, fast wind).

The SBG NGC 253 is seen almost perfectly edge-on (see Figure 4.5), ideally oriented for studying the superwind as it flows out into the galaxy halo. Physical, morphological and kinematic evidence for the existence of a galactic superwind has been found for NGC 253 (Strickland et al., 2000; Weaver et al., 2002; Sugai et al., 2003). This superwind creates a cavity of hot ($\sim 10^8$ K) gas with cooling time longer than the typical expansion timescales. As the cavity expands, a strong shock front is formed at the interface with the cool interstellar medium. Shock interactions with low-density and high-density clouds can

produce X-ray continuum and optical line emission, respectively. The shock velocity can reach thousands of km s^{-1}. This wind has been proposed as the convector of particles which have been already accelerated in individual supernova remnants, to the larger superwind region, where Fermi acceleration could upgrade their energy up to that detected in ultra high energy cosmic rays (Torres and Anchordoqui, 2004; Domingo-Santamaría and Torres, 2005).

4.5.5 Diffuse Gamma-Ray Emission from Starburst Galaxies

The diffuse gamma-ray emission observed from a galaxy basically consists of three components:

- the truly diffuse emission from the galactic interstellar medium (ISM) itself
- the extragalactic background
- the contribution of faint, unresolved, point-like sources that belong to the galaxy or are beyond it but in the same line-of-sight by chance.

The galactic diffuse emission generated in interactions with the ISM has a wide energy distribution and normally dominates the other components. Gamma rays are thus mostly produced in energetic interactions of particles with the interstellar gas and the radiation fields present in the galaxy. The diffuse gamma-ray emission at high energies mainly comes via neutral pion production from the interaction of high-energy cosmic-ray nucleons with gas nuclei. Contributions from energetic cosmic-ray electrons interacting with the ambient photon fields via inverse-Compton scattering and with the matter field of the galaxy via relativistic Bremsstrahlung become more important below 100 MeV (Torres and Domingo-Santamaría, 2005).

The standard picture of gamma-ray production via cosmic-ray interactions seems more plausible given the rapidly growing knowledge about SBGs in other wavelength ranges, principally in terms of supernova explosion rates and the

Figure 4.5: A high-resolution image of the starburst galaxy NGC 253 This image was taken at San Esteban, Chile (http://www.astrosurf.com/antilhue/ngc_253_hires.htm).

total gas mass in the starburst region. The relevant cosmic-ray interactions are: inelastic collisions of relativistic nuclei with thermal gas nuclei producing π^0 mesons which decay into gamma rays, inverse-Compton collisions of relativistic electrons with ambient low-energy photons and Bremsstrahlung from collisions of such electrons with gas nuclei.

The gamma-ray flux from these processes is proportional to the density of the relativistic particles. The cosmic-ray density is determined by the strength of the cosmic-ray accelerators in the starburst region, and by the propagation modes and energy losses of the cosmic rays. Propagation of cosmic rays via convection in the starburst wind is a key process in gamma-ray production.

The enhanced cosmic-ray density and the very high gas and photon densities in the starburst regions are related to each other. The high gas densities are necessary for the high star-formation rates which produce massive, high-luminosity stars. Their subsequent supernova explosions heat the gas and generate cosmic rays. Together the heating of the gas and the high cosmic-ray density drive a mass outflow in the form of a galactic wind (Aharonian et al., 2005b).

Nearby starburst galaxies and luminous infrared galaxies with high levels of star formation are prime candidates to constitute a new population of high-energy gamma-ray emitters. Recent calculations by Persic et al. (2008) predicted that M 82 would be detectable by VERITAS and MAGIC with an integrated flux of $F(E \geq 100 \text{ GeV}) \sim 2 \times 10^{-12} \text{ cm}^{-2} \text{ s}^{-1}$ and by Fermi-LAT with an integrated flux of $F(E \geq 100 \text{ MeV}) \sim 10^{-8} \text{ cm}^{-2} \text{ s}^{-1}$. VERITAS detected M 82 at $F(E > 700 \text{ GeV}) = (3.7 \pm 0.8_{\text{stat}} \pm 0.7_{\text{syst}}) \times 10^{-13} \text{ cm}^{-2} \text{ s}^{-1}$ with a significance of 4.8 σ (Acciari et al., 2009a), and as stated in Section 4.5.1, the Fermi-LAT has also detected M 82 with a significance of 6.8 σ (Abdo et al., 2010).

4.5.6 History and Source Overview: NGC 253

NGC 253 is located at a distance of 2.58 ± 0.7 Mpc (Puche and Carignan, 1988; de Vaucouleurs, 1978; Turner and Ho, 1985) with a visual size of 0.3° from Earth

(Itoh et al., 2003b) and it is a nearly edge-on (inclination 78°) barred Sc galaxy (Torres and Domingo-Santamaría, 2005). It has a high supernova rate of $\leq$ 0.3 yr^{-1} derived from high-resolution radio continuum images (Ulvestad and Antonucci, 1997).

Radio Observations

Radio observations of starburst galaxies within a few Mpc of our Galaxy offer the best opportunities for detailed high spatial resolution studies and the best chance to detect and resolve individual objects within the active starburst regions. Of special interest at radio wavelengths are populations of compact sources, both thermal (i.e., HII regions) and non-thermal (i.e., supernova remnants). Numerous studies of the radio emission from NGC 253 have been reported. From Very Large Array (VLA) observations (Very Large Array Webpage, 2008), it has been estimated that within NGC 253, approximately half of the compact radio sources are dominated by thermal emission and the remainder are likely to be supernova remnants (Ulvestad and Antonucci, 1997).

The dynamics of the HI gas in NGC 253 were studied by Koribalski et al. (1995). Carilli (1996) constructed the radio spectrum of the nuclear starburst region of NGC 253 at low resolution (33" $\times$ 21") and frequencies between 330 MHz and 15 GHz, finding a flattening of the spectrum below 1.6 GHz. Of a number of possible explanations for the observed spectrum, the free-free absorption by gas local to the starburst region is most likely, with emission measures for the absorbing gas of $\sim 3 \times 10^5$ $(T/10^4\ \mathrm{K})^{3/2}$ pc cm^{-6}. Carilli (1996) finds that the free-free absorption interpretation is consistent with other observations that suggest the presence of high interstellar pressures in the starburst region of NGC 253.

X-Ray Observations

In principle, X-ray observations of the thermal emission from hot gas in superwinds can be used to measure the properties of the hot gas. Strickland et al. (2000) has found bright diffuse soft X-ray emission (0.3 keV $-$ 2.0 keV),

emerging from the nuclear starburst region of NGC 253, extending away from the plane of the galaxy to the south east and north west of the galaxy for a distance of $\sim$ 900 pc and $\sim$ 450 pc respectively (assuming $D = 2.6$ Mpc). This starburst driven superwind has previously been traced out to $\sim$ 9 kpc from the nucleus by Dahlem et al. (1998). Strickland et al. (2000) also found many soft X-ray point sources in the nuclear starburst region, presumably from high mass X-ray binaries or supernova remnants.

Hard X-ray emission (2.0 keV $-$ 8.0 keV) from NGC 253 is dominated by point-source emission. Several point-like sources were found in the central starburst region, although these are not the brightest X-ray sources in NGC 253. It was also found that there is no significant hard X-ray emission from the galaxy's southern outflow cone, which can be clearly seen in the soft X-ray band. The southern outflow cone is much softer (a higher flux of low-energy X-ray photons) than the diffuse emission from the starburst region, which itself is softer than the emission seen from the northern outflow on the far side of the disk.

Only $\leq$ 20 % of the observed X-ray emission comes from the volume-filling, metal-enriched wind fluid itself. This implies that the majority of the energy and gas (in particular the hot metal-enriched gas) transported out of NGC 253 by its superwinds cannot be seen even in X-ray emission. Strickland et al. (2000) argues that, if this is generally true for all starbursts, the majority of intergalactic medium heating and enrichment by starbursts may be currently invisible in X-ray emission and emphasises the importance of absorption line studies of the warm and hot gases in these galaxies.

Very complex X-ray emission has been found from galactic halos, especially in galaxies that are seen edge-on. Therefore, NGC 253 provides an almost perfect candidate for unobscured analysis of its halo emission. The best spatial resolution was provided by the Chandra observatory and Strickland et al. (2002) was first to publish a detailed case study of the diffuse X-ray and Hα emission in the halo of NGC 253. A statistically significant structure within the diffuse

emission on angular scales down to ~ 10" (~ 130 pc) was found. The spectrum of the diffuse X-ray emission was thermal but there was no convincing evidence for diffuse X-ray emission at energies above 2 keV in the halo. Based on Chandra data, it was finally showed that there is no statistically significant variation in the spectral properties of the diffuse X-ray emission in the northern halo, over scales of several parsecs to several thousand parsecs (~ 400 pc to ~ 3 kpc).

X-rays can penetrate the dense cores of nearby galaxies and are crucial for probing the possible links between starburst and AGN activity. The analysis of Chandra data by Weaver et al. (2002) suggests the presence of a significant source of photoionisation at the centre of NGC 253. This result complements the discovery of resolved (FWHM ~ 200 km s^{-1}) radio recombination line emission at the same location by Mohan et al. (2002).

Weaver et al. (2002) concluded that at the centre of the NGC 253's torus, along with an evolved circumnuclear starburst, is a source of hard X-rays with an unabsorbed 2 keV to 10 keV luminosity of $\geq 10^{39}$ erg s^{-1} and suggested that the ionising source of these X-rays is an intermediate-mass black hole (IMBH) or weakly accreting supermassive black hole.

Weaver et al. (2002) came to this conclusion by estimating that the inverse-Compton process makes roughly only a minor contribution to the hard X-ray emission and postulates that the nuclear starburst in NGC 253 is approximately 20 to 30 million years old (Engelbracht et al., 1998), which implies that its hard X-ray emission is dominated by X-ray bursts (XRBs) (Van Bever and Vanbeveren, 2000). Only a handful of bright XRBs would be required to produce the observed 2 keV $-$ 10 keV luminosity of 2×10^{39} erg s^{-1} (Grimm et al., 2002). On the other hand, the equivalent widths of the emission lines are tens to hundreds of times larger than those of Galactic XRBs (Asai et al., 2000). Weaver et al. (2002) suggested that if several bright XRBs are the source of the continuum photons, they must be located behind a significant amount of absorbing material that suppresses the photoionising continuum. Given the location of the ultra-luminous source coincident with the radio core of NGC 253,

chances are high that the absorbing material is an intermediate-mass, accreting black hole.

Gamma-Ray Observations

Studies of the dense molecular gas in NGC 253 indicate high average densities of $n_{\mathrm{H_2}} \leq 10^6$ cm^{-3} in NGC 253 (Paglione et al., 1997). Therefore, NGC 253 is expected to be one of the brightest starburst galaxies in the gamma-ray domain.

Low-energy gamma-ray observations were made by the OSSE instrument on board the CGRO and detected NGC 253 at sub-MeV gamma-ray levels (Bhattacharya et al., 1994) over an observation period of $\sim 10^6$ s. Bhattacharya et al. (1994) detected NGC 253 continuum emission from 50 keV to 165 keV with a total significance of 4.4 σ, a flux of 3×10^{-11} erg cm^{-2} s^{-1} and an estimated luminosity of 3×10^{40} erg s^{-1}. Bhattacharya et al. (1994) suggested that the source of this low-energy emission is inverse-Compton scattering, Bremsstrahlung and discrete source emission.

EGRET observations of NGC 253 (Sreekumar et al., 1994), on board the CGRO, resulted in an upper limit on the integral flux above 100 MeV of 1.0 $\times 10^{-7}$ photons cm^{-2} s^{-1}. A reanalysis of this data by Paglione et al. (1996) yielded a consistent limit of 8×10^{-8} photons cm^{-2} s^{-1}. More complete EGRET data led Blom et al. (1999) to revise this upper limit down to 3.4×10^{-8} photons cm^{-2} s^{-1}. Blom et al. (1999) found no gamma-ray emission from NGC 253 and derived a 2 σ upper limit to the gamma-ray emission above 100 MeV. Similar upper limits for NGC 253 were obtained in a recent reanalysis of the EGRET data by Cillis et al. (2005). According to Pohl (1994), even starburst galaxies such as NGC 253 may not be luminous enough in gamma rays to be detected individually by EGRET with the exposure available at the time of analysis by Blom et al. (1999).

Itoh et al. (2002) reported a detection of diffuse TeV gamma-ray emission from NGC 253 at the ~ 11 σ level with a flux of $(7.8 \pm 2.5) \times 10^{-12}$ cm^{-2} s^{-1} at energies > 0.5 TeV, based on ~ 150 hours of observation in 2000 and 2001.

Aharonian et al. (2005b) presented the result of 28 hours of observations

of NGC 253 with the H.E.S.S. detector in 2003. No evidence for very high energy gamma-ray emission from this object was found. From the H.E.S.S. data, Aharonian et al. (2005b) derived upper limits on the flux above 300 GeV of 1.9×10^{-12} photons cm^{-2} s^{-1} for a point-like source and 6.3×10^{-12} photons cm^{-2} s^{-1} for a source of radius 0.5° both at a confidence level of 99 %. These upper limits were inconsistent with the spectrum reported by Itoh et al. (2002). The mean zenith angle of observations was 14° and the energy threshold for this dataset was 190 GeV. According to Aharonian et al. (2005b), the non-detection of this object could not be attributed to mispointing of the instrument and given the strong signal from NGC 253 reported by Itoh et al. (2002), the non-detection of this object with H.E.S.S. was surprising.

Itoh et al. (2007) published an erratum to their previous papers, Itoh et al. (2002) and Itoh et al. (2003a). The significance of 11 σ was lowered to less than 4 σ after assessing treatment of malfunction of its photomultiplier tubes. They re-observed NGC 253 in October 2004 with the CANGAROO-III array but failed to detect TeV emission. The upper limit on the gamma-ray flux was 5.8 % Crab at 0.58 TeV for point-source assumption. The total observation time using CANGAROO-III was 1179 minutes (19.65 hours) and 753 minutes (12.55 hours), for ON and OFF observations, respectively. The upper limits of Itoh et al. (2007) were marginally inconsistent with their previous CANGAROO-II observations (Itoh et al., 2002). Following this, Itoh et al. (2007) further investigated their previous CANGAROO-II analysis and found an improper procedure in their hot channel rejection algorithm. After removing that procedure, the previous CANGAROO-II flux was reduced to less than half. Itoh et al. (2007) concluded that they could not claim any evidence for gamma-ray emission from NGC 253.

4.5.7 History and Source Overview: IC 342

IC 342 is a late-type spiral galaxy and is located at a distance of $\sim$ 2 Mpc, though derived distances have varied between 1.8 Mpc and 8.0 Mpc (McCall,

1989; Krismer et al., 1995; Saha et al., 2002; Kubota et al., 2001; Tarchi et al., 2002; Buta and McCall, 1999). This discrepancy arises because IC 342 is located close to the galactic disk, its light is dimmed by the Milky Way's intervening clouds, and such a discrepancy in derived distances to IC 342 should be kept in mind when discussing distance-dependent quantities. IC 342 is part of the Maffei Group which is one of the closest groups to our Galaxy and is located at a galactic longitude of 138° and latitude 10°. The spiral arms of IC 342 are well developed and are seen almost face-on, inclination, $i = 25° \pm 3°$ (Newton, 1980; Sage and Solomon, 1991).

X-Ray Observations

Fabbiano and Trinchieri (1987) observed IC 342 with the Einstein X-ray Observatory (Giacconi et al., 1979) in 1980 and paid particular attention to the central nuclear region of IC 342. Fabbiano and Trinchieri (1987) revealed that X-ray emission is associated with the starburst nucleus of IC 342 and in comparing this emission with previously studied starburst nuclei, found that an overall similarity is shown in their radio through X-ray energy spectra. It was found that the detected X-ray luminosity of the nuclear region of IC 342, $L = 2.7 \times 10^{39}$ erg s^{-1}, is in excess of that predicted, $L \lesssim 10^{39}$ erg s^{-1}, from its infrared luminosity on the basis of stellar and supernova remnant contributions. This excess luminosity was postulated to originate from evolved bright binary X-ray sources located in the nuclear region or a soft gaseous component projected onto the nucleus in a face-on galaxy and would be virtually indistinguishable from the background nuclear emission using the Einstein instruments. Fabbiano and Trinchieri (1987) observed five X-ray point sources within the central region and assumed a distance of 4.6 Mpc for IC 342.

Bregman et al. (1993) obtained X-ray observations of IC 342 with the Röntgensatellit High Resolution Imager (ROSAT HRI) (Trümper, 1984) during February 13$^{\text{th}}$ to 16$^{\text{th}}$, with a total livetime of 19,055 s and found both diffuse and point source X-ray emission from the central region with a luminosity of 1.5 $\times 10^{39}$ erg s^{-1}, assuming a distance of 4.5 Mpc. The image centre, which was

very close to that of the centre of IC 342, revealed 10 easily identifiable sources including one at the centre and two other sources within 1' of the centre of IC 342. Five X-ray point sources seen by Fabbiano and Trinchieri (1987) from an observation with the Einstein X-ray Observatory all lie in the field of view of the ROSAT HRI observation and the first four sources discussed by Fabbiano and Trinchieri (1987) were detected by Bregman et al. (1993). The diffuse emission from the central region had a diameter of 400 pc, a hot gas density of 0.2 cm^{-3} and pressure of $\sim 10^6$ K cm^{-3}. The X-ray size and shape, according to Bregman et al. (1993), was similar to that seen at 1.4 GHz but was unlike the prominent molecular bar. Fabbiano and Trinchieri (1987) argued that the detected emission from IC 342 is consistent with starburst activity whilst Bregman et al. (1993) concluded that the hot gas bubble has an age of 2×10^5 yr and is still confined to the disk, suggesting that IC 342 is a starburst galaxy early in its development.

IC 342 was observed by Kong (2003) with the European Photon Imaging Camera (EPIC) and the Optical Monitor (OM) on board XMM-Newton on 11^{th} February 2001 for about 10 ks. The count rates reported were the count rates in the 0.2 keV $-$ 12 keV band, recorded using the pn-CCD camera, one of three CCD cameras comprising EPIC. Thirty-seven X-ray point sources were detected by Kong (2003) down to a luminosity limit of $\sim 1.3 \times 10^{37}$ erg s^{-1} at a significance of 5 σ or greater. Of the 37 sources, 9 of them were detected in a previous ROSAT HRI observation (Bregman et al., 1993). Most of the sources were located near the spiral arms of the galaxy which would indicate that the X-ray point sources are dominated by young stellar population, presumably high-mass X-ray binaries, with continuous star-forming activity. The X-ray point-source luminosity function was consistent with a power-law shape with a slope of 0.55, typical of starburst galaxies. Kong (2003) also presented the energy spectra of several ultraluminous X-ray sources (ULXs), including the luminous X-ray source in the galactic nucleus. Except for the nucleus and a luminous supersoft X-ray source, other ULXs can generally be fitted with a

simple power-law spectral model. The nucleus was found to be very luminous ($\sim 10^{40}$ erg s^{-1} in 0.2 keV $-$ 12 keV) and required disc blackbody and power-law components to describe the X-ray emission. The spectral fit revealed a cool accretion disc ($kT = 0.11$ keV). Kong (2003) suggested that the source harbours either an intermediate-mass black hole or a stellar-mass black hole with outflow but later ruled out the possibility of an accreting stellar-mass black hole with beamed relativistic jet emission. The proximity of IC 342 and its almost face-on orientation towards the observer provides for unique possibilities to study X-ray point-source populations. Unfortunately, IC 342 is located at low galactic latitude, resulting in a relatively high hydrogen column density, $N_H = 3 \times 10^{21}$ cm^2 (Dickey and Lockman, 1990). This limited Kong (2003) to constrain local absorption and X-ray emission below 1 keV. A distance of 1.8 Mpc (Buta and McCall, 1999), where 1" corresponded to 8.7 pc, was employed for the XMM-Newton data.

Mak et al. (2008) observed IC 342 on April 2$^{\text{nd}}$ 2006 starting at 15:15:44 (UT) with the Chandra High Resolution Camera (HRC-I) for a total exposure time of 12.16 ks, with a photon energy range of 0.08 keV $-$ 10 keV and resolved a previously historical ULX near the nucleus into two sources. Mak et al. (2008) suggested that the closer of these sources to the nucleus is not an ULX but must be associated with the nucleus itself and found that the observed X-ray luminosity of this closer source is very close to the predicted X-ray emission from a starburst, suggesting that the nuclear X-ray emission of IC 342 is dominated by a starburst.

Although X-ray observations of IC 342 with the Einstein X-ray Observatory (Fabbiano and Trinchieri, 1987), ROSAT HRI (Bregman et al., 1993), and ASCA (Okada et al., 1998; Kubota et al., 2001) have indicated that the majority of the X-ray emission comes from a few ULXs, infrared and radio observations have indicated moderately strong nuclear starburst activities (Becklin et al., 1980) in IC 342. Optical and near IR observations of the inner region of IC 342 have revealed the presence of a nuclear star cluster (Rickard and Harvey, 1984).

IC 342 possesses a young luminous nuclear star cluster which has a mass of 6×10^6 $M_\odot$ and formed in a short-lived but major burst about 60 Myr ago (Böker et al., 1997, 1999) though Feng and Kaaret (2008) suggests that the minimum stellar age is between 10 Myr and 20 Myr. Mak et al. (2008) found that both the X-ray and the optical emission are confined to a region of radius $\sim$ 100 pc in the centre of IC 342. The diffuse X-ray emission in IC 342 extends preferentially along the north-south direction, which is the same as the alignment of the star clusters in the optical range. This implies that the nuclear X-ray emission is associated with star formation, and the Chandra observations suggest that most of the star formation occurs in the central ring region rather than along the spiral arms. No sign of the 6.4 keV Fe Kα line emission was found by Mak et al. (2008), typically an indicator of AGN, in the XMM-Newton EPIC spectrum (Bauer et al., 2003; Kong, 2003). However, this line is also absent in a number of starburst galaxies identified as having hidden AGN (Tzanavaris and Georgantopoulos, 2007) and the possibility cannot be excluded that IC 342 harbours an AGN. The positional coincidence of the X-ray centre with the optical star clusters in IC 342 could suggest a scenario of coexistence of the nuclear star cluster and an AGN, as discussed by other authors (Seth et al., 2008; Shields et al., 2008). The triggering mechanism for both starburst and AGN phenomena could be the interaction or the merging of gas-rich galaxies, which generates fast compression of the available gas in the inner galactic regions, causing both the onset of a major starburst and the fuelling of a central black hole (Mak et al., 2008), hence raising an AGN connection.

Indeed, any activity found in a galactic nucleus be it due to massive star formation, an accreting super-massive black hole or a combination of both requires the inflow of gas into the central few parsecs of the galaxy, and Schinnerer et al. (2008) presented strong evidence that mechanical feedback of nuclear star formation onto the disk gas flow in an extragalactic nucleus had been found in IC 342. The gas flow model by Schinnerer et al. (2008) in IC 342, depicted in Figure 4.6, proposes that a large-scale stellar bar moves gas towards the centre of the

galaxy via two spiral arms. The stellar winds and supernova shocks released by the most recent nuclear star formation event have significantly altered the path of the molecular gas towards the centre on the last few tens of parsecs, thus currently preventing efficient fuelling of the nucleus implying mechanical feedback. As the large-scale stellar bar continues to move gas towards the centre, it is likely that the gas resumes its old path once the mechanical energy has been dispersed. It is presumed that the nucleus will then again collect molecular gas until the next star formation episode. This feedback between nuclear activity and fuelling efficiency appears to self-regulate the rate of nuclear star formation and offers a natural explanation for the repetitive star formation found in nuclear star clusters (Rossa et al., 2006; Walcher et al., 2006). If correct, this scenario implies that models for the gas fuelling mechanism (over the innermost 1 pc − 100 pc) cannot rely on the shape of the gravitational potential alone but also need to take into account the effect of mechanical energy released by nuclear activity onto the gas flow. The impact of this feedback process would be strongly variable with time and would critically depend on the amount of energy released as well as its geometry. In a broader sense, the model proposed by Schinnerer et al. (2008) also has implications for the evolution of any central massive object, whether it is a stellar cluster or a black hole, that requires occasional fuelling. Nuclear activity appears to have the potential to significantly reduce or even temporarily shut off fuelling, thus self-regulating the growth of the central mass of the galaxy. The altered path of the molecular gas towards the galactic centre of IC 342 had previously been identified and at that time Schinnerer et al. (2003) concluded that the non-circular motions observed in the CO kinematics of the gas disc were most likely due to streaming motions. Possible cause for such streaming motions could be the large-scale stellar bar. These models, together with the high-density medium that characterises the central regions of starburst galaxies and its power to accelerate particles up to relativistic energies, make starburst galaxies good candidates as gamma-ray sources.

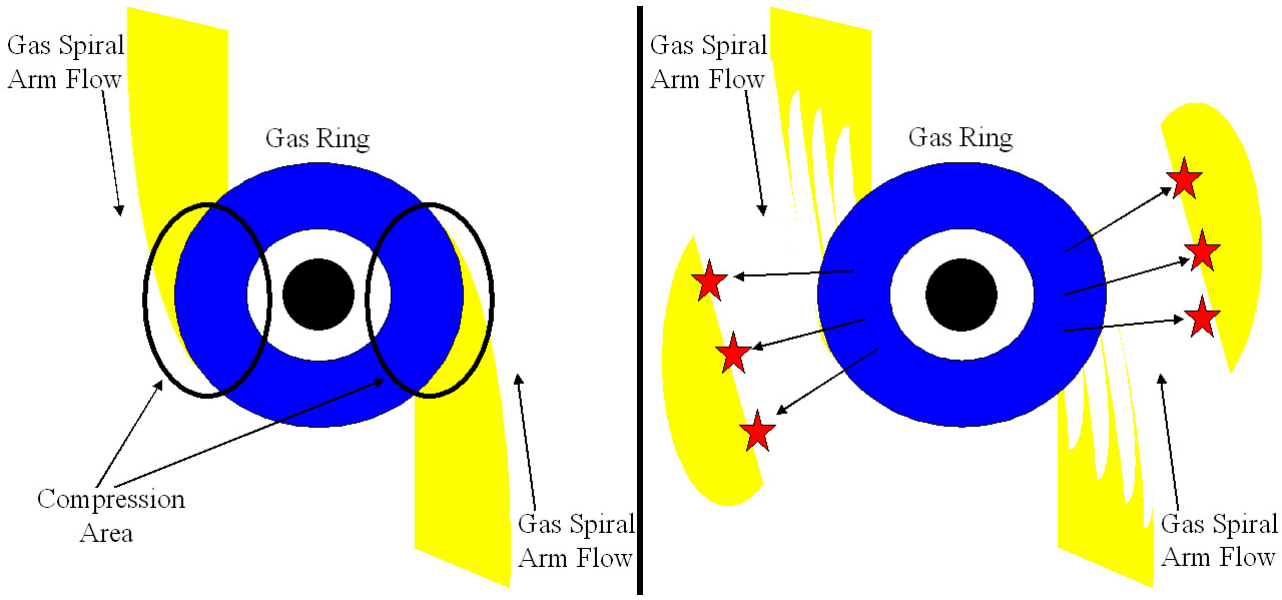

Figure 4.6: Illustration of a model for the self-regulation of the fuelling of the nuclear stellar cluster in IC 342. In the absence of massive star formation the molecular gas moves towards the nucleus along the gas lanes due to the gravitational influence of a large-scale stellar bar (left panel). The mechanical energy released by stellar winds and supernovae of a recent massive star formation in the nucleus is sufficient to alter the flow of the molecular gas thus significantly reducing the fuel available for future star formation events (right panel). After the stellar winds and supernova explosions have ceased, it is expected that the force of the gravitational bar potential takes over again and the gas flow will be similar to the situation shown in the left panel (Schinnerer et al., 2008).

Mak et al. (2008) also drew attention to a large uncertainty in the distance estimate to IC 342 due to the large uncertainty in the amount of dust extinction toward the galactic centre along that line of sight. Distance estimates of IC 342 range from 1.5 Mpc to 8 Mpc (Buta and McCall, 1999). A distance of 1.8 Mpc was assumed by Mak et al. (2008) (corresponding to a scale of 10" = 87 pc), identical to that in Böker et al. (1997), Böker et al. (1999) and Kong (2003), and similar to that (2 Mpc) assumed by Meier and Turner (2005). Mak et al. (2008) could not directly compare luminosities from the works of different authors because of the different assumptions made in those works. For example, the luminosity values in the earlier ROSAT HRI and ASCA publications were computed assuming distances to IC 342 of 4.5 Mpc and 4 Mpc respectively.

Chapter 5

Methodology and Analysis

5.1 Introduction

In the detection of TeV gamma rays, the first step in analysis is the selection of data from the database. There is a vast amount of data recorded by the Whipple 10-metre telescope and not all of the events originate from gamma rays. In fact, the gamma-ray events recorded by the telescope are vastly outnumbered by events from non-gamma-ray sources such as cosmic-ray showers, single-muon events and sky-noise fluctuations. Although all of these can give rise to somewhat similar events, the key is to record as much information as possible and then devise a rejection procedure for the unwanted non-gamma-ray-initiated EASs.

When selecting a database of recorded events for analysis, a number of factors must be taken into consideration. Factors such as sky condition, status of the telescope during recording of data and the elevation angle of the telescope can each independently have a serious effect on the quality of data recorded by the telescope. Adverse weather conditions such as cloud cover and water vapour in the atmosphere can effect the intensity of the image and signals recorded. Hardware degradation of the electronics can cause the telescope to record perfect in-focus cascades with lower sensitivity. When recording at low elevation, the Cherenkov photons must traverse a greater distance through the atmosphere before they reach the telescope, resulting in fainter images. On the other hand, when recording at low elevation, the light cone of the EAS spreads out more

resulting in a much larger light pool at ground level compared to a smaller light pool generated by an EAS arriving from zenith, resulting in a larger collection area. Due to all of these criteria, the selection of data for analysis requires much consideration.

For this work, only data recorded in good weather and atmospheric conditions and without hardware malfunctions, were used in the analysis of IC 342. The Whipple 10-metre telescope is located at latitude = $31^\circ\ 40^\mathrm{m}\ 49.7^\mathrm{s}$ and longitude = $-110^\circ\ 52^\mathrm{m}\ 45.1^\mathrm{s}$. IC 342 lies at right ascension = $3^\mathrm{h}\ 46^\mathrm{m}\ 49.10^\mathrm{s}$ and declination = $+68^\circ\ 05'\ 47.4''$. Due to the celestial position of IC 342, all data were recorded at angles between 41° and 54° elevation.

5.2 Data Preparation

The raw data recorded by the telescope are subjected to cleaning and calibration processes before analysis in order to maximise the true Cherenkov light content of EAS images whilst simultaneously minimising the effects of background sky-noise fluctuations. This section describes the preparation of the data for analysis.

5.2.1 Software Padding

During ON/OFF observing, differing sky brightness between ON and OFF sky regions can introduce a bias. A software noise equalisation technique known as "noise padding" is employed to correct for this bias by injecting software noise into the events for the darker sky region to compensate for this bias (Cawley et al., 1990). In an ON/OFF data set where P_{ON}/P_{OFF}, σ_{ON}/σ_{OFF} and C_{ON}/C_{OFF} are the ON/OFF pedestal, pedestal variance and the component due to the Cherenkov signal respectively for a particular pixel, the total ON signal is given by:

$$ON = P_{ON} + R_G\sigma_{ON} + C_{ON} + R_G\sqrt{C_{ON}} \tag{5.1}$$

where R_G represents a random number drawn from a Gaussian distribution of zero mean and unit variance (Quinn, 1997). The noise component due to the night-sky-background fluctuations in the ON region is:

$$N_{ON} = R_G \sigma_{ON} \tag{5.2}$$

Similarly, for the OFF region:

$$N_{OFF} = R_G \sigma_{OFF} \tag{5.3}$$

Suppose we are working with pairs of data sets where N_{ON} is larger than N_{OFF} then we wish to inject additional noise, N_{ADD}, in the OFF events such that:

$$N_{ON}^2 = N_{OFF}^2 + N_{ADD}^2 \tag{5.4}$$

The total OFF signal is then:

$$OFF = P_{OFF} + R_G \sigma_{OFF} + R_G N_{ADD} + C_{OFF} + R_G \sqrt{C_{OFF}} \tag{5.5}$$

In a situation where the OFF region is brighter than the ON region N_{ADD} is added to the ON pixels instead. In this way the noise levels can be approximately equalised between the ON and OFF data sets.

5.2.2 Pedestal Subtraction

The pedestal is a small positive offset value applied to each ADC channel to allow for both negative and positive night-sky noise fluctuations. The pedestals and the night-sky background are calculated using noise events, which are artificially triggered snapshots of the sky, recorded at a rate of 1 Hz. Pedestal

subtraction is not only a data preparation process but is also used as a calibration tool for the telescope itself which was explained in Section 3.3.1. For a recorded Cherenkov event, the average pedestal value in each ADC channel is subtracted from the signal recorded from that channel to derive the signal due the Cherenkov light. The pedestal variance is the spread of artificially triggered ADC values in each channel and gives an indication of the night-sky background fluctuations for that channel. If the pedestal variance is found to be too large (> 1.5 times the mean pedestal variance), then it is assumed that the PMT had a star or bright region of the sky in its field of view during the observation run. Such channels are suppressed in the analysis so that they do not influence the outcome of the analysis result. Similarly, if the pedestal variance of a channel is too low (< 0.6 times pedestal variance), the PMT may have been switched off or not functioning properly.

5.2.3 Image Cleaning

Each event recorded by the camera is made up of signals from the PMTs. Some of the PMT signals will contain genuine Cherenkov signals plus background noise while others will contain only background night-sky noise. To remove the unwanted background signals from the overall image, a filtering technique known as picture/boundary cleaning is used. With this technique a PMT signal is set to zero (i.e., rejected from the overall image) unless it has a signal greater than a certain threshold (defined as the "picture" threshold) or is a neighbour of such a PMT and has a signal greater than some lower threshold (defined as the "boundary" threshold). For each PMT, these thresholds are specified in terms of the standard deviation (s.d.) of the pedestal value for that PMT (see Sections 3.3.1 and 5.2.2). The optimised values for the picture and boundary thresholds were found to be 4.25 s.d. and 2.25 s.d. respectively. An example of the application of picture/boundary cleaning is shown in Figure 5.1. The top image of Figure 5.1 shows a Cherenkov event recorded along with background noise. The bottom image of Figure 5.1 shows the same event after the image cleaning

has been applied. The success of this process can be seen as the unwanted background noise artifacts have removed leaving only a clean Cherenkov image.

5.2.4 Gain Normalisation

After each ADC channel has had its pedestal subtracted and the Cherenkov events have been cleaned, each surviving channel is adjusted to compensate for differences in PMT gains. This adjustment is called gain normalisation. Since each PMT has a slightly different gain, it is necessary to scale the signals recorded in each PMT accordingly so PMTs with larger gains do not distort the final analysed image. This is achieved using a nitrogen lamp located at the centre of the telescope dish. At the beginning of night's observing, the nitrogen lamp is pulsed at $\sim$ 750 Hz for one minute, providing uniform illumination across the camera - this is a "nitrogen run". The artificial events triggered in this way are used to calculate the gain of each PMT relative to the average gain. This process is also a telescope calibration tool (see Section 3.3.2). The processes of pedestal subtraction and gain normalisation are collectively known as "flat-fielding".

5.3 Image Parameterisation

After the image-cleaning and gain-normalisation processes, each image is parameterised. The shape and orientation of each image recorded by the imaging atmospheric Cherenkov telescope is dependent on the particle which caused the cascade (see Figure 5.3). A parameter-fitting procedure was proposed by Hillas (1985) to quantify the shape and orientation of the recorded images. The parameter ranges are expected to differ between gamma-ray, cosmic-ray and muon images. The definition of the original six Hillas parameters (denoted †), together with additional parameters introduced to increase gamma-ray selection efficiency, can be seen in Table 5.1 and Figure 5.2. The calculation of the parameter values from the PMT signals is shown in Appendix A. With this technique, the first significant detection of the Crab Nebula at TeV energies

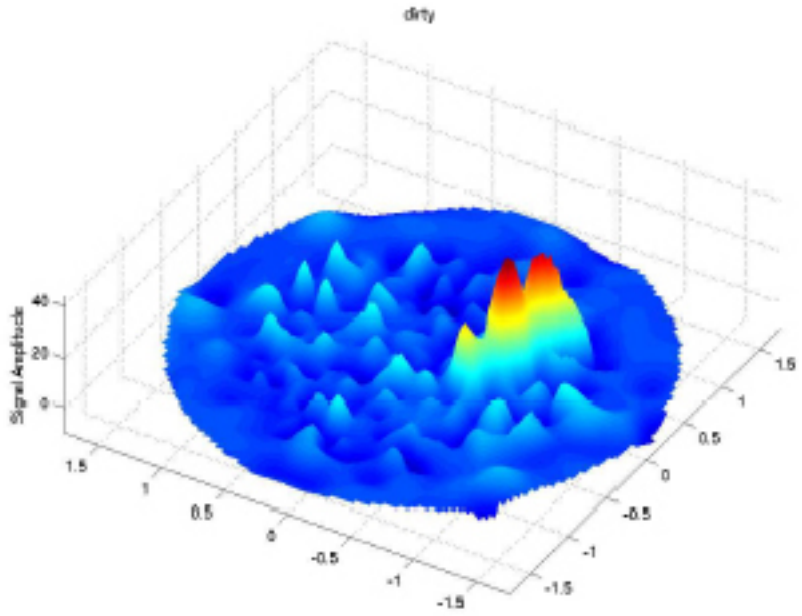

Before picture/boundary cleaning.

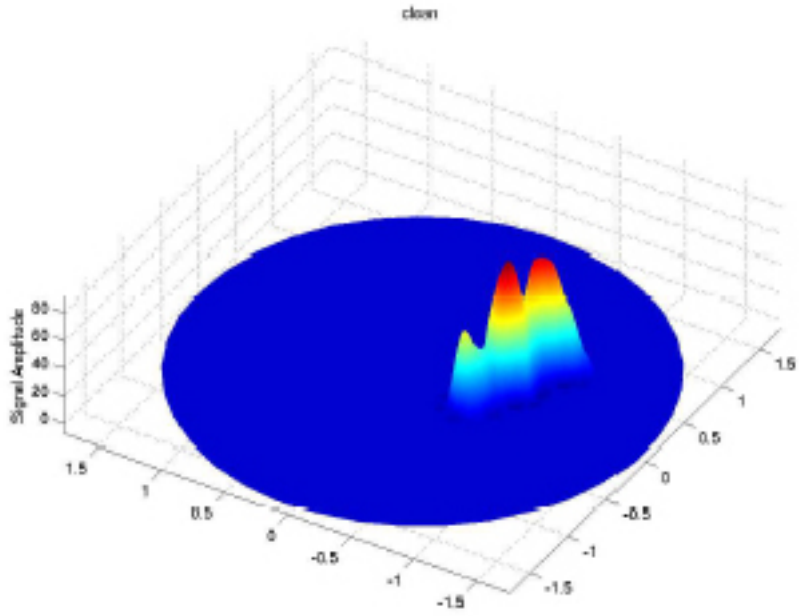

After picture/boundary cleaning.

Figure 5.1: A typical event recorded by the Whipple 10m telescope before and after picture/boundary cleaning is applied. The picture on top shows the event before cleaning and the picture on the bottom shows the event after cleaning, clearly indicating its success in removing unwanted noise. Adapted from Gammell (2004).

was made (Weekes et al., 1989). The parameters used in this work are length, width, distance, length/size, frac3 and alpha.

5.4 Gamma-Ray Event Selection

The original parameters and parameter ranges proposed by Hillas (1985) were extended to provide a new set of parameter criteria called "Supercuts". The parameter ranges for Supercuts were derived experimentally from Crab Nebula data (Punch, 1991) whereas the original ranges were determined using computer simulations (Hillas, 1985).

5.4.1 Supercuts

The Supercuts technique is now a standard process applied to data recorded by the Whipple 10m telescope to discriminate between gamma-ray events and cosmic-ray events. Events which lie within the parameter boundaries are considered gamma rays and are retained. Events which lie outside the parameter boundaries are considered to be cosmic rays or night-sky background and are rejected. The initial cuts employed in this work were a set of cuts known as Supercuts 2000, developed on the basis of Crab Nebula observations during the $1999 - 2000$ observing season. The efficiency of Supercuts 2000 was shown to be greatly enhanced by the application of a *length/size* cut, which was designed to reject background images caused primarily by local muons. Supercuts 2000 represent the standard parameter cuts applied to the recorded data. Table 5.2 shows the parameter cuts imposed by Supercuts 2000. As described later in this chapter, the values of the cuts were then re-optimised specifically for the $2003 - 2004$ observing season.

Supercuts 2000 serves to eliminate background events due to cosmic rays and local muons. In this work it was found that Supercuts 2000 eliminated 99.4 % of background events. When the telescope is pointed towards a potential gamma-ray source, any gamma-ray images recorded will tend to point towards the centre of the field of view of the camera, as these gamma rays are coming

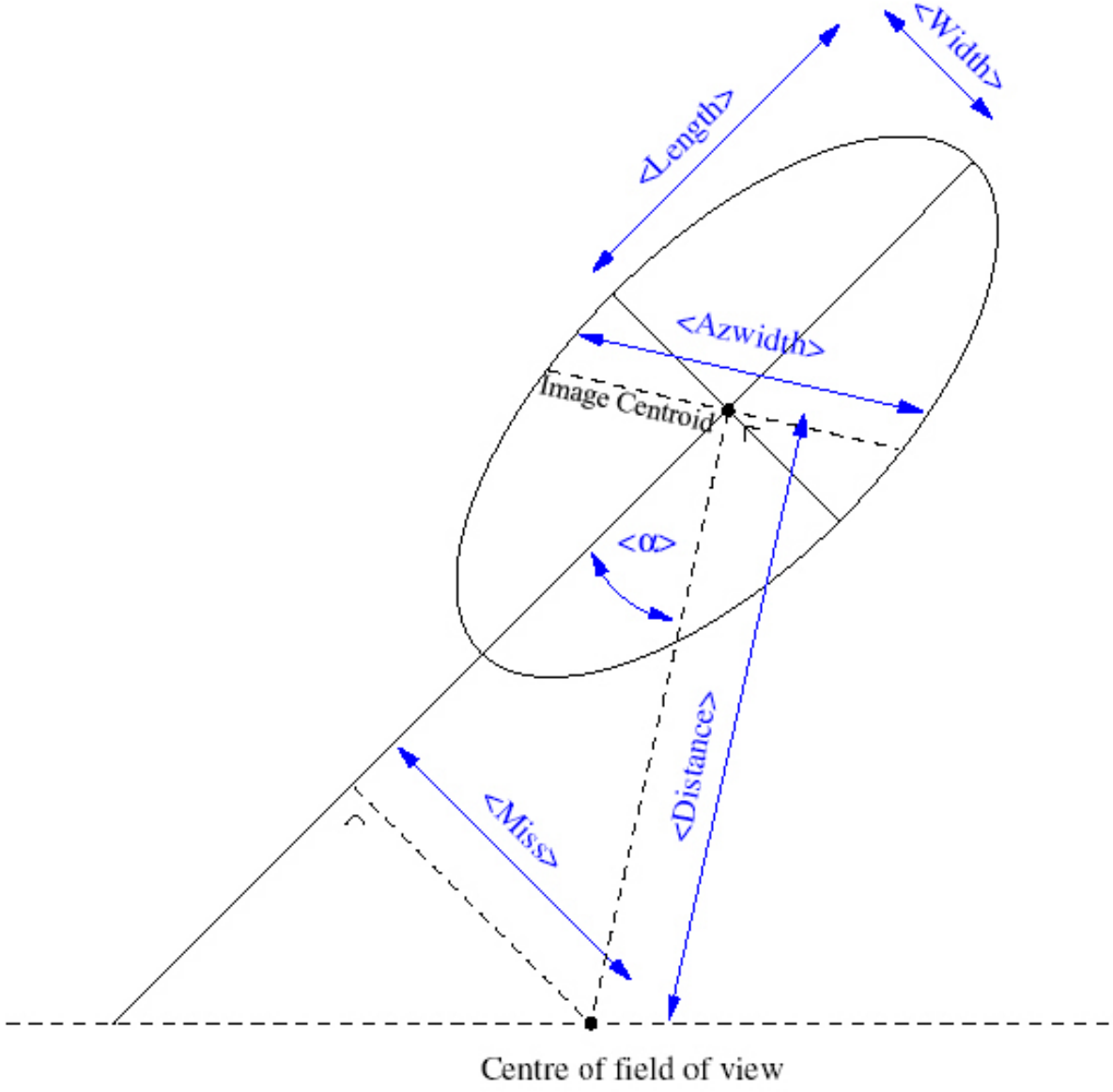

Figure 5.2: Geometrical definition of Hillas parameters, from Dunlea (2001).

Length * †	The root-mean-squared (RMS) spread of light along the major axis of the image (the longitudinal development of the shower). It is a measure of the shape of the image.
Width * †	The RMS spread of light along the minor axis of the image (the lateral development of the shower). It is a measure of the shape of the image.
Size	The sum of the number of digital counts in all PMTs which are part of the image, corresponding to the total light content of the image (i.e., the luminosity). The size of the image is related to the energy of the event-triggering particle.
Length/Size *	A measure of the compactness of the image in relation to its total light content. Used to eliminate background due to local muons.
Max1, Max2, Max3	The number of digital counts in the highest, second highest and third highest PMTs in the image. By requiring that these three PMTs are above some preset threshold, images due to sky noise fluctuations can be eliminated.
Frac3 * †	The fraction of total light of the image contained in the three highest PMTs. This is used to eliminate events caused by sky noise or by particles physically passing through the camera.
Asymmetry	A measure of how asymmetric the image is. Gamma-ray images should be tear-drop shaped, with their light distributions skewed toward their source position (see Figure 5.3).
Azwidth †	The RMS spread of light perpendicular to the line connecting the centroid of the image with the centre of the field of view of the camera. It describes the shape and orientation of the image.
Distance * †	The distance from the centroid of the image to the centre of the field of view of the camera. It gives information on the impact parameter of the particle shower with respect to the telescope, i.e., the distance from the telescope to the intersection of the shower axis with the ground.
Miss †	The perpendicular distance between the major axis of the image and the centre of the field of view of the camera. It is a measure of the orientation of the shower image.
Alpha *	The angle between the major axis of the image and a line drawn from the centroid of the image to the centre of the field of view of the camera. It is a measure of the orientation of the image and is related to the angle between the axis of the EAS and the axis of the telescope.

Table 5.1: Parameters relating to the shape and size of an IACT image. † denotes the original six Hillas parameters. * denotes the parameters used in this work.

Parameter	Lower Limit	Upper Limit
Length	0.13°	0.25°
Width	0.05°	0.12°
Length/Size	–	0.0004°/d.c.
Distance	0.4°	1.0°
Max1	30 d.c.	–
Max2	30 d.c.	–
Frac3	–	0.98
Alpha	–	15°

Table 5.2: Supercuts 2000 (d.c., where 1.0 d.c. $\approx$ 1.0 photoelectron).

from a point source directed to the centre of the camera. Cherenkov light retains the original direction of the incident photon. Cosmic rays are randomly oriented so the recorded images will generally not point towards the centre of field of view of the camera. The distance and alpha parameters are employed to distinguish and reject events of this nature. Figure 5.3 illustrates this point from a standard observational scenario. Due to perspective, images of individual EASs appear elongated unless seen head-on. Those originating from a common point (A, B and C in Figure 5.3) reveal a distinct source of gamma rays. Those with random orientation (D and E in Figure 5.3) presumably stem from the cosmic-ray background.

Gamma-ray images tend to have smaller lengths and widths than cosmic-ray images due to the smaller dimensions of the extensive air showers initiated by gamma rays. Gamma-ray EASs start higher up in the atmosphere and spread out less; as a result images of gamma-ray events are geometrically shorter and thinner than images of cosmic-ray events.

The amount of Cherenkov light radiated is proportional to the total number of particles in an EAS and so is a good estimator of the initial energy of the incident photon. The "size" parameter for an EAS image is the total number of digital counts summed over all pixels in the image and is therefore a measure of the Cherenkov light from the shower. Thus, the "size" of an image is related to the energy of the initiating particle.

Images due to single muons (from hadronic showers) radiating close to the

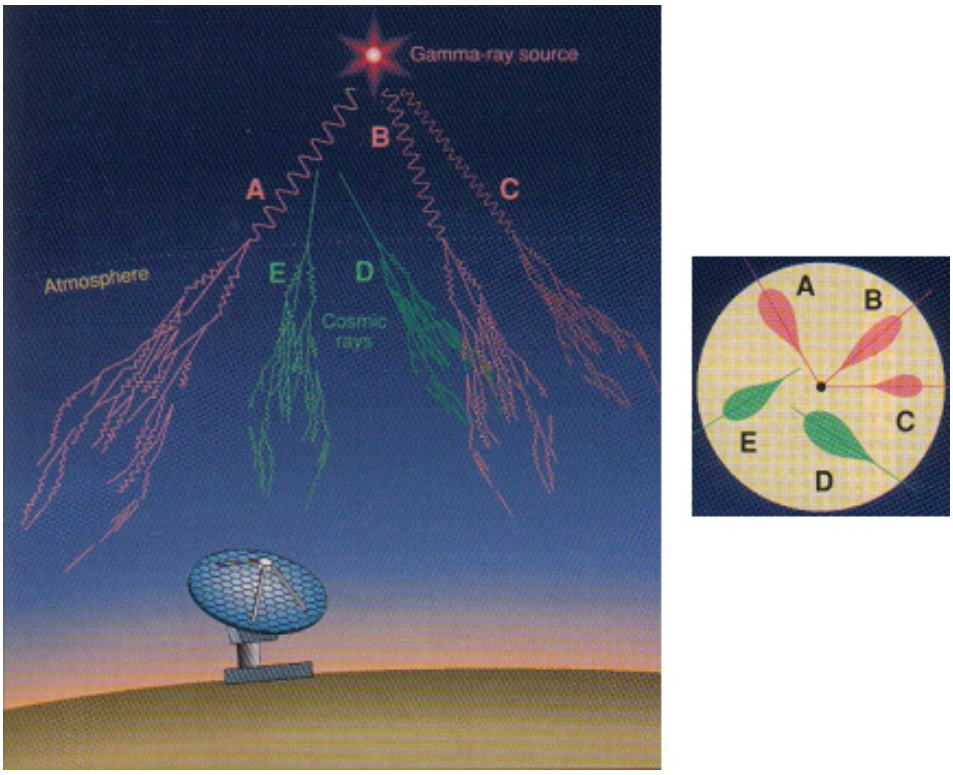

Figure 5.3: The figure on the left illustrates a standard observational scenario. The figure on the right illustrates the imaging telescope's point of view of the scenario illustrated on the left. Image by Diaz (1995).

telescope tend to have large lengths but small sizes, and hence the parameter length/size can be used to discriminate between gamma rays and muons. Muons with small impact parameters form ring-shaped images (or parts of rings) due to the nature of Cherenkov emission. An ellipse fitted to such an image would be very large and the Cherenkov light emitted by a single particle is not particularly intense, so muons are expected to have relatively large values of length/size. However, for muons with large impact parameters the ring structure is only partially imaged. Such compact muon arcs are very similar to gamma-ray images, and are difficult to discriminate using a single telescope.

5.4.2 Significance

Once the recorded data have been prepared, the images parameterised and the parameter cuts applied, an excess of gamma-ray events may be left if the source under observation was emitting gamma radiation at the time of observation. A

measure of the statistical significance of the gamma-ray signal is given by the ratio of the signal to the error, calculated assuming Poisson fluctuations only in both ON and OFF counts:

$$\sigma_{EXCESS} = \frac{N_{ON} - N_{OFF}}{\sqrt{N_{ON} + N_{OFF}}} \tag{5.6}$$

where N_{ON} and N_{OFF} are the number of events or counts which have passed the selection cuts in the ON run and OFF run datasets, respectively. The significance is an indication of the probability that the signal is real as opposed to random fluctuations in the background cosmic-ray rate. It may be argued that Equation 5.6 ignores the possibility of non-Poissonian errors in the data. However, detailed analysis on a large subset of data has shown that signal fluctuations are close to Poissonian (Reynolds et al., 1993).

The corresponding gamma-ray rate, r, and the uncertainty associated with it, Δr, are calculated from:

$$r \pm \Delta r = \frac{N_{ON} - N_{OFF}}{t} \pm \frac{\sqrt{N_{ON} + N_{OFF}}}{t} \tag{5.7}$$

where t is the duration of the recorded runs, typically expressed in minutes. From this it can be seen that the significance:

$$\sigma_{EXCESS} = \frac{r}{\Delta r} \tag{5.8}$$

When determining the gamma-ray excess, it is helpful to plot the distribution of the alpha (α) parameter for the events which pass all of the other gamma-ray selection criteria in the ON and OFF runs. If a gamma-ray source is present there should be an excess of events in the ON data with a low α value as gamma-ray event images should be aligned towards the centre of field of view of the camera (subject to statistical fluctuations in the PMT signals). There should be a fairly isotropic distribution of α values in the OFF dataset (see Figure 3.7 as an

example). To show the effect of Supercuts, these criteria were applied to 41 Crab Nebula ON/OFF pairs and 22 Mrk 421 ON/OFF pairs. These runs were all recorded during the same season of observation at reasonably high elevations in good weather conditions, they had stable rates for the full 28 minutes of the run, and they showed no hardware or data-acquisition anomalies. The significance for the 41 Crab Nebula ON/OFF pairs after application of Supercuts was found to be 20.9 σ with a rate of 2.47 ± 0.12 gamma rays per minute. The significance for the 22 Mrk 421 ON/OFF pairs after application of Supercuts was found to be 33.0 σ with a rate of 5.00 ± 0.15 gamma rays per minute.

5.4.3 Optimisation of Supercuts

In this work, the Supercuts criteria were optimised to establish whether any significant improvement in background rejection could be achieved for the recorded datasets in the season of observation. An observing season runs roughly from September to June. The values chosen for Supercuts have traditionally been optimised to give maximum gamma-ray significance on a set of Crab Nebula data recorded during the same observing season as the datasets under analysis.

The main reason for doing this is to take into account changes and modifications to the telescope. Changes in the optimum cut values for alpha, width, distance and length/size can arise from a combination of tracking, focusing, mirror alignment improvements, degradation and system upgrades.

As an example of this procedure, optimisation of the criteria for the 2003/2004 season is described in detail here. A total of 41 Crab ON/OFF pairs, totalling $\sim$ 19.1 hours, were used in the optimisation procedure. These runs were all recorded at reasonably high elevations (between 50° and 80°), in good weather conditions, had stable rates for the full 28 minutes of the run, and showed no hardware or DAQ anomalies.

Each selection cut is initialised to a plausible starting value before optimisation begins. In this work, the starting values were set to the values used in Supercuts 2000. The optimum set of selection criteria is then determined with

Parameter Cut	Supercuts 2000	Optimised Cuts
Alpha	15°	9°
Lower Length	0.13°	0.13°
Upper Length	0.25°	0.25°
Lower Width	0.05°	0.04°
Upper Width	0.12°	0.10°
Lower Distance	0.40°	0.56°
Upper Distance	1.00°	0.96°
Length/Size	0.00040°/d.c.	0.00030°/d.c.
Frac3	0.98	0.98

Table 5.3: Cut values optimised for the 2003 − 2004 observing season, compared with the standard Supercuts 2000 values.

respect to one cut at a time, by fixing all cuts except the one being optimised. This produces gamma-ray significance values for the range of each cut being optimised. The peak in a plot of gamma-ray significance versus cut value for the cut under optimisation represents its first "best-estimate" value. Figure 5.4 shows the gamma-ray significance versus cut value plot for each cut from the final iteration of the optimisation procedure. Once the first best-estimate value for each cut is found, the process is repeated with the first best-estimates values replacing the initial values. After several iterations the best-estimate cuts converge. For the present analysis, the cuts were found to converge sufficiently after three iterations, to give the "optimised" values shown in Table 5.3.

The significance for the 41 Crab Nebula ON/OFF pairs after application of the optimised cuts was found to be 28.0 σ with a rate of 1.34 $\pm$ 0.05 gamma rays per minute, compared with 20.9 σ and 2.47 $\pm$ 0.12 gamma rays per minute for Supercuts 2000. When the optimisation is based solely on the significance, the rate typically diminishes as seen here. The significance improves because of better background rejection (99.94 % for the optimised cuts compared to 99.4 % for Supercuts 2000). While it is shown that the optimised cuts do achieve improvement for the Crab Nebula data, improvement will only be expected in the case of IC 342 if there actually is a gamma-ray signal present and if the IC 342 energy spectrum is similar to that of the Crab Nebula. As discussed in

Section 6.3, the spectral index for IC 342 is likely to be in the region of -2.5, compared with a value of $-2.49 \pm 0.06_{\mathrm{stat}} \pm 0.04_{\mathrm{syst}}$ for the Crab Nebula (Hillas et al., 1998).

The validity of the optimised Supercuts derived from Crab Nebula data, was tested using a selection of independent data from a known TeV gamma-ray source, Mrk 421. The 22 Mrk 421 ON/OFF pairs were recorded in the same season of observation as the data under investigation in this work and again were selected on the basis of high elevation (between 50° and 84°), good weather conditions, stable rates for the full 28 minutes of the run, and absence of hardware and DAQ anomalies. The significance for the 22 Mrk 421 ON/OFF pairs after application of the optimised cuts was found to be 31.7 σ with a rate of 2.14 ± 0.07 gamma rays per minute, compared with 33.0 σ and 5.00 ± 0.15 gamma rays per minute for Supercuts 2000.

The Supercuts optimised for the Crab Nebula data produced a slightly worse result in the case of Mrk 421. This is probably due to a variety of factors, including differences in spectra of the two sources, sky brightness differences and different sets of pixels suppressed (due to bright stars in the field of view) in the two cases.

5.4.4 Scaling of Optimised Supercuts with Elevation

Because of the celestial position of IC 342 and the location of the Whipple Observatory, the elevation of this object never exceeds 54° when observed with the 10m telescope. The IC 342 data used in this work were recorded at low elevation angles, between 41° and 54°.

When observing an object of low elevation, the Cherenkov radiation must traverse a greater distance through the Earth's atmosphere to reach the telescope and will therefore be subject to more absorption. Furthermore, the impact area on the ground of the cascade arriving at a lower angle is far greater than the impact area of a cascade falling straight down from zenith. For observations at low elevation, the energy threshold is higher and the event rate is lower (even

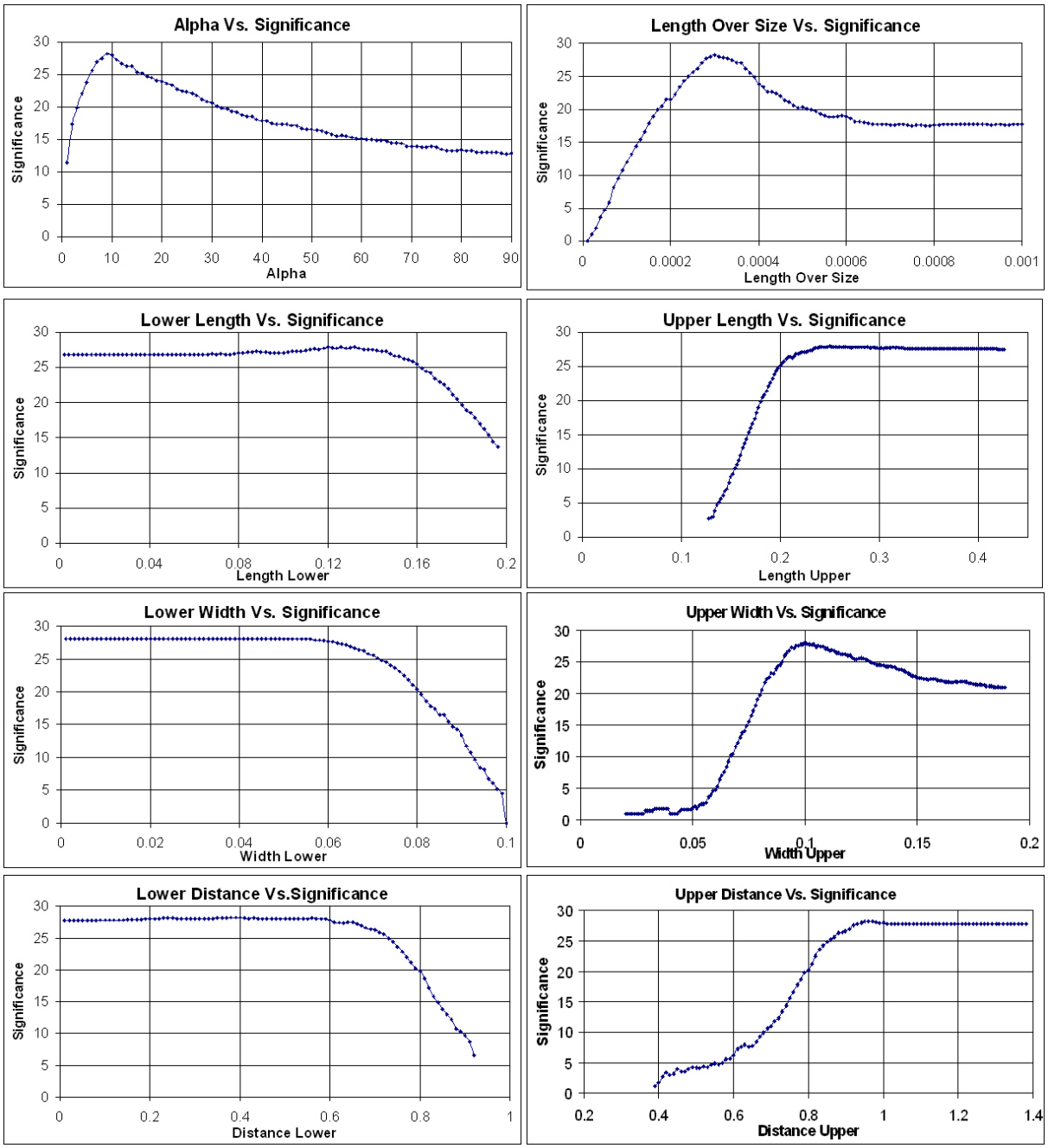

Figure 5.4: Plots of final significance versus cut values for the optimisation procedure described in Section 5.4.3. The position of the peak, if present, in each plot indicates the optimal cut value.

though the effective area is greater for high-energy events). The length, width and size of Cherenkov images are all reduced by the greater distance to the EASs, so the selection criteria derived for high elevation observations are no longer optimised. To overcome this problem, an attempt was made to scale the cuts with respect to elevation.

The Crab Nebula data discussed in Section 5.4.3 were recorded with elevation angles ranging from 50° to 80°. The dataset was split into five separate subsets for elevation ranges: $50° - 55°$, $56° - 62°$, $63° - 67°$, $68° - 74°$ and $\geq 75°$ with 5, 7, 10, 5 and 14 ON/OFF pairs in each subset respectively. Re-optimisation was carried out on each subset as described in the previous section, to achieve the highest significance for each elevation range. Again, it was found that the procedure converged sufficiently for each subset after three iterations.

The purpose of this particular analysis is to compare the data under investigation recorded at low elevation to "standard candle" data recorded at the same low elevation. The derived scaling of optimised Supercuts values for each elevation range is presented in Table 5.4. Table 5.5 shows the comparison of significance and rates between the different elevation ranges for the respective subsets of Crab Nebula data. An extra set of cuts was extrapolated from the subset cuts to provide cuts applicable to elevations less than 50°. No Crab Nebula data were available below the $50° - 55°$ elevation range so this extrapolation was done to allow the lowest IC 342 elevation data recorded (41°) to be compared beyond the lowest Crab Nebula elevation data recorded (50°). These extrapolated cuts are shown in Table 5.6. For observations at low elevation, the air showers detected are further from the telescope and the Cherenkov light traverses a greater thickness of atmosphere to reach the detector. As a result, the recorded events are expected to be less bright and have smaller length and width. This is reflected in the lower value for the upper length cut and the higher length/size cut for the low elevation data (the upper width cut is already comparable with the pixel diameter). Furthermore, because the events on average have smaller length the orientation is less well defined, leading to a

Parameter Cut	$50° - 55°$	$56° - 62°$	$63° - 67°$	$68° - 74°$	$\geq 75°$
Alpha	22°	16°	10°	10°	9°
Lower Length	0.13°	0.14°	0.12°	0.12°	0.11°
Upper Length	0.20°	0.20°	0.24°	0.24°	0.23°
Lower Width	0.05°	0.05°	0.05°	0.04°	0.05°
Upper Width	0.10°	0.10°	0.10°	0.10°	0.11°
Lower Distance	0.40°	0.41°	0.38°	0.50°	0.51°
Upper Distance	0.95°	0.97°	0.98°	0.89°	0.95°
Length/Size	0.00036 d.c.	0.00036 d.c.	0.00033 d.c.	0.00037 d.c.	0.00030 d.c.
Frac3	0.98	0.98	0.98	0.98	0.98

Table 5.4: Cut values derived from the scaling of optimised Supercuts for each elevation range.

higher alpha cut. The significance and rates for all 41 Crab Nebula ON/OFF pairs when analysed with the combination from the scaled cuts from the different elevation ranges was found to be 29.5 σ with a rate of 1.84 ± 0.06 gamma rays per minute.

Elevation Range	Significance (σ)	Rate (gamma rays/minute)
$50° - 55°$	6.1	1.45 ± 0.24
$56° - 62°$	11.2	1.57 ± 0.14
$63° - 67°$	14.7	1.53 ± 0.10
$68° - 74°$	12.3	2.13 ± 0.17
$\geq 75°$	20.7	2.23 ± 0.11

Table 5.5: Analysis results for each subset of Crab Nebula data after application of scaled Supercuts.

The validity of the scaled optimised Supercuts, derived from Crab Nebula data, was again tested using the Mrk 421 data. The significance and rates for all 22 Mrk 421 ON/OFF pairs when analysed with the combination of the scaling of optimised Supercuts from the different elevation ranges was found to be 33.2 σ with a rate of 2.70 ± 0.08 gamma rays per minute.

5.5 Kernel Analysis

The Supercuts analysis procedure is a type of selection known as box selection. Every event, when tagged with its image parameter values, can be considered

Parameter Cut	Extrapolated Cuts
Alpha	28°
Lower Length	0.13°
Upper Length	0.20°
Lower Width	0.05°
Upper Width	0.10°
Lower Distance	0.39°
Upper Distance	0.94°
Length/Size	0.00036°/ d.c.
Frac3	0.98

Table 5.6: Cuts extrapolated to elevation $< 50°$ from the scaling of optimised Supercuts. These cuts represent an elevation range subset that would lie below the $50° - 55°$ elevation range subset.

to exist at a point in n-dimensional parameter space. Upper and lower boundaries on parameter values define an n-dimensional box within this parameter space. Events which lie within the box are selected, those outside the box are rejected. This box acts as a filter to discriminate between gamma-ray events and background events.

Kernel analysis is an alternative approach which evaluates the likelihood that each individual event is a gamma-ray event or a background event by determining its relative proximity to a population of gamma-ray events or background events in parameter space. This closeness can be measured by a kernel function.

The kernel technique was applied in high-energy nuclear physics in the detection of the top quark (Holmström and Sain, 1997). The use of the technique in TeV gamma-ray astronomy has been described previously by Moriarty and Samuelson (2000). The method was found to be effective in improving the detection significance for strong gamma-ray sources (Crab Nebula, Mrk 421 and Mrk 501) but was not tested on weak sources. A previous attempt to use the method in the case of a weak source (the blazar 1ES 2344 +514) was unsuccessful because the data in that case consisted mainly of tracking runs (Quinn, 2005). This issue does not arise in the present investigation, where the IC 342 observations were all made in ON/OFF mode, and it was decided to apply the kernel analysis to the IC 342 data to establish whether it would improve the

significance of the signal (if any).

5.5.1 The Kernel Method

In kernel analysis, a real data event is placed in n-dimensional parameter space with a large population of simulated events.

The image parameters used for each event are length, l, and width, w, of the event ellipse, the distance, d, from the centre of the ellipse to the centre of the camera, the natural logarithm of the size, $\ln(s)$, of the image and alpha, α, the orientation angle of the ellipse. An event is then represented as a vector $p = (l, w, d, \ln(s), \alpha)$. Each event is then classified as a gamma-ray or background event depending on a likelihood ratio:

$$R = \frac{f_\gamma}{f_B} \tag{5.9}$$

where f_γ is the likelihood that it is a gamma-ray event and f_B is the likelihood that it is a background event. The likelihood of a gamma-ray event, f_γ, is estimated from a set of simulated gamma rays, N_γ, with parameter vectors $p_{\gamma i} = (l_i, w_i, d_i, \ln(s_i), \alpha_i)$:

$$f_\gamma = \frac{1}{N_\gamma} \sum_{i=1}^{N_\gamma} K(p - p_{\gamma i}) \tag{5.10}$$

The kernel function, $K(p - p_{\gamma i})$, is effectively a point-spread function describing the "influence" of vector $p_{\gamma i}$ at p. f_B is estimated in a similar way from a set of N_B real background events with parameter vectors $p_{Bi} = (l_i, w_i, d_i, \ln(s_i), \alpha_i)$:

$$f_B = \frac{1}{N_B} \sum_{i=1}^{N_B} K(p - p_{Bi}) \tag{5.11}$$

No simple function can describe the probability density distribution of gamma-ray images nor the distribution of background events. A simple dia-

grammatic representation of the kernel technique for a hypothetical univariate situation is shown in Figure 5.5. The probability density distribution of p can be crudely represented by a histogram, but the histogram is a less than ideal representation due to its discontinuous nature and its heavy dependence on the binning parameters used. A smoother continuous approximation to the true probability density distribution of p can be obtained by convolving each point in p with a point-spread function, to form a "kernel", and summing the results.

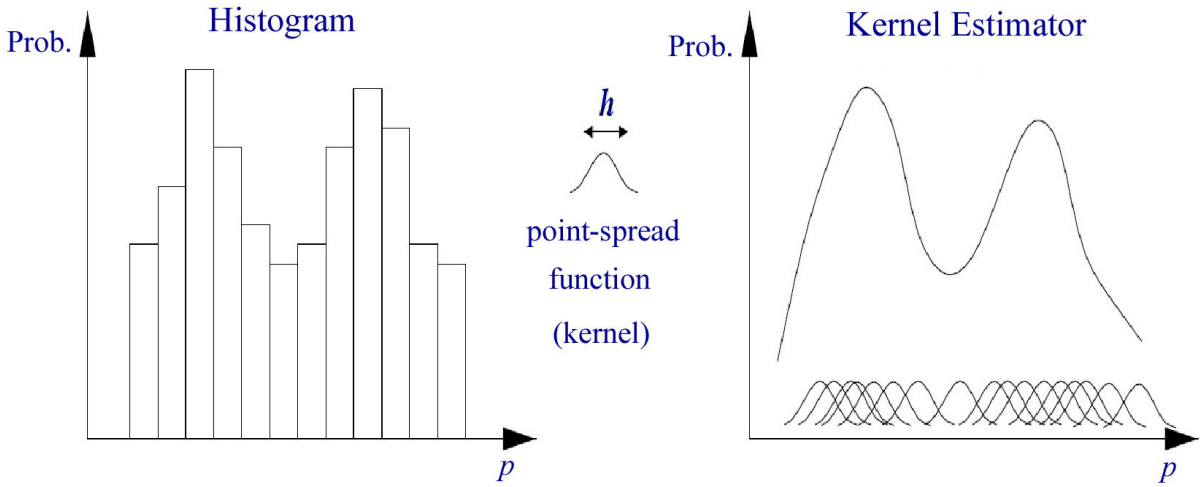

Figure 5.5: The kernel probability density estimator: each data point is convolved with a point-spread function which is then summed, producing a smooth approximation to the probability density distribution. Adapted from Quinn (2005).

The point-spread function which forms the kernel and the summing of these kernels is akin to Fourier analysis in which a single-valued periodic function may be built as a summation of individual sinusoidal components. In this work, a multivariate Gaussian is used as the kernel function (see Equations 5.13 and 5.14). For a kernel function that is the product of Gaussians, with one Gaussian in each dimension, a scaling factor, h_γ, is employed to minimise the mean integrated squared error between the kernel estimator and an actual distribution (Scott, 1992) and is given by:

$$h_\gamma = \left(\frac{4}{N_\gamma(n+2)}\right)^{\frac{1}{n+4}} \tag{5.12}$$

where n is the number of parameters and similarly for h_B. The probability distribution function (kernel estimator) is of the form:

$$f_\gamma = \frac{1}{N_\gamma h_\gamma \sqrt{(2\pi)^n |\xi_\gamma|}} \sum_{i=1}^{N_\gamma} \exp\left(-\frac{1}{2h_\gamma^2}(p - p_{\gamma i})^{\mathrm{T}} \xi_\gamma^{-1} (p - p_{\gamma i})\right) \tag{5.13}$$

where p is the coordinate in parameter space of the real data event, $p_{\gamma i}$ is the coordinate of the i^{th} simulated gamma-ray event, ξ_γ is the covariance matrix of the simulated gamma-ray dataset (giving the dependence of each parameter on every other parameter) and h_γ is the scale factor.

The background likelihood, f_B, for each event is calculated in the same manner except that real background data replace the simulated gamma-ray data.

$$f_B = \frac{1}{N_B h_B \sqrt{(2\pi)^n |\xi_B|}} \sum_{i=1}^{N_B} \exp\left(-\frac{1}{2h_B^2}(p - p_{Bi})^{\mathrm{T}} \xi_B^{-1} (p - p_{Bi})\right) \tag{5.14}$$

where N_B is a set of real background events with parameter vectors p_{Bi} and ξ_B is the covariance matrix of the background dataset.

For each event recorded in the ON and OFF dataset, the image is parameterised to give the vector p. The logarithmic of the likelihood ratio, $\log(R)$, is then a measure of the probability that the event is a gamma-ray event:

$$\log(R(p)) = \log\left(\frac{f_\gamma(p)}{f_B(p)}\right) \tag{5.15}$$

In an ideal distribution of $\log(R)$ values, gamma-ray events would be expected to have positive $\log(R)$ values, and background events negative $\log(R)$ values.

Each event in n-dimensional parameter space is tagged with a $\log(R)$ value. A cut, R_{cut}, applied to the $\log(R)$ values. R_{cut} is essentially a contour in n-space. Events are selected as gamma-ray events, the rest are assumed to be background. The kernel estimator (probability distribution function) in effect converts an n-dimensional box parameter selection into a one-dimensional selection. The boundary value, R_{cut}, is determined experimentally in the same manner in which parameter values are determined for the optimisation of Supercuts (Section 5.4.3). The value chosen is the one which gives the best signal significance on a test dataset. For a given R_{cut} value, the significance is determined by using the same standard Poisson excess calculation as in Equations 5.6 and 5.7:

$$\sigma_{EXCESS} = \frac{N_{ON} - N_{OFF}}{\sqrt{N_{ON} + N_{OFF}}} \tag{5.16}$$

and gamma-ray rate:

$$r \pm \Delta r = \frac{N_{ON} - N_{OFF}}{t} \pm \frac{\sqrt{N_{ON} + N_{OFF}}}{t} \tag{5.17}$$

where N_{ON} and N_{OFF} are the number of events with $\log(R) \geq R_{cut}$ in the ON and OFF datasets respectively and t is the duration of observation of the source.

5.5.2 Reduction of Computational Overhead

Kernel analysis is computationally intensive, as every event is compared with every gamma-ray simulation and with every background event. Two possibilities for reducing the analysis time have been investigated, pre-selection of events and lattice analysis (Moriarty and Samuelson, 2000).

Since most events in the dataset are not gamma-ray-initiated, many can be eliminated with loose cuts on individual parameters before applying the kernel analysis. By rejecting in advance those events whose parameters values fall well within the background regions of parameter space, it is possible to reduce the kernel analysis computational workload, without significantly affecting the final

Parameter	Lower Cut	Upper Cut
Length	0°	0.40°
Width	0°	0.20°
Alpha	0°	55°
ln(Size)	0 d.c.	–

Table 5.7: Kernel pre-selection cuts.

results. The pre-selection method can reduce the number of calculations by a factor of five and is the method employed in this work.

The probability distributions f_γ and f_B defined by Equations 5.13 and 5.14, represent the convolution of the gamma-ray simulations and background samples with a kernel (point-spread) function. Therefore, the value of the log-likelihood function, $\log(R)$, can be precalculated for a lattice of points in the n-dimensional parameter space. Values between the nodes of the lattice can be estimated using linear piecewise interpolation (Moriarty and Samuelson, 2000). The lattice analysis need only perform one linear piecewise interpolation per event, resulting in a reduced analysis time rather than a comparison with all simulated gamma rays and background events. While producing the required lattice requires many more calculations than a typical full kernel analysis, it need only be carried out once per detector configuration.

5.5.3 Gamma-Ray Simulations

In practice the kernel technique calculates the probability that an event is a gamma-ray event or a background event by comparing its properties to that of a database of simulated gamma rays and real background events. Any real background data recorded using the same telescope configuration during the same season of observation may be used in this analysis. The simulated gamma-ray events were generated using the GrISU software program developed jointly by Grinnell College, Iowa and Iowa State University. The GrISU simulations program may be differentiated into three distinct procedures.

- Simulation of extensive air showers: The generation of simulated EASs

is accomplished by a program routine known as *KASCADE*, a modified version of that originally developed by Kertzman and Sembroski (1994). The *KASCADE* routine simulates the physics of the particle showers that occur in the atmosphere. It traces out the trajectories of all the particles created in the EAS as the gamma rays interact with nuclei and produce electron-positron pairs. *KASCADE* creates a 3-dimensional map of the EAS, reconstructing the interactions of each secondary particle as it descends through a model atmosphere.

- Simulation of Cherenkov emission: The 3-dimensional map created by *KASCADE* is forwarded to the routine *Cherenkf*, the second program in the simulation procedure. *Cherenkf* uses the 3-D maps to simulate the physics of the Cherenkov emission from each of the particles. It models the atmosphere and index of refraction, calculates emission angles and tracks each photon until it arrives on the ground (Carter-Lewis, 1992).

- Simulation of the detector: The final procedure models the optical and electronic processes in the telescope system. The *GrISUDet* program tracks individual Cherenkov photons as they reflect from the mirrors and illuminate the camera and models the charge pulses produced by the photomultiplier tubes and subsequent electronics. At this stage, artificial noise can also be injected into the data to reflect the level of background light expected at the telescope. The most suitable noise level to inject can be identified by varying the amount of noise in the simulations and comparing the resulting pedestal variance distribution to that of real data.

Simulated events which have an energy above the energy threshold of the telescope will result in a trigger and will be recorded. These simulated recorded events are subjected to the same image cleaning, calibration and parameterisation as for real Cherenkov events and can then be used for the kernel analysis or for diagnostic investigations. In this work, sets of 100000 gamma-ray events with spectral index equal to that of the Crab Nebula were simulated for each

Crab Nebula Data	Supercuts 2000	Optimised Cuts	Scaled Optimised Cuts	Kernel Analysis
Significance (σ)	20.9	28.0	29.5	29.9
Rate (γ/minute)	2.47 ± 0.12	1.34 ± 0.05	1.84 ± 0.06	1.74 ± 0.06

Table 5.8: A comparison of Supercuts 2000, optimised cuts, scaled optimised cuts and kernel analysis applied to Crab Nebula data.

Mrk 421 Data	Supercuts 2000	Optimised Cuts	Scaled Optimised Cuts	Kernel Analysis
Significance (σ)	33.0	31.7	33.2	38.9
Rate (γ/minute)	5.00 ± 0.15	2.14 ± 0.08	2.70 ± 0.08	3.24 ± 0.08

Table 5.9: A comparison of Supercuts 2000, optimised cuts, scaled optimised cuts and kernel analysis applied to Mrk 421 data.

elevation at which the IC 342 dataset was recorded, resulting in $\sim 1.5 \times 10^6$ simulated events.

5.5.4 Optimisation of Kernel Cut

As mentioned in Section 5.5.1, the $\log(R)$ cut must be optimised to give the best significance for the dataset under investigation. Simplistically, if gamma-ray and background events were completely distinct, the R_{cut} boundary separating both populations would occur at zero, making discrimination easy. Unfortunately, the two distributions overlap to some extent, so optimisation is required to determine the most efficient cut value. The kernel analysis effectively merges the five parameters (length, width, distance, ln(size) and α) into a single $\log(R)$ score so that only one parameter needs to be optimised in this case.

To determine the optimal cut, the same Crab Nebula data which were used in the Supercuts optimisation analysis in Section 5.4.3 were again used.

From Figure 5.6, a value of 4.97 was chosen as the optimised kernel cut. For this value of R_{cut}, the significance for the 41 Crab Nebula ON/OFF pairs after is found to be 29.9 σ with a rate of 1.74 ± 0.06 gamma rays per minute. Table 5.8 shows that for the Crab Nebula data, the significance and rate obtained from the kernel optimisation is greater than the result from the optimisation

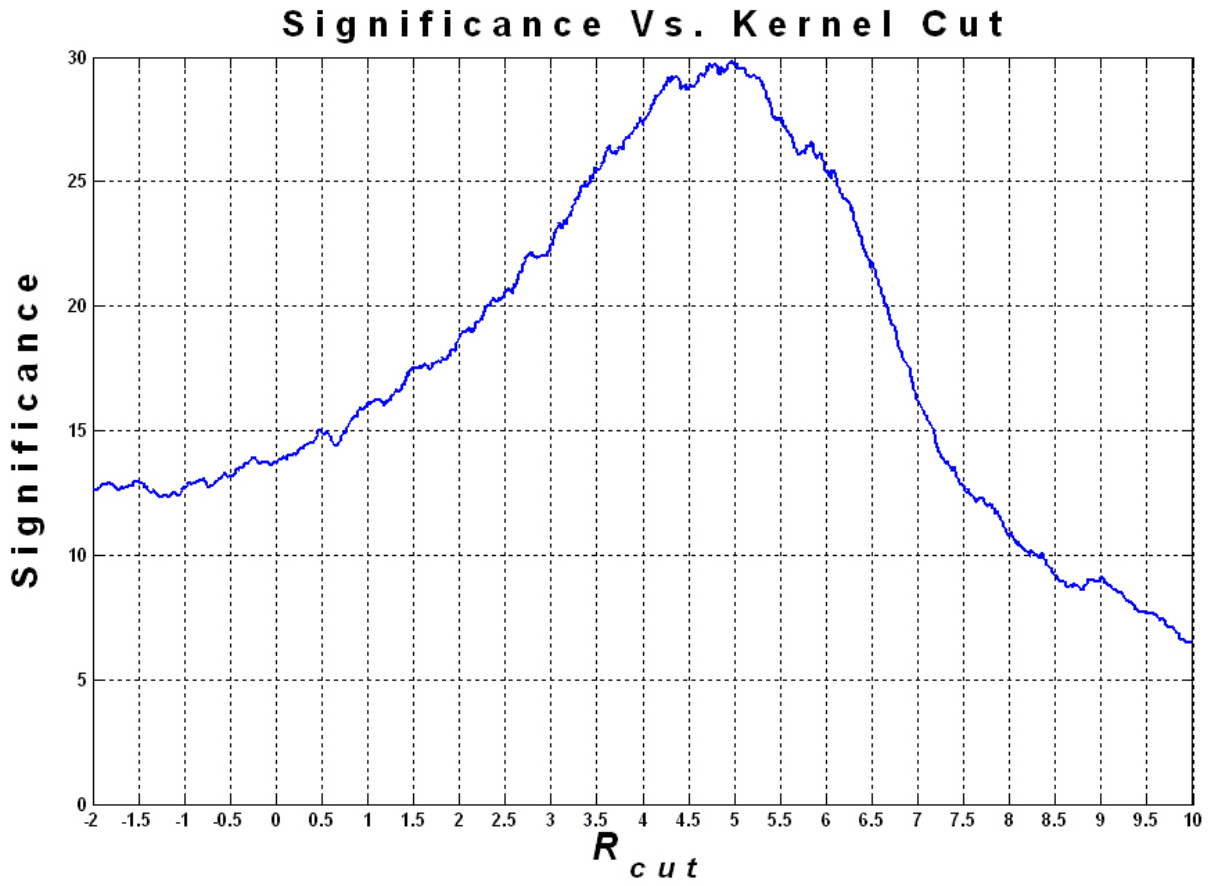

Figure 5.6: A kernel analysis of 41 Crab Nebula ON/OFF pairs. The peak of this distribution indicates the optimal kernel cut value (R_{cut}). The maximum significance is obtained for $R_{cut} = 4.97$.

of Supercuts and slightly greater than the result from the scaled optimised Supercuts.

The validity of the kernel cut optimisation, derived from Crab Nebula data, was tested using the Mrk 421 dataset described in Section 5.4.3. Figure 5.7 shows the plot of significance against R_{cut} for the Mrk 421 data. The significance for the 22 Mrk 421 ON/OFF pairs using the value $R_{cut} = 4.97$ optimised on the Crab Nebula dataset was found to be 38.9 σ with a rate of 3.24 $\pm$ 0.08 gamma rays per minute.

Table 5.9 shows that for the Mrk 421 data, the significance and rate obtained from the kernel optimisation is greater than the result from the optimisation of Supercuts and scaled optimised Supercuts. A complete graphical representation

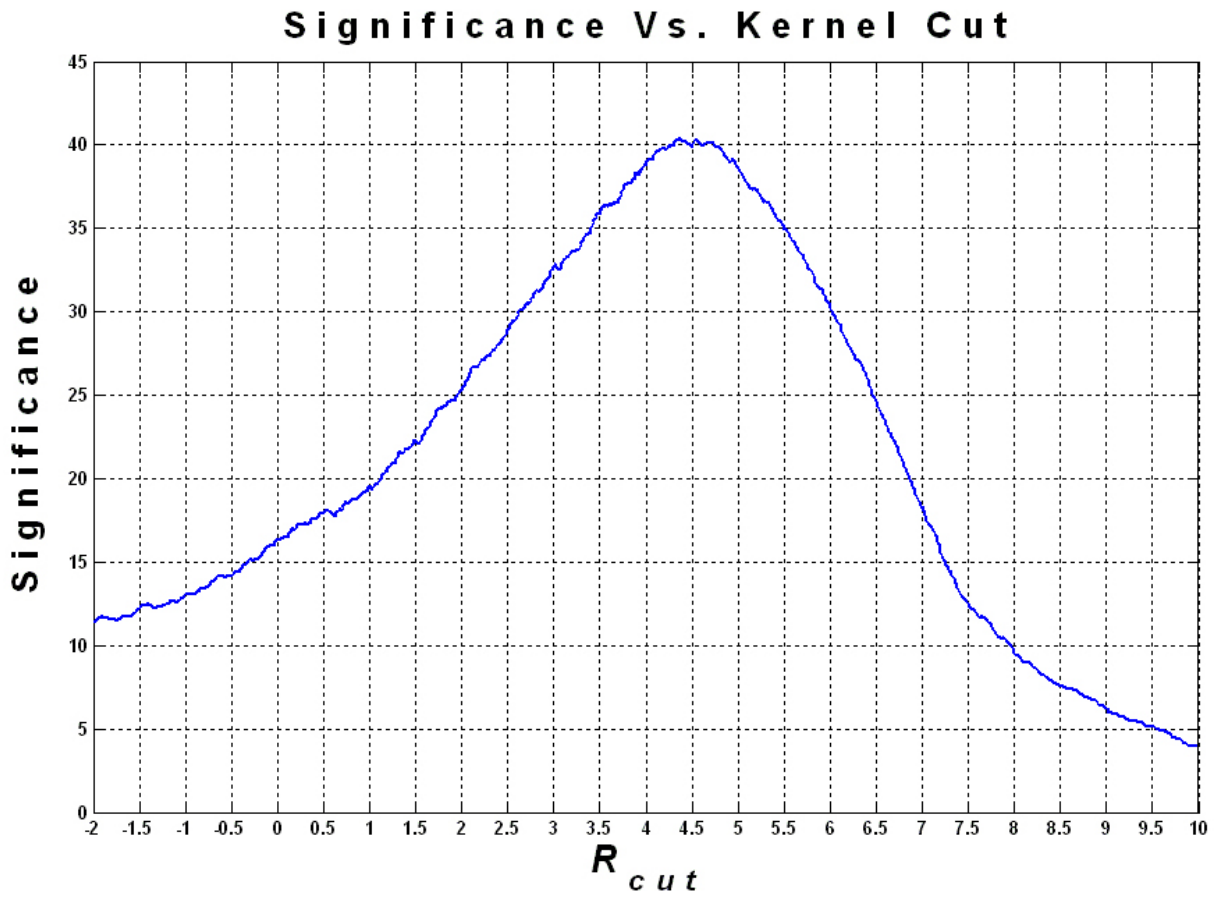

Figure 5.7: A kernel analysis of 22 Mrk 421 ON/OFF pairs.

of the overall kernel analysis procedure can be seen in Figure 5.8.

5.6 Flux Calculation

As seen in the previous sections the analysis methods are applied to a recorded dataset to determine the significance and rate of TeV gamma-ray emission. While the detection rate is typically expressed as number of gamma-ray counts per minute, a more useful expression is obtained if the detection rate is converted to a *flux* expressed as number of gamma-ray counts per unit area per unit time (e.g. $m^{-2}s^{-1}$) above the energy threshold. The flux allows for a more direct comparison between different instruments.

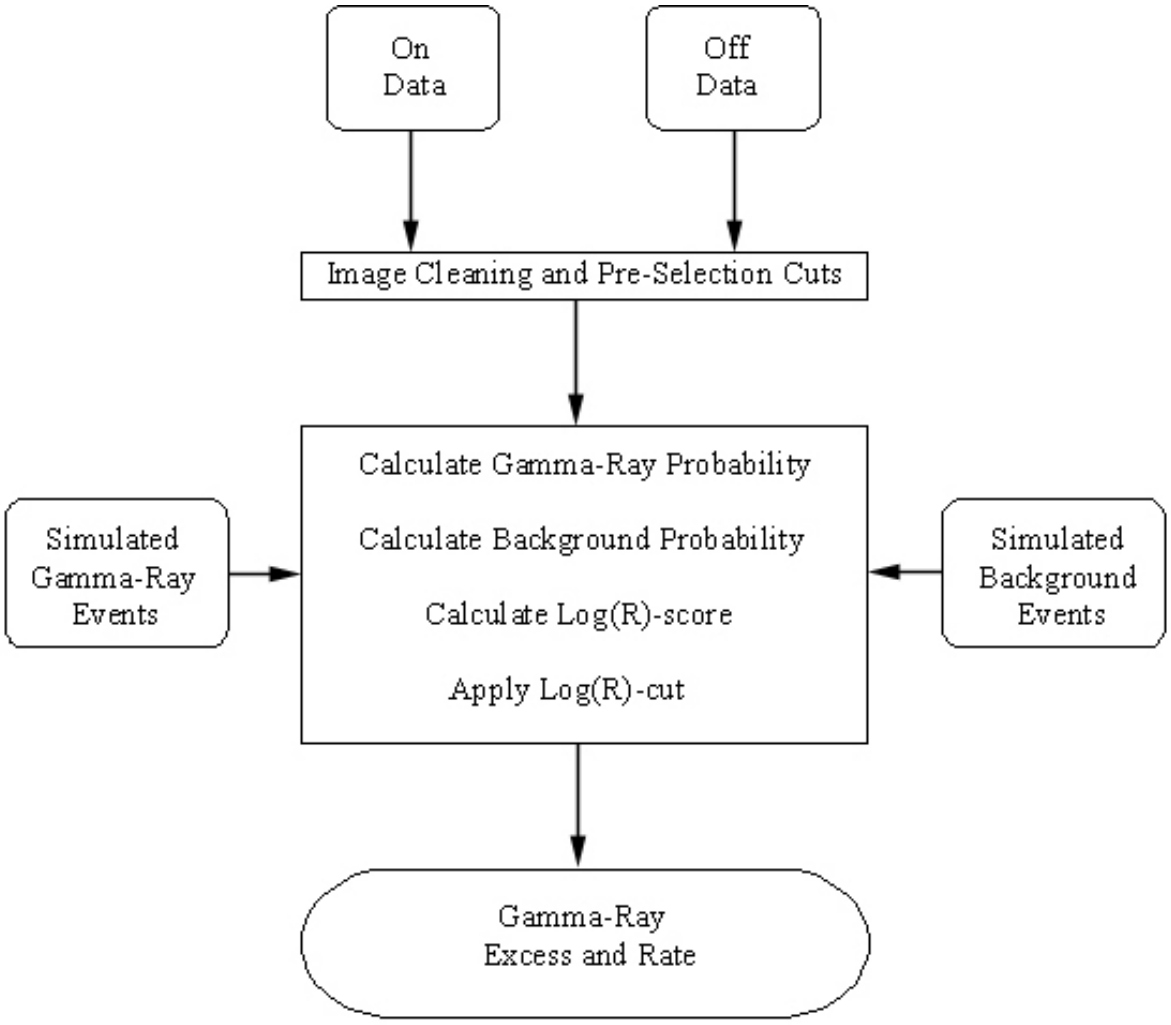

Figure 5.8: The kernel analysis procedure for ON/OFF data.

5.6.1 Determination of Effective Collection Area

To determine the flux, the collection area of the telescope must first be determined. The collection area of an IACT detector represents the area over which gamma-ray and background events trigger the telescope and is a measure of the efficiency of gamma-ray detection over a range of energies. In order to determine the collection area it is necessary to perform an exact calibration of the telescope and the gamma-ray selection technique employed as the sensitivity of the telescope to gamma rays is dependent on the gamma-ray selection procedures performed on the raw data. Simply, the collection area is dependent on the selection procedure. Also the collection area increases as a function of incident energy while the gamma-ray flux from an object decreases with increasing energy, thereby complicating the energy response of the detector. The collection area must therefore be calculated for each gamma-ray selection procedure and also for each observing season, due to upgrades or degradation to the telescope hardware.

The collection area was determined directly from gamma-ray simulations. Gamma-ray air showers were simulated with an impact radius of 320 m which defines a circular area A_0 perpendicular to the optical axis of the telescope. These simulations are those discussed previously in Section 5.5.3. The collection area at a particular energy, $A(E)$, can be calculated by projecting a number of simulated showers ($N_{incident}$) over an area A_0, and counting the number which trigger the telescope and pass the gamma-ray selection criteria ($N_{trig+cuts}$). The collection area at a given energy is calculated by;

$$A(E) = A_0 \left(\frac{N(E)_{trig+cuts}}{N(E)_{incident}} \right) \tag{5.18}$$

For very low energies, the collection area is expected to be small, as the Cherenkov light produced is insufficient to trigger the telescope. In principle, the collection area is large for high-energy showers; however, such showers may be rejected by the distance cut. The collection area is also dependent on the

zenith angle of the telescope, thus simulations appropriate to the range of zenith angles used for observations must be used in approximating the collection area.

However, $A(E)$ is not sufficient to characterise the response of the telescope to a particular gamma-ray source without incorporating the effect of the source spectrum. This is achieved by convolving the collection area curve with the source spectrum (assumed to follow a power law), resulting in a differential response curve:

$$\frac{dr}{dE} = A(E).I_\gamma.E^{-\alpha} \tag{5.19}$$

where r is the gamma-ray rate, I_γ is the flux constant, and α is the differential spectral index. The differential response curve provides a measure of the true sensitivity of the telescope to gamma rays from the object under investigation.

Using the simulation dataset detailed in Section 5.5.3, the collection area and energy threshold values were calculated. The energy thresholds were calculated assuming a Crab-Nebula-like spectrum, i.e., $I_\gamma.E^{-\alpha} = 3.20 \times 10^{-7} \times (E/\mathrm{TeV})^{-2.49}$ m^{-2} s^{-1} TeV^{-1} (Hillas et al., 1998). The conventional definition of the energy threshold (E_{th}) is the point where the differential rate of gamma rays from the Crab Nebula reaches a maximum. This effectively occurs at the peak in the differential response curve (see Figures 5.9 (bottom), 5.10 (bottom) and 5.11 (bottom)). Thus the conventional energy threshold is the collector's peak response energy (PRE) to a Crab-Nebula-like spectrum.

The other parameter used in classifying the response of the telescope is the effective collection area (A_{eff}). This can be derived in terms of the collection area function $A(E)$ using a method similar to that of Kertzman and Sembroski (1994):

$$R(> E_{th}) = \int_{E_{th}}^{\infty} A(E) I_\gamma E^{-\alpha}\, dE = A_{eff} \int_{E_{th}}^{\infty} I_\gamma E^{-\alpha}\, dE \tag{5.20}$$

Rearranging we have an expression for the effective area:

$$A_{eff} = \frac{R(> E_{th})}{Flux(> E_{th})} = \frac{\int_{E_{th}}^{\infty} A(E) I_\gamma E^{-\alpha}\, dE}{\int_{E_{th}}^{\infty} I_\gamma E^{-\alpha}\, dE} \tag{5.21}$$

This calculation is effectively a division of the area under the differential response curve by the area under the source spectrum, from the energy threshold upwards. The effective area for Supercuts, optimised Supercuts and scaled Supercuts in this work was found to be (3.25 ± 0.04) × 10^4 m^2, (2.12 ± 0.04) × 10^4 m^2 and (7.01 ± 0.02) × 10^4 m^2 respectively. These are shown in Figures 5.9 (top), 5.10 (top) and 5.11 (top). The effective area for Supercuts was used as the effective area for the kernel analysis; while this is clearly not a valid assumption (since as seen in Tables 5.8 and 5.9, the gamma-ray rates obtained with kernel analysis are ∼ 30 % lower than for Supercuts), a more detailed analysis was not carried out for the present work.

5.6.2 Flux Upper Limits

If the analysis of a source results in a non-detection, i.e., if the excess is not statistically significant, it is possible to impose upper limits on the number of gamma-ray events coming from the target object. In this work, upper limits were derived using a three-step process.

Firstly, the Helene (1983) method calculates the probability density function of the number of source events based on the number of events in the ON and OFF dataset. Using the probability density function it is possible to determine the maximum number of events coming from the source with a given confidence level, assuming statistical fluctuations only. In practice, the upper limit on the number of counts, N_{ul}, is calculated by numerically solving the equation:

$$1 - CL = \frac{I\left(\frac{N_{ul}-N}{\sigma}\right)}{I\left(\frac{-N}{\sigma}\right)} \tag{5.22}$$

where CL is the desired confidence level (e.g., 0.999), N is the excess number of events ($N_{ON} - N_{OFF}$), σ is the standard deviation of the background number

of events ($\sqrt{N_{ON} + N_{OFF}}$) and $I(z)$ is the error function of the form:

$$I(z) = \frac{1}{\sqrt{2\pi}} \int_z^{\infty} e^{\frac{-x^2}{2}}\, dx \tag{5.23}$$

To convert the upper limit on the number of counts to a flux upper limit, an intermediate step is applied whereby the upper limit on the number of counts (N_{ul}) is converted to an upper limit of the gamma-ray rate from the Crab Nebula (UL_{cu}) in terms of the average rate from the Crab Nebula ($rate_{Crab}$) for the same season of observation as the object under investigation:

$$UL_{cu} = \frac{\frac{N_{ul}}{t}}{rate_{Crab}} \tag{5.24}$$

where t is the number of minutes spent observing the object. Finally, this upper limit in Crab Nebula units can then be converted into an absolute flux (UL_{abs}) above the energy threshold of the telescope by assuming a Crab-Nebula-like spectrum:

$$UL_{abs} = UL_{cu} \times F_{Crab}(E > E_{th}) \tag{5.25}$$

where $F_{Crab}(E > E_{th})$ is the Crab Nebula integral flux above the energy threshold of the telescope (E_{th}) for the relevant season. The Crab Nebula integral flux above a given energy threshold E_{th} is calculated using;

$$F_{Crab}(E > E_{th}) = 3.20 \times 10^{-7} \int_{E_{th}}^{\infty} (E/\mathrm{TeV})^{-2.49}\, dE \tag{5.26}$$

This flux upper limit calculation assumes that the VHE Crab Nebula flux is constant so that changes in the observed Crab Nebula count rate are most likely due to changes in the telescope or instrument sensitivity, variable weather conditions or energy threshold (Aharonian et al., 2004).

The energy thresholds for Supercuts, optimised Supercuts and scaled Supercuts in this work was found to be 0.38 TeV, 0.46 TeV and 0.60 TeV, respec-

tively (see the bottom panels of Figures 5.9 − 5.11). For simplicity, the energy threshold for the Supercuts was used as the energy threshold for the kernel analysis. The Crab Nebula flux integrated above each of these energy thresholds gives $F_{Crab}(E > 0.38 \text{ TeV}) = 1.35 \times 10^{-6} \text{ m}^{-2} \text{ s}^{-1}$, $F_{Crab}(E > 0.46 \text{ TeV}) = 1.02 \times 10^{-6} \text{ m}^{-2} \text{ s}^{-1}$, $F_{Crab}(E > 0.60 \text{ TeV}) = 6.85 \times 10^{-7} \text{ m}^{-2} \text{ s}^{-1}$ and $F_{Crab}(E > 0.38 \text{ TeV}) = 8.91 \times 10^{-7} \text{ m}^{-2} \text{ s}^{-1}$ for Supercuts, optimised Supercuts, scaled Supercuts and kernel cuts, respectively.

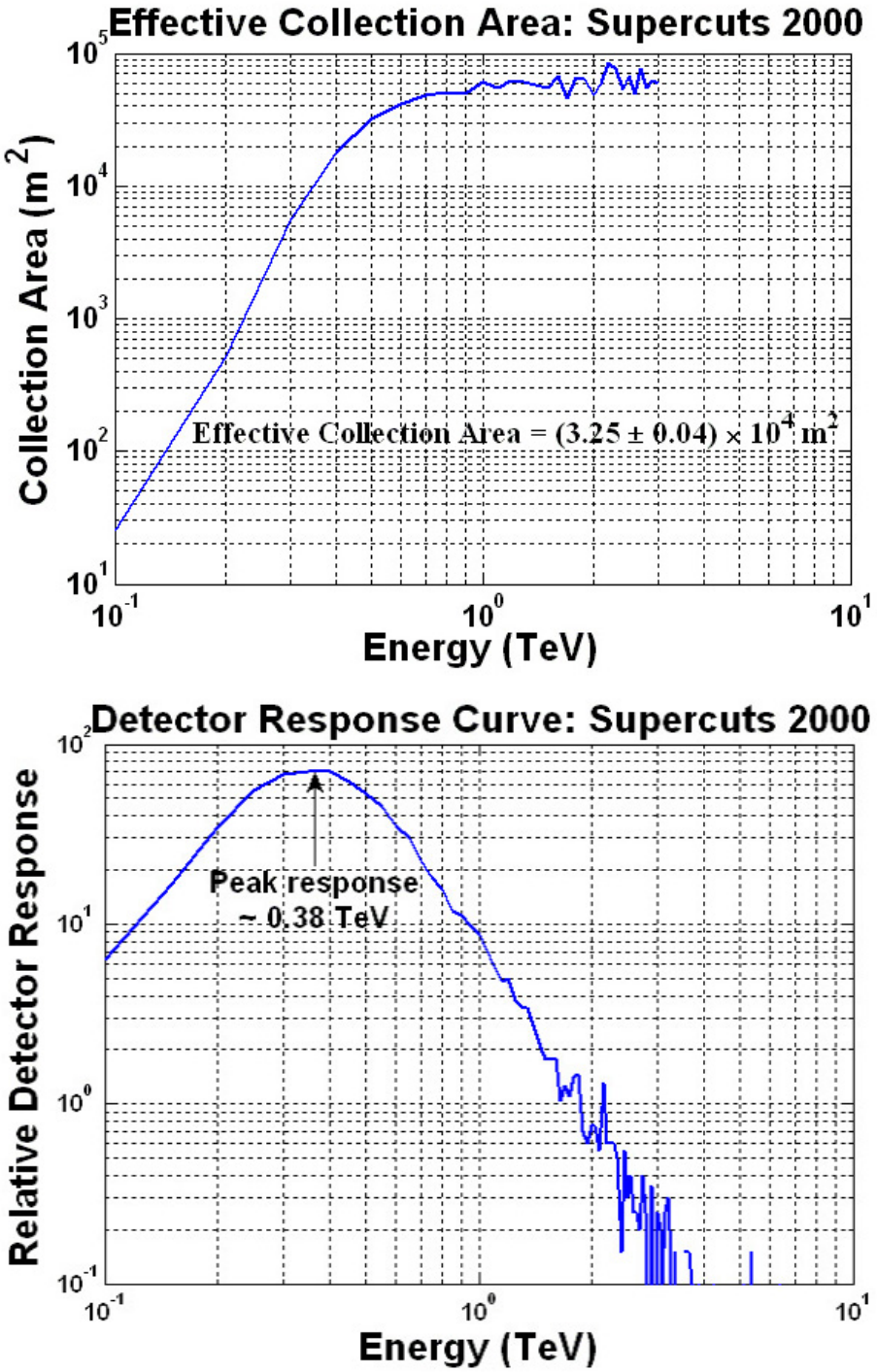

Figure 5.9: Collection area distribution (top) and differential response curve (bottom) using 100000 simulated gamma-ray events describing the Whipple 10m telescope response to a source with a Crab-Nebula-like spectrum using Supercuts 2000.

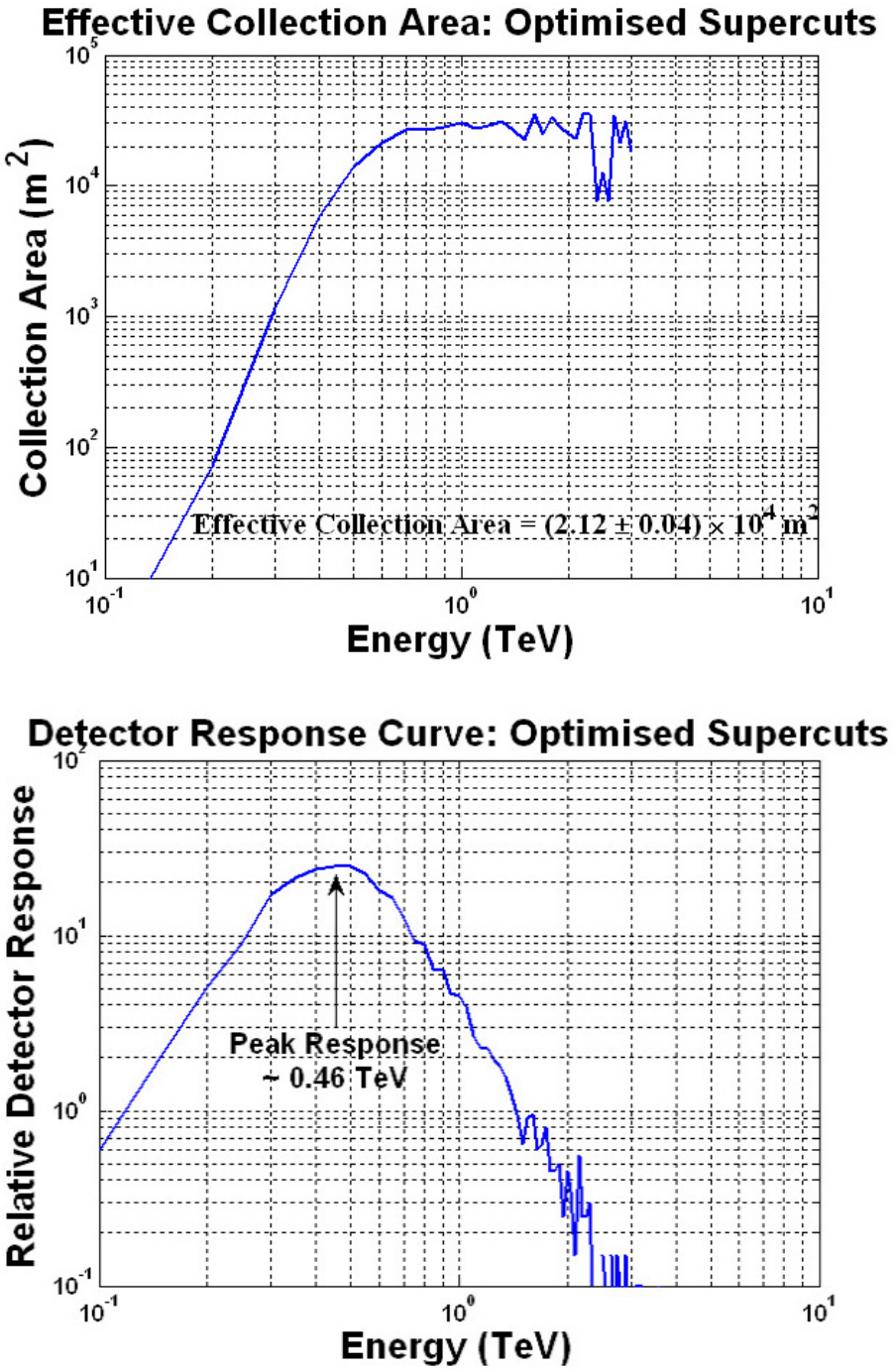

Figure 5.10: Collection area distribution (top) and differential response curve (bottom) using 100000 simulated gamma-ray events describing the Whipple 10m telescope response to a source with a Crab-Nebula-like spectrum using optimised Supercuts.

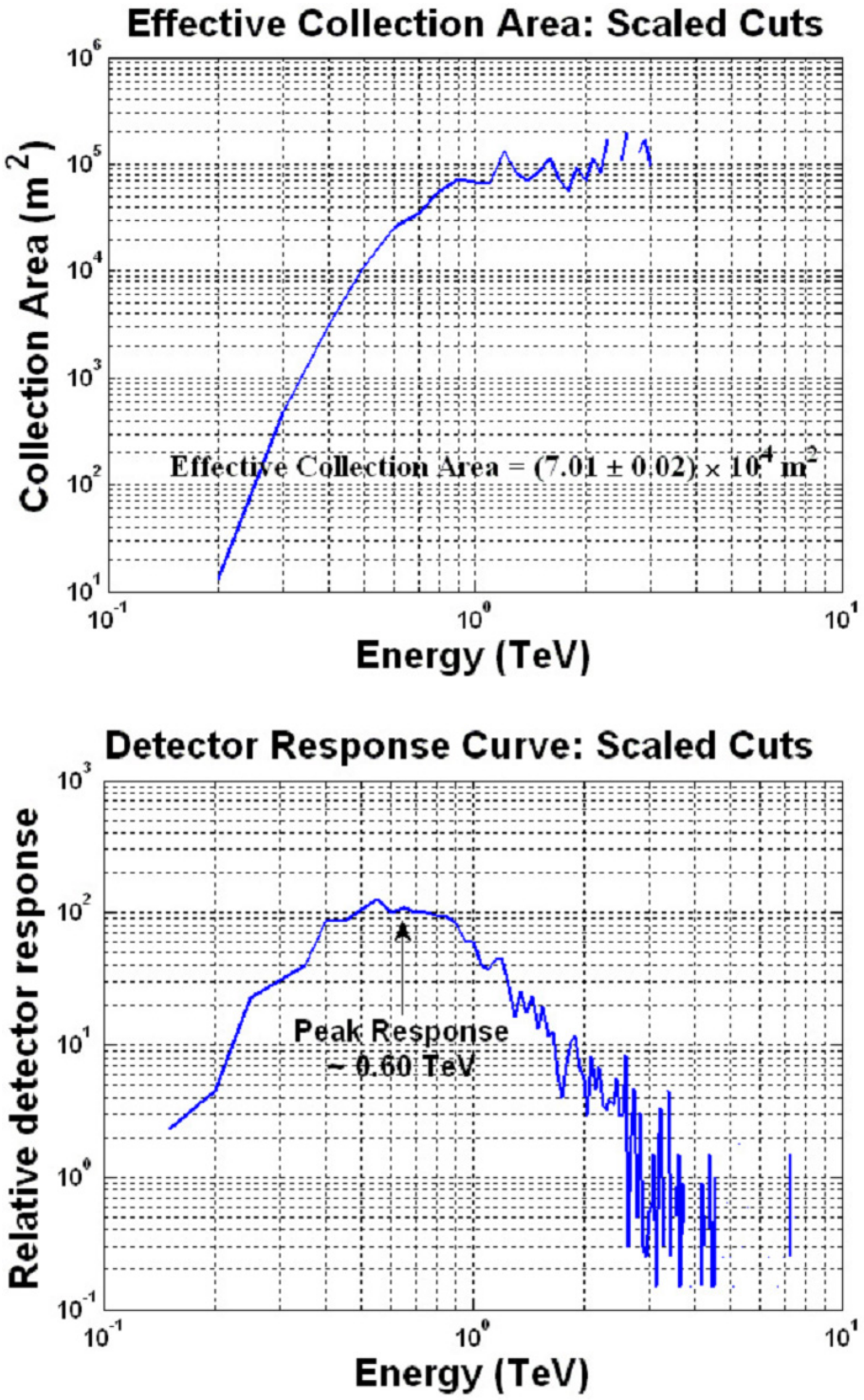

Figure 5.11: Collection area distribution (top) and differential response curve (bottom) using 100000 simulated gamma-ray events describing the Whipple 10m telescope response to a source with a Crab-Nebula-like spectrum using scaled optimised cuts.

Chapter 6

VHE Observations of the Starburst Galaxy IC 342.

6.1 Introduction

This work is concerned with a search for VHE gamma radiation from the starburst galaxy IC 342. The observations of IC 342 were carried out at the Fred Lawrence Whipple Observatory on Mount Hopkins, Arizona, during the observing season of 2003 − 2004. The observational data were analysed as described in Chapter 5. In this chapter, the results of this analysis are presented in Section 6.2, followed by concluding remarks.

6.2 Results of Search for VHE Gamma Radiation from the Starburst Galaxy IC 342.

The database of IC 342 observations comprises 51 ON/OFF pairs with a total exposure time of 1428 minutes, taken between October 2003 and April 2004. The runs were all taken in good weather, had stable cosmic-ray rates and were free of any hardware or data-acquisition problems. Unfortunately, because of its declination, the maximum elevation angle of IC 342 observed from the Whipple Observatory is only 54°. The observations reported here were recorded at elevation angles between 41° and 54°. The parameterised events were subjected to the discrimination criteria of Supercuts 2000, optimised Supercuts, scaled Supercuts and kernel analysis as described in Chapter 5.

IC 342 Data	Supercuts 2000
Events On (N_{ON})	9990
Events Off (N_{OFF})	9951
Excess Events	39
Significance (σ)	0.276
Rate (gamma rays/minute)	0.027 ± 0.099
Effective Area (m^2)	$(3.25 \pm 0.04) \times 10^4$
Upper Limit (N_{ul} Helene 99.9 %)	495
Energy Threshold (E_{th})	0.38 TeV
Flux Upper Limit (m^{-2} s^{-1})	1.78×10^{-7}

Table 6.1: Analysis results for 51 IC 342 ON/OFF pairs from the 2003 − 2004 observing season after application of standard Supercuts 2000.

6.2.1 Supercuts Results

The results obtained by applying standard Supercuts 2000 to the IC 342 dataset are presented in Table 6.1. The alpha distribution plot for the IC 342 dataset after application of these cuts is depicted in Figure 6.1. There is no discernable difference between the ON and OFF data, and it is clear that no gamma-ray signal is present.

6.2.2 Optimisation of Supercuts Results

The results obtained by applied the optimised Supercuts described in Section 5.4.3 to the IC 342 dataset are presented in Table 6.2, and the corresponding alpha distribution plot is shown in Figure 6.2.

6.2.3 Scaling of Optimised Supercuts Results

The original Supercuts 2000 and the re-optimised Supercuts are derived for observations at large elevation angles, and are therefore not directly applicable to the IC342 observations described here. The scaled cuts derived in Section 5.4.4 are designed to overcome this problem. The results obtained by applying the scaled cuts are presented in Table 6.3, and the corresponding alpha distribution plot is shown in Figure 6.3. Even with the scaled cuts, there is no evidence for a gamma-ray signal in the IC 342 data.

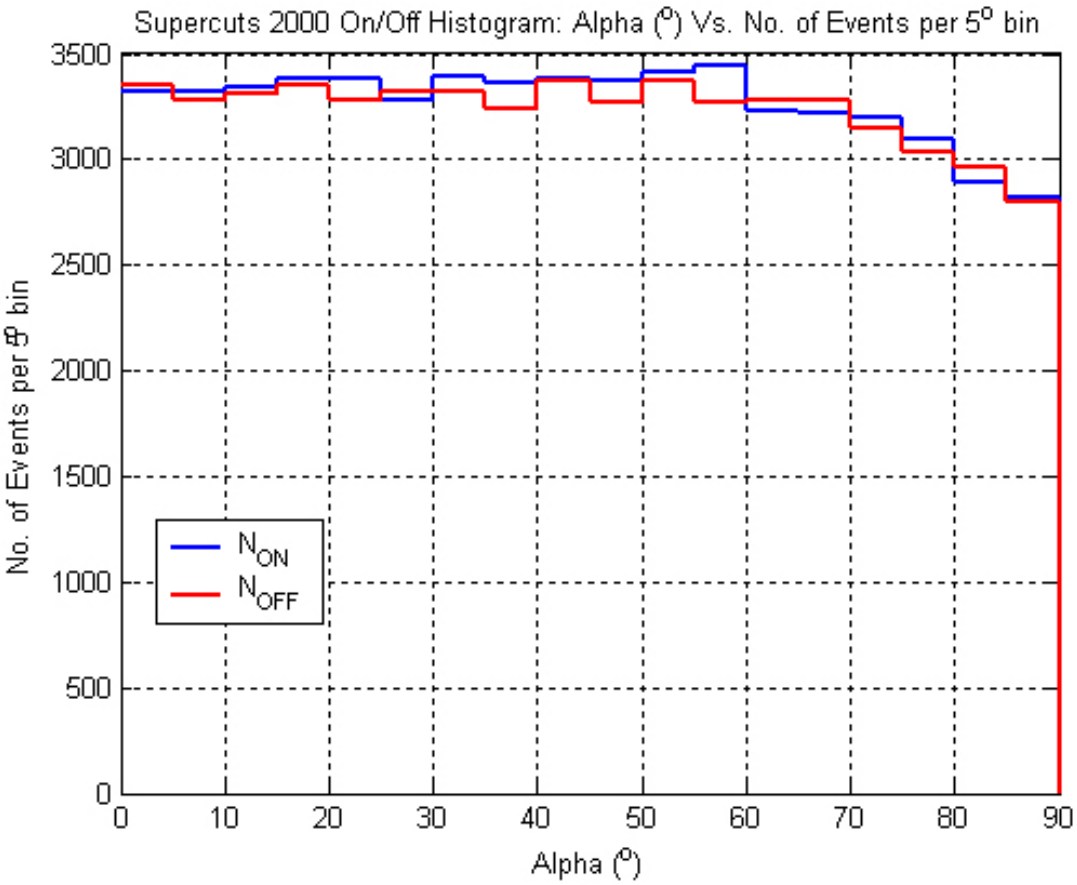

Figure 6.1: Alpha distribution plot for 51 IC 342 ON/OFF pairs from the 2003 − 2004 observing season after application of standard Supercuts 2000.

IC 342 Data	Optimised Supercuts
Events On (N_{ON})	1058
Events Off (N_{OFF})	1063
Excess Events	-5
Significance (σ)	-0.108
Rate (gamma rays/minute)	-0.003 ± 0.032
Effective Area (m^2)	(2.12 ± 0.04) × 10^4
Upper Limit (N_{ul} Helene 99.9 %)	147
Energy Threshold (E_{th})	0.46 TeV
Flux Upper Limit (m^{-2} s^{-1})	8.10 × 10^{-8}

Table 6.2: Analysis results for 51 IC 342 ON/OFF pairs from the 2003 − 2004 observing season after application of optimised Supercuts.

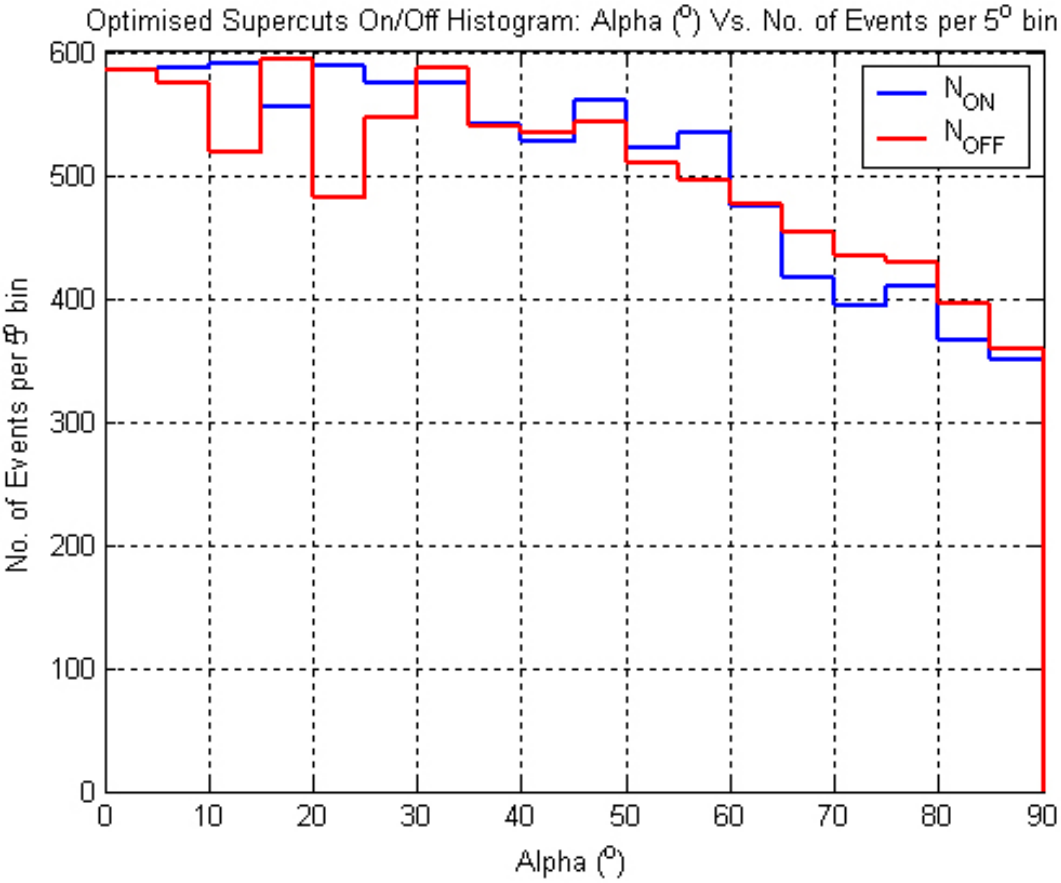

Figure 6.2: Alpha distribution plot for 51 IC 342 ON/OFF pairs from the 2003 − 2004 observing season after application of optimised Supercuts.

IC 342 Data	Scaled Optimised Supercuts
Events On (N_{ON})	3760
Events Off (N_{OFF})	3708
Excess Events	52
Significance (σ)	0.602
Rate (gamma rays/minute)	0.036 ± 0.060
Effective Area (m^2)	$(7.01 \pm 0.02) \times 10^4$
Upper Limit (N_{ul} Helene 99.9 %)	327
Energy Threshold (E_{th})	0.60 TeV
Flux Upper Limit (m^{-2} s^{-1})	5.46×10^{-8}

Table 6.3: Analysis results for 51 IC 342 ON/OFF pairs from the 2003 − 2004 observing season after application of scaled Supercuts.

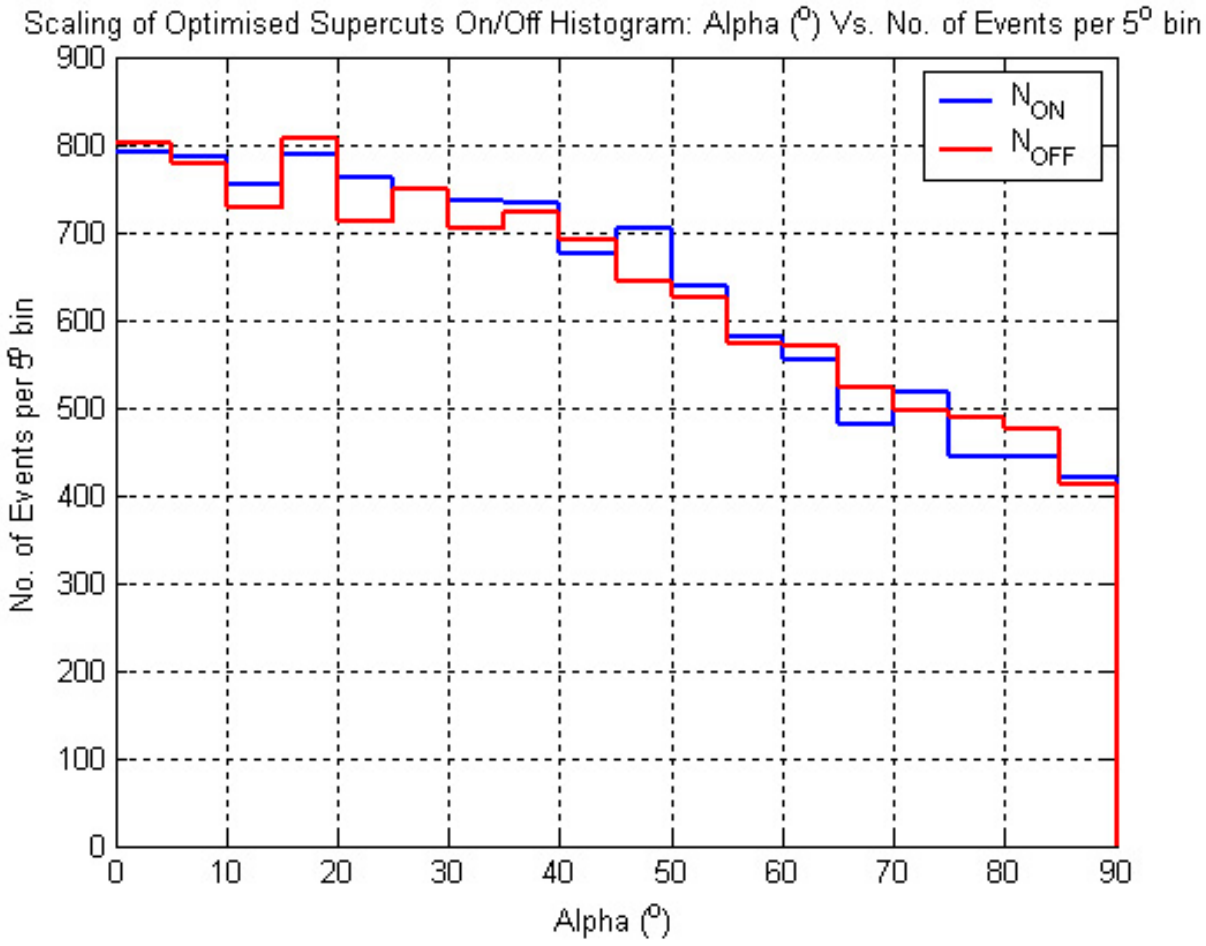

Figure 6.3: Alpha distribution plot for 51 IC 342 ON/OFF pairs from the 2003 − 2004 observing season after application of scaled optimised Supercuts.

IC 342 Data	Kernel Analysis
Kernel Cut	4.97
Events On (N_{ON})	1697
Events Off (N_{OFF})	1675
Excess Events	22
Significance (σ)	0.379
Rate (gamma rays/minute)	0.015 ± 0.041
Time Recorded (minutes)	1425.032
Effective Area (m^2)	$(3.25 \pm 0.04) \times 10^4$
Upper Limit (N_{ul} Helene 99.9 %)	208
Energy Threshold (E_{th})	0.38 TeV
Flux Upper Limit (m^{-2} s^{-1})	7.47×10^{-8}

Table 6.4: Kernel analysis results of IC 342 data from the $2003 - 2004$ observing season.

6.2.4 Kernel Analysis Results

Kernel analysis was applied to the IC 342 dataset as a whole and was also applied to the individual data pairs grouped by elevation range. 100000 gamma-ray events were simulated for each elevation at which the IC 342 dataset was recorded. The results of applying the kernel analysis to the IC 342 dataset are presented in Table 6.4. A plot of gamma-ray significance versus $\log(R)$ cut is shown in Figure 6.4. The $\log(R)$ cut of 4.97 derived from the kernel optimisation on Crab Nebula data gave a significance of 0.379 σ consistent with the results from the other analysis methods. An upper limit was calculated at the 99.9 % confidence level using the method described in Section 5.6.2. Although the kernel analysis has proved very successful when applied to strong gamma-ray sources like the Crab Nebula and Mrk 421, its efficacy has not been established for weak sources.

6.3 Discussion of Results: IC 342

The results obtained using the different analysis methods are compared in Table 6.5, where the flux upper limits have also been expressed in terms of the Crab Nebula flux for the appropriate energy threshold.

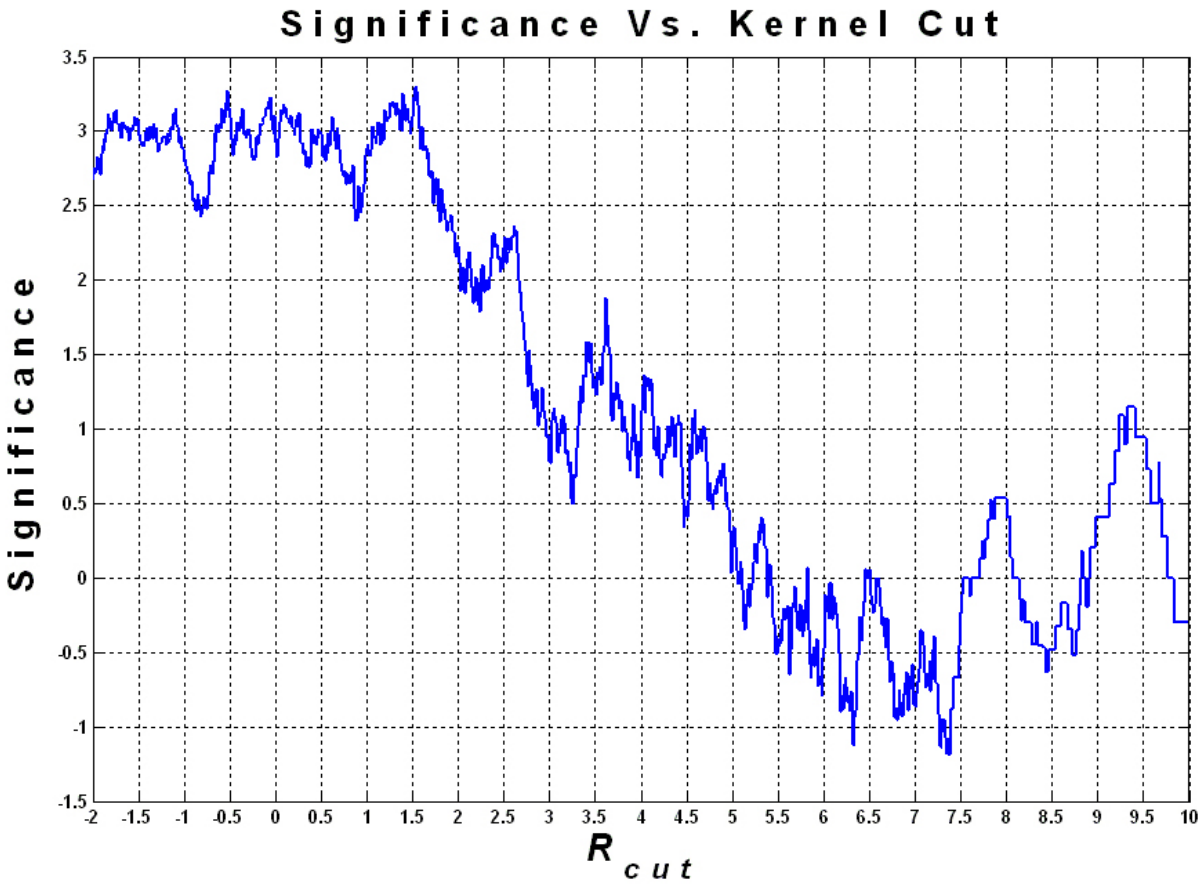

Figure 6.4: Kernel analysis of 51 IC 342 ON/OFF pairs. The kernel cut of 4.97 derived from the kernel optimisation of Crab Nebula data was chosen to generate this distribution.

As discussed above, the most reliable result is that obtained using the scaled cuts: significance 0.602 σ with nominal rate of 0.04 $\pm$ 0.06 gamma rays per minute. The flux upper limit above 600 GeV (at 99.9 % confidence) is determined to be 5.46 $\times$ 10^{-8} m^{-2} s^{-1}, corresponding to $\sim$ 8 % of the Crab Nebula flux in the same energy range.

The observations of IC 342 were motivated by the detection of diffuse TeV gamma-ray emission from the starburst galaxy NGC 253 claimed by Itoh et al. (2002) using the CANGAROO-II 10m telescope near Woomera in South Australia. That detection was reported at a significance level of $\sim$ 11 σ with a flux of (7.8 $\pm$ 2.5) $\times$ 10^{-8} m^{-2} s^{-1} at a threshold energy of 400 GeV. Such a flux level should be detectable with the Whipple 10m telescope.

IC 342 Analysis	Significance (σ)	Rate (γ-rays/minute)	Flux Upper Limit (m^{-2} s^{-1})	Flux Upper Limit ($Crab$)
Supercuts	0.276	0.027 ± 0.099	1.78×10^{-7}	13 %
Optimised Supercuts	-0.108	-0.003 ± 0.032	8.10×10^{-8}	8 %
Scaled Optimised Supercuts	0.602	0.036 ± 0.060	5.46×10^{-8}	8 %
Kernel	0.379	0.015 ± 0.041	7.47×10^{-8}	8 %

Table 6.5: All analysis results for 51 IC 342 ON/OFF pairs from the 2003 − 2004 observing season after application of Supercuts, optimised Supercuts, scaled optimised Supercuts and kernel analysis.

NGC 253 is not observable from the Whipple Observatory, so IC 342 was chosen as a suitable northern hemisphere target with very similar properties (although NGC 253 can be observed from Woomera at elevations up to 84°, leading to a lower energy threshold than for the Whipple 10m observation of IC 342). The distance to NGC 253 is 2.6 ± 0.7 Mpc; the distance to IC 342 is somewhat uncertain, but it could be as low as 1.8 Mpc. If the intrinsic level of emission from the two galaxies is similar (as might be expected since the dynamical processes and the morphology of the molecular gas in the central regions of these galaxies are almost identical (Böker et al., 1998)), the flux detected from IC 342 could actually be higher by a factor ~ 2.

Low-elevation observations of NGC 253 were carried out by the HEGRA Collaboration in 2001 but no gamma-ray emission was detected (Götting, 2006). A upper limit on the flux above 5.2 TeV of $F(> 5.2 \text{ TeV}) < 1.3 \times 10^{-9}$ photons m^{-2} s^{-1} at 99 % confidence was derived from 32.5 hours of observation, corresponding to ~ 11 % of the Crab Nebula flux. However, because of the high energy threshold of the HEGRA observations, this result is not in conflict an the extrapolation of the spectrum quoted by Itoh et al. (2002).

Unfortunately, observations of NGC 253 with the H.E.S.S. array (Aharonian

et al., 2005b) contradicted the Itoh et al. (2002) claim, giving a flux upper limits above 300 GeV of 1.9×10^{-8} photons m^{-2} s^{-1} for point-source emission and 6.3×10^{-8} photons m^{-2} s^{-1} for extended emission. Subsequent re-appraisal of the CANGAROO-II results identified errors in the analysis that invalidated the claim of a detection; later observations with the CANGAROO-III array also led to the conclusion that TeV emission from NGC 253 had not in fact been detected (Itoh et al., 2007).

More recently, VHE gamma-radiation has been detected from two starburst galaxies. The VERITAS Collaboration measured VHE emission from the galaxy M 82 with flux $F(E > 700 \text{ GeV}) = (3.7 \pm 0.8_{\text{stat}} \pm 0.7_{\text{syst}}) \times 10^{-9}$ m^{-2} s^{-1} at a significance level of 4.8 σ (Acciari et al., 2009a). This result is based on 137 hours of observation, yielding an excess of only 91 gamma-ray-like events (~ 0.7 photons per hour). The flux corresponds to ~ 0.9 % of the Crab Nebula flux for the same threshold energy. At the same time, the H.E.S.S. Collaboration presented a 5.2 σ detection of NGC 253 with an integral flux of $F(> 220 \text{ GeV}) = (5.5 \pm 1.0_{\text{stat}} \pm 2.8_{\text{syst}}) \times 10^{-9}$ m^{-2} s^{-1}, corresponding 0.3 % of the Crab Nebula flux (Acero et al., 2009). This result was based on 119 hours of observation in 2005, 2007 and 2008 with the full H.E.S.S. 4-telescope array.

In the light of the VERITAS result for M 82 and the H.E.S.S. result for NGC 253, the negative result presented here for IC 342 is hardly surprising. The measured fluxes for M 82 and NGC 253 are more than an order of magnitude lower than the original NGC 253 flux claimed by Itoh et al. (2002), and well below the sensitivity of the Whipple 10m telescope. Because of the very low fluxes, the spectral indices (assuming power-law spectra) for M 82 and NGC 253 are not well determined, but are likely be in the region of -2.5. In the case of M 82, Acciari et al. (2009a) quote an spectral index of $-2.5 \pm 0.6_{\text{stat}} \pm 0.2_{\text{syst}}$ (but note the very large errors), while for NGC 253, theoretical predictions are in the region of -2.4 (Domingo-Santamaría and Torres, 2005) to -2.7 (Paglione et al., 1996). Assuming a value of -2.5 for the spectral index, the reported fluxes can be scaled to the energy threshold of 600 GeV applicable to the IC

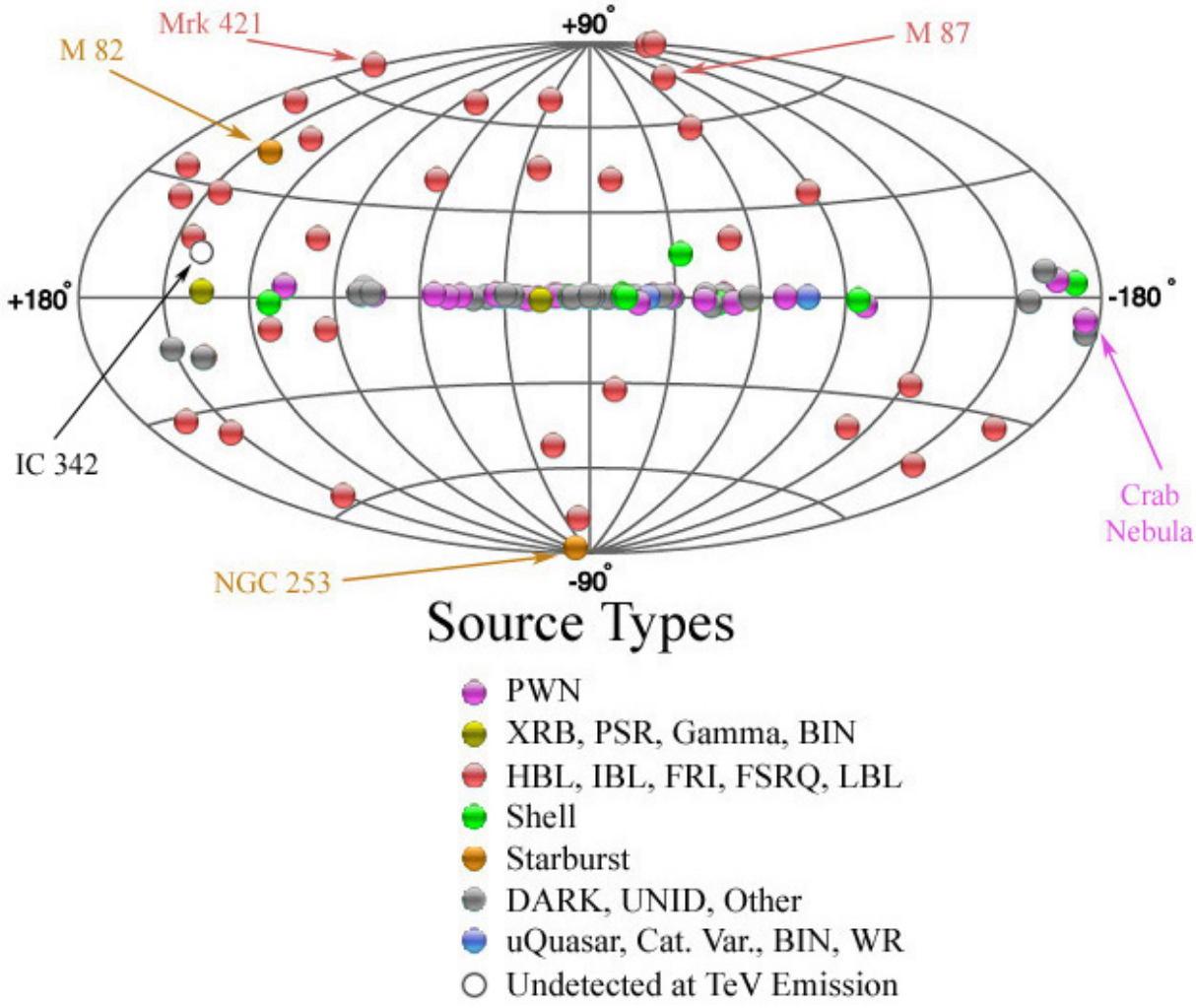

Figure 6.5: VHE γ-ray Sky Map, as of May 2010. Note that NGC 253 lies within the southern hemisphere and is unobservable with the Whipple IACT. Image adapted from http://tevcat.uchicago.edu/.

342 observations, giving $\sim 5.4 \times 10^{-9}$ m^{-2} s^{-1} for M 82 and $\sim 0.44 \times 10^{-9}$ m^{-2} s^{-1} for NGC 253. Even taking the more optimistic case of M 82, the flux is a factor of ten below the upper limit derived here for IC 342.

The VERITAS array is $\sim 8 - 10$ times more sensitive than the Whipple 10m telescope. This translates into a factor of $\sim 60 - 100$ in the time required to detect the same signal with the same significance. The VERITAS detection required 137 hours to detect M 82 at a level $\sim 5\ \sigma$. If the IC 342 flux is comparable to that of M 82, it would therefore require a minimum of perhaps

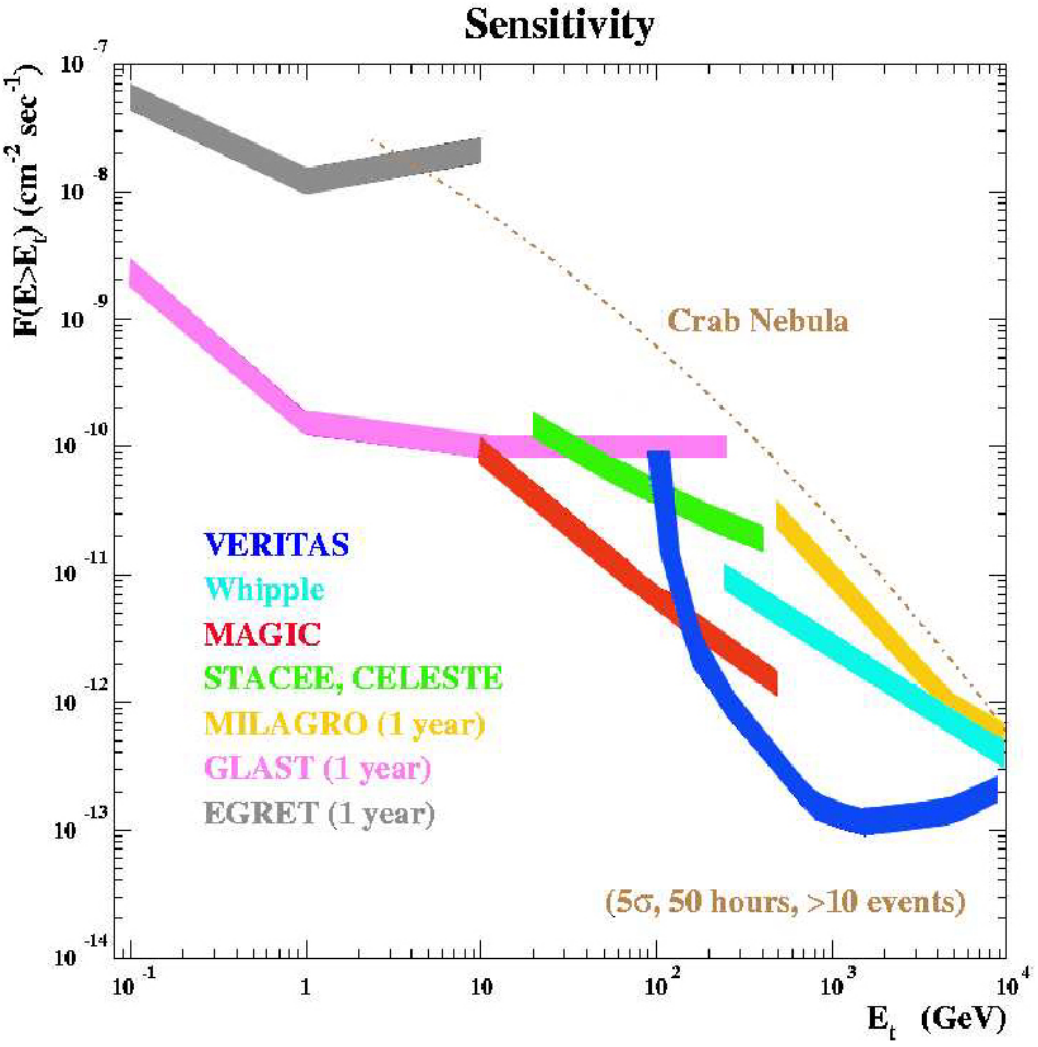

Figure 6.6: Sensitivity of next-generation gamma-ray telescopes compared to current and past experiments. The sensitivity curves are produced using Monte-Carlo simulations of VHE gamma rays and appropriate detector simulations. Indicated sensitivities assume at least 50 hours of observations and a minimum 5 σ detection with at least ten excess events recorded. Figure from Gammell (2004).

8000 hours to achieve a detection using the 10m telescope. Even if IC 342 is at a distance as low as 1.8 Mpc, compared with a distance to M 82 of $\sim$ 3.7 Mpc, the time scale for detection is still $\sim$ 2000 hours. The low elevation of IC 342 at the Whipple Observatory means that it cannot be observed for very long each year, certainly no more than 100 hours, so the time scale is completely impractical.

On the other hand, the result presented here for IC 342 is the only upper limit available for this target at TeV energies, and it is unlikely that it will be improved on in the near future. It is clear from the observations on M 82 and NGC 253 that with current atmospheric Cherenkov systems an investment of a minimum of $\sim$ 100 hours is required simply to detect such a system. With two starburst galaxies already detected, neither VERITAS nor H.E.S.S. is likely to commit such a large amount of observing time to IC 342, because a mere detection of a third starburst galaxy would not significantly improve our understanding of the mechanisms responsible for the VHE emission. Instead, the detection of IC 342 at energies above $\sim$ 500 GeV will probably have to await the development of next-generation detector systems such as CTA or AGIS.

Appendix A

Calculation of Hillas Parameters

Suppose the i^{th} PMT is given coordinates x_i, y_i (in degrees) and registers a signal s_i. The origin of the coordinate system is in the centre of the array of PMT's. An ellipse is fitted to the image and the Hillas parameters are calculated relative to the centre. For a graphical description of the Hillas parameters see Figure 5.2. The fitting of the ellipse employs the following simple moments:

$$\begin{aligned}
\langle x \rangle &= \frac{\sum s_i x_i}{\sum s_i}, \\
\langle y \rangle &= \frac{\sum s_i y_i}{\sum s_i}, \\
\langle x^2 \rangle &= \frac{\sum s_i x_i^2}{\sum s_i}, \\
\langle y^2 \rangle &= \frac{\sum s_i y^2}{\sum s_i}, \\
\langle xy \rangle &= \frac{\sum s_i x_i y_i}{\sum s_i}, \\
\langle x^3 \rangle &= \frac{\sum s_i x_i^3}{\sum s_i}, \\
\langle y^3 \rangle &= \frac{\sum s_i y_i^3}{\sum s_i}, \\
\langle x^2 y \rangle &= \frac{\sum s_i x_i^2 y_i}{\sum s_i}, \\
\langle xy^2 \rangle &= \frac{\sum s_i x_i y_i^2}{\sum s_i},
\end{aligned}$$

and

$$
\begin{aligned}
\sigma_{x^2} &= \langle x^2 \rangle - \langle x \rangle^2, \\
\sigma_{y^2} &= \langle y^2 \rangle - \langle y \rangle^2, \\
\sigma_{xy} &= \langle xy \rangle - \langle x \rangle \langle y \rangle, \\
\sigma_{x^3} &= \langle x^3 \rangle - 3\langle x \rangle \langle x^2 \rangle + 2\langle x \rangle^3, \\
\sigma_{y^3} &= \langle y^3 \rangle - 3\langle y \rangle \langle y^2 \rangle + 2\langle y \rangle^3, \\
\sigma_{x^2y} &= \langle x^2 y \rangle - 2\langle xy \rangle \langle x \rangle + 2\langle x \rangle^2 \langle y \rangle - \langle x^2 \rangle \langle y \rangle, \\
\sigma_{xy^2} &= \langle xy^2 \rangle - 2\langle xy \rangle \langle y \rangle + 2\langle x \rangle \langle y \rangle^2 - \langle x \rangle \langle y^2 \rangle,
\end{aligned}
$$

Given the following definitions:

$$
\begin{aligned}
k &= \sigma_{y^2} - \sigma_{x^2}, \\
l &= \sqrt{k^2 + 4\sigma_{xy}^2}, \\
m &= \langle y^2 \rangle - \langle x^2 \rangle, \\
n &= \sqrt{m^2 + 4\langle xy \rangle^2}, \\
u &= 1 + \frac{k}{l}, \\
v &= 2 - u,
\end{aligned}
$$

the Hillas parameters are calculated from:

$$
\begin{aligned}
\langle Size \rangle &= \sum s_i, \\
\langle Length \rangle^2 &= \frac{\sigma_{x^2} + \sigma_{y^2} + 1}{2}, \\
\langle Width \rangle^2 &= \frac{\sigma_{x^2} + \sigma_{y^2} - 1}{2}, \\
\langle Azwidth \rangle^2 &= \frac{\langle x \rangle^2 + \langle y \rangle^2 - n}{2}, \\
\langle Miss \rangle^2 &= \frac{u\langle x \rangle^2 + v\langle y \rangle^2}{2} - \frac{2\langle xy \rangle \sigma_{xy}}{l}, \\
\langle Distance \rangle^2 &= \langle x \rangle^2 + \langle y \rangle^2, \\
\langle Alpha \rangle &= \sin^{-1}\left(\frac{\langle Miss \rangle}{\langle Distance \rangle} \right),
\end{aligned}
$$

The calculation of the parameter *Asymmetry* requires the angle, ψ, between the x-axis and the major axis of the ellipse. It is convenient to define p:

$$
\begin{aligned}
\psi &= \tan^{-1}\left(\frac{(k+l)\langle y\rangle + 2\sigma_{xy}\langle x\rangle}{2\sigma_{xy}\langle y\rangle - (k-l)\langle x\rangle}\right), \\
p &= \sigma_{x^3}\cos^3\psi + 3\sigma_{x^2y}\sin\psi\cos^2\psi + 3\sigma_{xy^2}\cos\psi\sin^2\psi + \sigma_{y^3}\sin^3\psi, \\
\langle Asymmetry\rangle^3 &= \frac{p}{\langle Length\rangle}
\end{aligned}
$$

Appendix B

Data Sets

Table B.1: IC 342 data from 2003 − 2004 season.

UT Date	ON Run	OFF Run	Elevation
031020	gt025466	gt025467	48°
031021	gt025485	gt025486	49°
031022	gt025503	gt025504	52°
031023	gt025521	gt025522	50°
031023	gt025523	gt025524	53°
031024	gt025542	gt025543	52°
031024	gt025544	gt025545	54°
031025	gt025561	gt025562	45°
031025	gt025563	gt025564	49°
031025	gt025565	gt025566	52°
031025	gt025567	gt025568	54°
031025	gt025569	gt025570	53°
031025	gt025771	gt025772	50°
031026	gt025584	gt025585	45°
031026	gt025586	gt025587	49°
031029	gt025634	gt025635	51°
031118	gt025699	gt025700	48°
031118	gt025701	gt025702	51°
031119	gt025712	gt025713	45°
031119	gt025714	gt025715	50°
031119	gt025716	gt025717	53°
031120	gt025730	gt025731	42°
031120	gt025732	gt025733	47°
031121	gt025752	gt025753	49°

Table B.1 Cont'd: IC 342 data from 2003 − 2004 season.

UT Date	ON Run	OFF Run	Elevation
031122	gt025776	gt025777	51°
031123	gt025796	gt025797	44°
031123	gt025798	gt025799	49°
031123	gt025800	gt025801	52°
031124	gt025817	gt025818	47°
031124	gt025819	gt025820	51°
031127	gt025862	gt025863	50°
031127	gt025864	gt025865	53°
031127	gt025866	gt025867	54°
031128	gt025879	gt025880	51°
031130	gt025900	gt025901	53°
031201	gt025916	gt025917	51°
031218	gt025975	gt025976	49°
031219	gt025993	gt025994	52°
031219	gt025995	gt025996	53°
031226	gt026068	gt026069	53°
040113	gt026107	gt026108	53°
040118	gt026137	gt026138	52°
040118	gt026139	gt026140	54°
040119	gt026160	gt026161	53°
040119	gt026162	gt026163	54°
040210	gt026243	gt026244	53°
040310	gt026484	gt026485	46°
040315	gt026510	gt026511	43°
040316	gt026529	gt026530	43°
040318	gt026573	gt026574	43°
040321	gt026648	gt026649	41°

Table B.2: Crab Nebula data from 2003 − 2004 season.

UT Date	ON Run	OFF Run	Elevation
030204	gt023907	gt023908	76°
030206	gt023927	gt023928	66°
030220	gt023982	gt023983	80°
030322	gt024104	gt024105	64°
030323	gt024112	gt024113	63°
030324	gt024122	gt024123	63°
030325	gt024136	gt024137	61°
030326	gt024152	gt024153	60°
030327	gt024169	gt024170	59°
030328	gt024190	gt024191	59°
030926	gt025283	gt025284	58°
031001	gt025382	gt025383	70°
031021	gt025487	gt025488	50°
031022	gt025505	gt025506	63°
031023	gt025526	gt025527	77°
031024	gt025550	gt025551	76°
031026	gt025588	gt025589	52°
031120	gt025734	gt025735	51°
031120	gt025738	gt025739	68°
031120	gt025740	gt025741	78°
031121	gt025755	gt025756	52°
031121	gt025757	gt025758	65°
031121	gt025759	gt025760	75°
031121	gt025761	gt025762	80°

Table B.2 Cont'd: Crab Nebula data from 2003 − 2004 season.

UT Date	ON Run	OFF Run	Elevation
031121	gt025763	gt025764	72°
031122	gt025778	gt025779	59°
031122	gt025781	gt025782	73°
031122	gt025783	gt025784	80°
031123	gt025802	gt025803	65°
031123	gt025804	gt025805	77°
031124	gt025828	gt025829	76°
031127	gt025868	gt025869	77°
031127	gt025870	gt025871	79°
040113	gt026109	gt026110	73°
040116	gt026121	gt026122	79°
040119	gt026164	gt026165	78°
040127	gt026186	gt026187	66°
040213	gt026276	gt026277	57°
040222	gt026442	gt026443	65°
040311	gt026491	gt026492	65°
040315	gt026512	gt026513	53°

Table B.3: Mrk 421 data from 2003 − 2004 season.

UT Date	ON Run	OFF Run	Elevation
040118	gt026150	gt026151	57°
040127	gt026193	gt026194	79°
040216	gt026333	gt026334	62°
040216	gt026336	gt026337	83°
040217	gt026360	gt026361	84°
040226	gt026464	gt026465	66°
040315	gt026519	gt026520	83°
040315	gt026525	gt026526	61°
040319	gt026598	gt026599	56°
040319	gt026600	gt026601	68°
040319	gt026602	gt026603	79°
040319	gt026604	gt026605	80°
040412	gt026770	gt026771	83°
040413	gt026785	gt026786	78°
040413	gt026787	gt026788	67°
040415	gt026823	gt026824	82°
040416	gt026840	gt026841	83°
040419	gt026874	gt026875	82°
040420	gt026893	gt026894	82°
040421	gt026912	gt026913	80°
040423	gt026948	gt026949	63°
040424	gt026964	gt026965	50°

Appendix C

The VERITAS Collaboration

Member Institutions

Smithsonian Astrophysical Observatory
Purdue University, Indiana
Iowa State University
Washington University, St. Louis
University of Chicago
University of Utah
University of California, Los Angeles
McGill University, Montreal
University College Dublin
University of Leeds

Collaborators

Adler Planetarium, Chicago
Argonne National Laboratory, Illinois
Barnard College, New York
DePauw University, Indiana
Grinnell College, Iowa
University of California, Santa Cruz
University of Iowa
University of Massachussetts
Cork Institute of Technology
Galway-Mayo Institute of Technology
National University of Ireland, Galway
Associate Members

Bibliography

Abdo, A. A., Ackermann, M., Ajello, M., Atwood, W. B., Axelsson, M., Baldini, L., Ballet, J., Barbiellini, G., Bastieri, D., Bechtol, K., Bellazzini, R., Berenji, B., Bloom, E. D., Bonamente, E., Borgland, A. W., Bregeon, J., Brez, A., Brigida, M., Bruel, P., Burnett, T. H., Caliandro, G. A., Cameron, R. A., Caraveo, P. A., Casandjian, J. M., Cavazzuti, E., Cecchi, C., Celik, O., Charles, E., Chekhtman, A., Cheung, C. C., Chiang, J., Ciprini, S., Claus, R., Cohen-Tanugi, J., Conrad, J., Dermer, C. D., de Angelis, A., de Palma, F., Digel, S. W., do Couto e Silva, E., Drell, P. S., Drlica-Wagner, A., Dubois, R., Dumora, D., Farnier, C., Favuzzi, C., Fegan, S. J., Focke, W. B., Foschini, L., Frailis, M., Fukazawa, Y., Funk, S., Fusco, P., Gargano, F., Gasparrini, D., Gehrels, N., Germani, S., Giebels, B., Giglietto, N., Giordano, F., Glanzman, T., Godfrey, G., Grenier, I. A., Grondin, M.-H., Grove, J. E., Guillemot, L., Guiriec, S., Hanabata, Y., Harding, A. K., Hayashida, M., Hays, E., Hughes, R. E., Jóhannesson, G., Johnson, A. S., Johnson, R. P., Johnson, W. N., Kamae, T., Katagiri, H., Kataoka, J., Kawai, N., Kerr, M., Knödlseder, J., Kocian, M. L., Kuss, M., Lande, J., Latronico, L., Lemoine-Goumard, M., Longo, F., Loparco, F., Lott, B., Lovellette, M. N., Lubrano, P., Madejski, G. M., Makeev, A., Mazziotta, M. N., McConville, W., McEnery, J. E., Meurer, C., Michelson, P. F., Mitthumsiri, W., Mizuno, T., Moiseev, A. A., Monte, C., Monzani, M. E., Morselli, A., Moskalenko, I. V., Murgia, S., Nakamori, T., Nolan, P. L., Norris, J. P., Nuss, E., Ohsugi, T., Omodei, N., Orlando, E., Ormes, J. F., Ozaki, M., Paneque, D., Panetta, J. H., Parent, D., Pelassa, V., Pepe, M., Pesce-Rollins, M., Piron, F., Porter, T. A., Rainò, S., Rando, R., Razzano, M., Reimer, A., Reimer, O., Reposeur,

T., Ritz, S., Rodriguez, A. Y., Romani, R. W., Roth, M., Ryde, F., Sadrozinski, H. F.-W., Sander, A., Saz Parkinson, P. M., Scargle, J. D., Sellerholm, A., Sgrò, C., Shaw, M. S., Smith, D. A., Smith, P. D., Spandre, G., Spinelli, P., Strickman, M. S., Strong, A. W., Suson, D. J., Takahashi, H., Tanaka, T., Thayer, J. B., Thayer, J. G., Thompson, D. J., Tibaldo, L., Tibolla, O., Torres, D. F., Tosti, G., Tramacere, A., Uchiyama, Y., Usher, T. L., Vasileiou, V., Vilchez, N., Vitale, V., Waite, A. P., Wang, P., Winer, B. L., Wood, K., S., Ylinen, T. and Ziegler, M. 2010, *Astrophysical Journal Letters*, 709, L152

Acciari, V. A., Aliu, E., Arlen, T., Aune, T., Bautista, M., Beilicke, M., Benbow, W., Boltuch, D., Bradbury, S. M., Buckley, J. H., Bugaev, V., Byrum, K., Cannon, A., Celik, O., Cesarini, A., Chow, Y. C., Ciupik, L., Cogan, P., Colin, P., Cui, W., Dickherber, R., Duke, C., Fegan, S. J., Finley, J. P., Finnegan, G., Fortin, P., Fortson, L., Furniss, A., Galante, N., Gall, D., Gibbs, K., Gillanders, G. H., Godambe, S., Grube, J., Guenette, R., Gyuk, G., Hanna, D., Holder, J., Horan, D., Hui, C. M., Humensky, T. B., Imran, A., Kaaret, P., Karlsson, N., Kertzman, M., Kieda, D., Kildea, J., Konopelko, A., Krawczynski, H., Krennrich, F., Lang, M. J., LeBohec, S., Maier, G., McArthur, S., McCann, A., McCutcheon, M., Millis, J., Moriarty, P., Mukherjee, R., Nagai, T., Ong, R. A., Otte, A. N., Pandel, D., Perkins, J. S., Pizlo, F., Pohl, M., Quinn, J., Ragan, K., Reyes, L. C., Reynolds, P. T., Roache, E., Rose, H. J., Schroedter, M., Sembroski, G. H., Smith, A. W., Steele, D., Swordy, S. P., Theiling, M., Thibadeau, S., Varlotta, A., Vassiliev, V. V., Vincent, S., Wagner, R. G., Wakely, S. P., Ward, J. E., Weekes, T. C., Weinstein, A., Weisgarber, T., Williams, D. A., Wissel, S., Wood, M. and Zitzer, B. 2009a, *Nature*, 462, 770

Acciari, V. A., Aliu, E., Arlen, T., Beilicke, M., Benbow, W., Boltuch, D., Bradbury, S. M., Buckley, J. H., Bugaev, V., Byrum, K., Cannon, A., Cesarini, A., Chow, Y. C., Ciupik, L., Cogan, P., Dickherber, R., Duke, C., Ergin, T., Falcone, A., Fegan, S. J., Finley, J. P., Finnegan, G., Fortin, P., Fortson, L., Furniss, A., Gibbs, K., Gillanders, G. H., Grube, J., Guenette, R., Gyuk, G.,

Hanna, D., Holder, J., Horan, D., Hui, C. M., Humensky, T. B., Imran, A., Kaaret, P., Karlsson, N., Kertzman, M., Kieda, D., Kildea, J., Konopelko, A., Krawczynski, H., Krennrich, F., Lang, M. J., LeBohec, S., Maier, G., McCann, A., McCutcheon, M., Millis, J., Moriarty, P., Mukherjee, R., Ong, R. A., Otte, A. N., Pandel, D., Perkins, J. S., Petry, D., Pohl, M., Quinn, J., Ragan, K., Reyes, L. C., Reynolds, P. T., Rose, H. J., Schroedter, M., Sembroski, G. H., Smith, A. W., Steele, D., Theiling, M., Toner, J. A., Varlotta, A., Vassiliev, V. V., Vincent, S., Wagner, R. G., Wakely, S. P., Ward, J. E., Weekes, T. C., Weinstein, A., Weisgarber, T., Williams, D. A., Wissel, S. and Wood, M. 2009b, *Astrophysical Journal Letters*, 698, 94

Acciari, V. A., Beilicke, M., Blaylock, G., Bradbury, S. M., Buckley, J. H., Bugaev, V., Butt, Y., Byrum, K. L., Celik, O., Cesarini, A., Ciupik, L., Chow, Y. C. K., Cogan, P., Colin, P., Cui, W., Daniel, M. K., Duke, C., Ergin, T., Falcone, A. D., Fegan, S. J., Finley, J. P., Fortin, P., Fortson, L., Gall, D., Gibbs, K., Gillanders, G. H., Grube, J., Guenette, R., Hanna, D., Hays, E., Holder, J., Horan, D., Hughes, S. B., Hui, C. M., Humensky, T. B., Kaaret, P., Kieda, D., Kildea, J., Konopelko, A., Krawczynski, H., Krennrich, F., Lang, M. J., LeBohec, S., Lee, K., Maier, G., McCann, A., McCutcheon, M., Millis, J., Moriarty, P., Mukherjee, R., Nagai, T., Ong, R. A., Pandel, D., Perkins, J. S., Pizlo, F., Pohl, M., Quinn, J., Ragan, K., Reynolds, P. T., Rose, H. J., Schroedter, M., Sembroski, G. H., Smith, A. W., Steele, D., Swordy, S. P., Toner, J. A., Valcarcel, L., Vassiliev, V. V., Wagner, R. G., Wakely, S. P., Ward, J. E., Weekes, T. C., Weinstein, A., White, R. J., Williams, D. A., Wissel, S., Wood, M. and Zitzer, B. 2008, *Astrophysical Journal*, 679, 1427

Acero, F., Aharonian, F., Akhperjanian, A. G., Anton, G., Barres de Almeida, U., Bazer-Bachi, A. R., Becherini, Y., Behera, B., Bernlöhr, K., Boisson, C., Bochow, A., Bolmont, J., Borrel, V., Brucker, J., Brun, F., Brun, P., Bühler, R., Bulik, T., Büsching, I., Boutelier, T., Chadwick, P. M., Charbonnier, A., Chaves, R. C. G., Cheesebrough, A., Chounet, L.-M., Clapson,

A. C., Coignet, G., Dalton, M., Daniel, M. K., Davids, I. D., Degrange, B., Deil, C., Dickinson, H. J., Djannati-Ataï, A., Domainko, W., O'C. Drury, L., Dubois, F., Dubus, G., Dyks, J., Dyrda, M., Egberts, K., Emmanoulopoulos, D., Espigat, P., Farnier, C., Fegan, S., Feinstein, F., Fiasson, A., Förster, A., Fontaine, G., Füßling, M., Gabici, S., Gallant, Y. A., Gérard, L., Gerbig, D., Giebels, B., Glicenstein, J. F., Glück, B., Goret, P., Göring, D., Hauser, D., Hauser, M., Heinz, S., Heinzelmann, G., Henri, G., Hermann, G., Hinton, J. A., Hofmann, A., Hofmann, W., Hofverberg, P., Hoppe, S., Horns, D., Jacholkowska, A., de Jager, O. C., Jahn, C., Jung, I., Katarzyński, K., Katz, U., Kaufmann, S., Kerschhaggl, M., Khangulyan, D., Khélifi, B., Keogh, D., Klochkov, D., Kluźniak, W., Komin, N., Kosack, K., Kossakowski, R., Lamanna, G., Lenain, J.-P., Lohse, T., Marandon, V., Martineau-Huynh, O., Marcowith, A., Masbou, J., Maurin, D., McComb, T. J. L., Medina, M. C., Méhault, J., Moderski, R., Moulin, E., Naumann-Godo, M., de Naurois, M., Nedbal, D., Nekrassov, D., Nicholas, B., Niemiec, J., Nolan, S. J., Ohm, S., Olive, J.-F., de Oña Wilhelmi, E., Orford, K. J., Ostrowski, M., Panter, M., Paz Arribas, M., Pedaletti, G., Pelletier, G., Petrucci, P.-O., Pita, S., Pühlhofer, G., Punch, M., Quirrenbach, A., Raubenheimer, B. C., Raue, M., Rayner, S. M., Reimer, O., Renaud, M., Rieger, F., Ripken, J., Rob, L., Rosier-Lees, S., Rowell, G., Rudak, B., Rulten, C. B., Ruppel, J., Sahakian, V., Santangelo, A., Schlickeiser, R., Schöck, F. M., Schwanke, U., Schwarzburg, S., Schwemmer, S., Shalchi, A., Sikora, M., Skilton, J. L., Sol, H., Stawarz, L., Steenkamp, R., Stegmann, C., Stinzing, F., Superina, G., Szostek, A., Tam, P. H., Tavernet, J.-P., Terrier, R., Tibolla, O., Tluczykont, M., van Eldik, C., Vasileiadis, G., Venter, C., Venter, L., Vialle, J. P., Vincent, P., Vivier, M., Völk, H. J., Volpe, F., Wagner, S. J., Ward, M., Zdziarski, A. A. and Zech, A. 2009, *Science*, 326, 1080

AGILE Webpage 2007, http://agile.rm.iasf.cnr.it/

Aharonian, F., Akhperjanian, A. G., Aye, K.-M., Bazer-Bachi, A. R., Beilicke, M., Benbow, W., Berge, D., Berghaus, P., Bernlöhr, K., Boisson, C., Bolz, O.,

Borrel, V., Braun, I., Breitling, F., Brown, A. M., Bussons Gordo, J., Chadwick, P. M., Chounet, L.-M., Cornils, R., Costamante, L., Degrange, B., Dickinson, H. J., Djannati-Ataï, A., O'C. Drury, L., Dubus, G., Emmanoulopoulos, D., Espigat, P., Feinstein, F., Fleury, P., Fontaine, G., Fuchs, Y., Funk, S., Gallant, Y. A., Giebels, B., Gillessen, S., Glicenstein, J. F., Goret, P., Hadjichristidis, C., Hauser, M., Heinzelmann, G., Henri, G., Hermann, G., Hinton, J. A., Hofmann, W., Holleran, M., Horns, D., Jacholkowska, A., de Jager, O. C., Khélifi, B., Komin, N., Konopelko, A., Latham, I. J., Le Gallou, R., Lemière, A., Lemoine-Goumard, M., Leroy, N., Lohse, T., Marcowith, A., Martin, J.-M., Martineau-Huynh, O., Masterson, C., McComb, T. J. L., de Naurois, M., Nolan, S. J., Noutsos, A., Orford, K. J., Osborne, J. L., Ouchrif, M., Panter, M., Pelletier, G., Pita, S., Pühlhofer, G., Punch, M., Raubenheimer, B. C., Raue, M., Raux, J., Rayner, S. M., Reimer, A., Reimer, O., Ripken, J., Rob, L., Rolland, L., Rowell, G., Sahakian, V., Saugè, L., Schlenker, S., Schlickeiser, R., Schuster, C., Schwanke, U., Siewert, M., Sol, H., Spangler, D., Steenkamp, R., Stegmann, C., Tavernet, J.-P., Terrier, R., Théoret, C. G., Tluczykont, M., Vasileiadis, G., Venter, C., Vincent, P., Völk, H. J. and Wagner, S. J. 2005a, *Science*, 309, 746

Aharonian, F., Akhperjanian, A. G., Aye, K.-M., Bazer-Bachi, A. R., Beilicke, M., Benbow, W., Berge, D., Berghaus, P., Bernlöhr, K., Boisson, C., Bolz, O., Braun, I., Breitling, F., Brown, A. M., Bussons Gordo, J., Chadwick, P. M., Chounet, L.-M., Cornils, R., Costamante, L., Degrange, B., Djannati-Ataï, A., O'C. Drury, L., Dubus, G., Emmanoulopoulos, D., Espigat, P., Feinstein, F., Fleury, P., Fontaine, G., Fuchs, Y., Funk, S., Gallant, Y. A., Giebels, B., Gillessen, S., Glicenstein, J. F., Goret, P., Hadjichristidis, C., Hauser, M., Heinzelmann, G., Henri, G., Hermann, G., Hinton, J. A., Hofmann, W., Holleran, M., Horns, D., de Jager, O. C., Johnston, S., Khélifi, B., Kirk, J. G., Komin, N., Konopelko, A., Latham, I. J., Le Gallou, R., Lemière, A., Lemoine-Goumard, M., Leroy, N., Lohse, T., Martineau-Huynh, O., Marcowith, A., Masterson, C., McComb, T. J. L., de Naurois, M., Nolan, S. J.,

Noutsos, A., Orford, K. J., Osborne, J. L., Ouchrif, M., Panter, M., Pelletier, G., Pita, S., Pühlhofer, G., Punch, M., Raubenheimer, B. C., Raue, M., Raux, J., Rayner, S. M., Redondo, I., Reimer, A., Reimer, O., Ripken, J., Rob, L., Rolland, L., Rowell, G., Sahakian, V., Saugè, L., Schlenker, S., Schlickeiser, R., Schuster, C., Schwanke, U., Siewert, M., Skjæraasen, O., Sol, H., Steenkamp, R., Stegmann, C., Tavernet, J.-P., Terrier, R., Théoret, C. G., Tluczykont, M., Vasileiadis, G., Venter, C., Vincent, P., Völk, H. J. and Wagner, S. J. 2005b, *Astronomy & Astrophysics*, 442, 177

Aharonian, F., Akhperjanian, A. G., Bazer-Bachi, A. R., Behera, B., Beilicke, M., Benbow, W., Berge, D., Bernlöhr, K., Boisson, C., Bolz, O., Borrel, V., Braun, I., Brion, E., Brown, A. M., Bühler, R., Büsching, I., Boutelier, T., Carrigan, S., Chadwick, P. M., Chounet, L.-M., Coignet, G., Cornils, R., Costamante, L., Degrange, B., Dickinson, H. J., Djannati-Ataï, A., Domainko, W., O'C. Drury, L., Dubus, G., Egberts, K., Emmanoulopoulos, D., Espigat, P., Farnier, C., Feinstein, F., Fiasson , A., Förster , A., Fontaine, G., Funk, S., Funk, S., Füßling, M., Gallant, Y. A., Giebels, B., Gillessen, S., Glück, B., Goret, P., Hadjichristidis, C., Hauser, D., Hauser, M., Heinzelmann, G., Henri, G., Hermann, G., Hinton, J. A., Hofmann, A., Hofmann, W., Holleran, M., Hoppe, S., Horns, D., Jacholkowska, A., de Jager, O. C., Kendziorra, E., Kerschhaggl, M., Khélifi, B., Komin, N., Kosack, K., Lamanna, G., Latham, I. J., Le Gallou, R., Lemière, A., Lemoine-Goumard, M., Lohse, T., Martin, J. M., Martineau-Huynh, O., Marcowith, A., Masterson, C., Maurin, G., McComb, T. J. L., Moulin, E., de Naurois, M., Nedbal, D., Nolan, S. J., Noutsos, A., Olive, J.-P., Orford, K. J., Osborne, J., Panter, M., Pedaletti, G., Pelletier, G., Petrucci, P.-O., Pita, S., Pühlhofer, G., Punch, M., Ranchon, S., Raubenheimer, B. C., Raue, M., Rayner, S. M., Ripken, J., Rob, L., Rolland, L., Rosier-Lees, S., Rowell, G., Ruppel, J., Sahakian, V., Santangelo, A., Saugè, L., Schlenker, S., Schlickeiser, R., Schröder, R., Schwanke, U., Schwarzburg, S., Schwemmer, S., Shalchi, A., Sol, H., Spangler, D., Steenkamp, R., Stegmann, C., Supe-

rina, G., Tam, P. H., Tavernet, J.-P., Terrier, R., Tluczykont, M., van Eldik, C., Vasileiadis, G., Venter, C., Vialle, J. P., Vincent, P., Völk, H. J., Wagner, S. J. and Ward, M. 2007, *Astronomy & Astrophysics*, 472, 489

Aharonian, F., Akhperjanian, A. G., Bazer-Bachi, A. R., Beilicke, M., Benbow, W., Berge, D., Bernlöhr, K., Boisson, C., Bolz, O., Borrel, V., Braun, I., Breitling, F., Brown, A. M., Chadwick, P. M., Chounet, L.-M., Cornils, R., Costamante, L., Degrange, B., Dickinson, H. J., Djannati-Ataï, A., O'C. Drury, L., Dubus, G., Emmanoulopoulos, D., Espigat, P., Feinstein, F., Fontaine, G., Fuchs, Y., Funk, S., Gallant, Y. A., Giebels, B., Gillessen, S., Glicenstein, J. F., Goret, P., Hadjichristidis, C., Hauser, M., Heinzelmann, G., Henri, G., Hermann, G., Hinton, J. A., Hofmann, W., Holleran, M., Horns, D., Jacholkowska, A., de Jager, O. C., Khélifi, B., Komin, N., Konopelko, A., Latham, I. J., Le Gallou, R., Lemière, A., Lemoine-Goumard, M., Leroy, N., Lohse, T., Martin, J. M., Martineau-Huynh, O., Marcowith, A., Masterson, C., McComb, T. J. L., de Naurois, M., Nolan, S. J., Noutsos, A., Orford, K., Osborne, J. L., Ouchrif, M., Panter, M., Pelletier, G., Pita, S., Pühlhofer, G., Punch, M., Raubenheimer, B. C., Raue, M., Raux, J., Rayner, S. M., Reimer, A., Reimer, O., Ripken, J., Rob, L., Rolland, L., Rowell, G., Sahakian, V., Saugè, L., Schlenker, S., Schlickeiser, R., Schuster, C., Schwanke, U., Siewert, M., Sol, H., Spangler, D., Steenkamp, R., Stegmann, C., Tavernet, J.-P., Terrier, R., Thèoret, C. G., Tluczykont, M., Vasileiadis, G., Venter, C., Vincent, P., Völk, H. J. and Wagner, S. J. 2005c, *Astronomy & Astrophysics*, 442, 1

Aharonian, F., Akhperjanian, A. G., Bazer-Bachi, A. R., Beilicke, M., Benbow, W., Berge, D., Bernlöhr, K., Boisson, C., Bolz, O., Borrel, V., Braun, I., Brown, A. M., Bühler, R., Büsching, I., Carrigan, S., Chadwick, P. M., Chounet, L.-M., Coignet, G., Cornils, R., Costamante, L., Degrange, B., Dickinson, H. J., Djannati-Ataï, A., O'C. Drury, L., Dubus, G., Egberts, K., Emmanoulopoulos, D., Espigat, P., Feinstein, F., Ferrero, E., Fiasson, A., Fontaine, G., Funk, S., Funk, S., Füßling, M., Gallant, Y. A., Giebels, B., Gli-

censtein, J. F., Goret, P., Hadjichristidis, C., Hauser, D., Hauser, M., Heinzelmann, G., Henri, G., Hermann, G., Hinton, J. A., Hofmann, A., Hofmann, W., Holleran, M., Hoppe, S., Horns, D., Jacholkowska, A., de Jager, O. C., Kendziorra, E., Kerschhaggl, M., Khélifi, B., Komin, N., Konopelko, A., Kosack, K., Lamanna, G., Latham, I. J., Le Gallou, R., Lemière, A., Lemoine-Goumard, M., Lenain, J.-P., Lohse, T., Martin, J. M., Martineau-Huynh, O., Marcowith, A., Masterson, C., Maurin, G., McComb, T. J. L., Moulin, E., de Naurois, M., Nedbal, D., Nolan, S. J., Noutsos, A., Orford, K. J., Osborne, J. L., Ouchrif, M., Panter, M., Pelletier, G., Pita, S., Pühlhofer, G., Punch, M., Ranchon, S., Raubenheimer, B. C., Raue, M., Rayner, S. M., Reimer, A., Ripken, J., Rob, L., Rolland, L., Rosier-Lees, S., Rowell, G., Sahakian, V., Santangelo, A., Saugè, L., Schlenker, S., Schlickeiser, R., Schröder, R., Schwanke, U., Schwarzburg, S., Schwemmer, S., Shalchi, A., Sol, H., Spangler, D., Spanier, F., Steenkamp, R., Stegmann, C., Superina, G., Tam, P. H., Tavernet, J.-P., Terrier, R., Tluczykont, M., van Eldik, C., Vasileiadis, G., Venter, C., Vialle, J. P., Vincent, P., Völk, H. J., Wagner, S. J. and Ward, M. 2006b, *Science*, 314, 1424

Aharonian, F., Akhperjanian, A. G., Bazer-Bachi, A. R., Beilicke, M., Benbow, W., Berge, D., Bernlöhr, K., Boisson, C., Bolz, O., Borrel, V., Braun, I., Brown, A. M., Bühler, R., Büsching, I., Carrigan, S., Chadwick, P. M., Chounet, L.-M., Cornils, R., Costamante, L., Degrange, B., Dickinson, H. J., Djannati-Ataï, A., O'C. Drury, L., Dubus, G., Egberts, K., Emmanoulopoulos, D., Espigat, P., Feinstein, F., Ferrero, E., Fiasson, A., Fontaine, G., Funk, S., Funk, S., Füßling, M., Gallant, Y. A., Giebels, B., Glicenstein, J. F., Goret, P., Hadjichristidis, C., Hauser, D., Hauser, M., Heinzelmann, G., Henri, G., Hermann, G., Hinton, J. A., Hofmann, A., Hofmann, W., Holleran, M., Horns, D., Jacholkowska, A., de Jager, O. C., Kendziorra, E., Khélifi, B., Komin, N., Konopelko, A., Kosack, K., Latham, I., Le Gallou, R., Lemière, A., Lemoine-Goumard, M., Lohse, T., Martin, J. M., Martineau-Huynh, O., Marcowith, A., Masterson, C., Maurin, G., McComb, T. J. L., Moulin, E., de

Naurois, M., Nedbal, D., Nolan, S. J., Noutsos, A., Orford, K. J., Osborne, J. L., Ouchrif, M., Panter, M., Pelletier, G., Pita, S., Pühlhofer, G., Punch, M., Raubenheimer, B. C., Raue, M., Rayner, S. M., Reimer, A., Reimer, O., Ripken, J., Rob, L., Rolland, L., Rowell, G., Sahakian, V., Santangelo, A., Saugè, L., Schlenker, S., Schlickeiser, R., Schröder, R., Schwanke, U., Schwarzburg, S., Shalchi, A., Sol, H., Spangler, D., Spanier, F., Steenkamp, R., Stegmann, C., Superina, G., Tavernet, J.-P., Terrier, R., Tluczykont, M., van Eldik, C., Vasileiadis, G., Venter, C., Vincent, P., Völk, H. J., Wagner, S. J. and Ward, M. 2006a, *Astronomy & Astrophysics*, 460, 743

Aharonian, F., Akhperjanian, A. G., Beilicke, M., Bernlöhr, K., Börst, H.-G., Bojahr, H., Bolz, O., Coarasa, T., Contreras, J. L., Cortina, J., Denninghoff, S., Fonseca, M. V., Girma, M., Götting, N., Heinzelmann, G., Hermann, G., Heusler, A., Hofmann, W., Horns, D., Jung, I., Kankanyan, R., Kestel, M., Kohnle, A., Konopelko, A., Kranich, D., Lampeitl, H., Lopez, M., Lorenz, E., Lucarelli, F., Mang, O., Mazin, D., Meyer, H., Mirzoyan, R., Moralejo, A., Oña-Wilhelmi, E., Panter, M., Plyasheshnikov, A., Pühlhofer, G., de los Reyes, R., Rhode, W., Ripken, J., Rowell, G., Sahakian, V., Samorski, M., Schilling, M., Siems, M., Sobzynska, D., Stamm, W., Tluczykont, M., Vitale, V., Völk, H. J., Wiedner, C. A. and Wittek, W. 2004, *Astrophysical Journal*, 614, 897

Aharonian, F., Akhperjanian, A. G., Beilicke, M., Bernlöhr, K., Börst, H.-G., Bojahr, H., Bolz, O., Coarasa, T., Contreras, J. L., Cortina, J., Denninghoff, S., Fonseca, M. V., Girma, M., Götting, N., Heinzelmann, G., Hermann, G., Heusler, A., Hofmann, W., Horns, D., Jung, I., Kankanyan, R., Kestel, M., Kohnle, A., Konopelko, A., Kornmeyer, H., Kranich, D., Lampeitl, H., Lopez, M., Lorenz, E., Lucarelli, F., Mang, O., Meyer, H., Mirzoyan, R., Moralejo, A., Oña-Wilhelmi, E., Panter, M., Plyasheshnikov, A., Pühlhofer, G., de los Reyes, R., Rhode, W., Ripken, J., Rowell, G., Sahakian, V., Samorski, M., Schilling, M., Siems, M., Sobzynska, D., Stamm, W., Tluczykont, M.,

Vitale, V., Völk, H. J., Wiedner, C. A. and Wittek, W. 2003, *Astronomy & Astrophysics*, 403, L1

Aielli, G., Bacci, C., Barone, F., Bartoli, B., Bernardini, P., Bi, X. J., Bleve, C., Branchini, P., Budano, A., Bussino, S., Calabrese Melcarne, A. K., Camarri, P., Cao, Z., Cappa, A., Cardarelli, R., Catalanotti, S., Cattaneo, C., Cavaliere, S., Celio, P., Chen, S. Z., Cheng, N., Creti, P., Cui, S. W., Dai, B. Z., D'Al Staiti, G. D., Danzengluobu, Dattoli, M., De Mitri, I., De Rosa, R., D'Ettorre Piazzoli, B., De Vincenzi, M., Di Girolamo, T., Ding, X. H., Di Sciascio, G., Feng, C. F., Zhaoyang Feng, Zhenyong Feng, Galeazzi, F., Galeotti, P., Gao, X. Y., Gargana, R., Garufi, F., Gou, Q. B., Guo, Y. Q., He, H. H., Haibing Hu, Hongbo Hu, Huang, Q., Iacovacci, M., Iuppa, R., James, I., Jia, H. Y., Labaciren, Li, H. J., Li, J. Y., Liberti, B., Liguori, G., Liu, C. Q., Liu, J., Lu, H., Mancarella, G., Mari, S. M., Marsella, G., Martello, D., Mastroianni, S., Meng, X. R., Mu, J., Ning, C. C., Palummo, L., Panareo, M., Perrone, L., Pistilli, P., Qu, X. B., Rossi, E., Ruggieri, F., Saggese, L., Salvini, P., Santonico, R., Segreto, A., Shen, P. R., Sheng, X. D., Shi, F., Stanescu, C., Surdo, A., Tan, Y. H., Vallania, P., Vernetto, S., Vigorito, C., Wang, H., Wang, Y. G., Wu, C. Y., Wu, H. R., Xu, B., Xue, L., Yang, H. T., Yang, Q. Y., Yang, X. C., Yu, G. C., Yuan, A. F., Zha, M., Zhang, H. M., Zhang, J. L., Zhang, L., Zhang, P., Zhang, X. Y., Zhang, Y., Zhaxisangzhu, Zhou, X. X., Zhu, F. R., Zhu, Q. Q. and Zizzi, G. 2009, *Astrophysical Journal*, 699, 1281

Albert, J., Aliu, E., Anderhub, H., Antoranz, P., Armada, A., Asensio, M., Baixeras, C., Barrio, J. A., Bartelt, M., Bartko, H., Bastieri, D., Bavikadi, S. R., Bednarek, W., Berger, K., Bigongiari, C., Biland, A., Bisesi, E., Bock, R. K., Bordas, P., Bosch-Ramon, V., Bretz, T., Britvitch, I., Camara, M., Carmona, E., Chilingarian, A., Ciprini, S., Coarasa, J. A., Commichau, S., Contreras, J. L., Cortina, J., Curtef, V., Danielyan, V., Dazzi, F., De Angelis, A., de los Reyes, R., De Lotto, B., Domingo-Santamaría, E., Dorner, D., Doro, M., Errando, M., Fagiolini, M., Ferenc, D., Fernández, E., Firpo,

R., Flix, J., Fonseca, M. V., Font, L., Fuchs, M., Galante, N., Garczarczyk, M., Gaug, M., Giller, M., Goebel, F., Hakobyan, D., Hayashida, M., Hengstebeck, T., Höhne, D., Hose, J., Hsu, C. C., Isar, P. G., Jacon, P., Kalekin, O., Kosyra, R., Kranich, D., Laatiaoui, M., Laille, A., Lenisa, T., Liebing, P., Lindfors, E., Lombardi, S., Longo, F., López, M., López, J., Lorenz, E., Lucarelli, F., Majumdar, P., Maneva, G., Mannheim, K., Mansutti, O., Mariotti, M., Martínez, M., Mase, K., Mazin, D., Merck, C., Meucci, M., Meyer, M., Miranda, J. M., Mirzoyan, R., Mizobuchi, S., Moralejo, A., Nilsson, K., Oña-Wilhelmi, E., Orduña, R., Otte, N., Oya, I., Paneque, D., Paoletti, R., Paredes, J. M., Pasanen, M., Pascoli, D., Pauss, F., Pavel, N., Pegna, R., Persic, M., Peruzzo, L., Piccioli, A., Poller, M., Pooley, G., Prandini, E., Raymers, A., Rhode, W., Ribó, M., Rico, J., Riegel, B., Rissi, M., Robert, A., Romero, G. E., Rügamer, S., Saggion, A., Sánchez, A., Sartori, P., Scalzotto, V., Scapin, V., Schmitt, R., Schweizer, T., Shayduk, M., Shinozaki, K., Shore, S. N., Sidro, N., Sillanpää, A., Sobczynska, D., Stamerra, A., Stark, L., Takalo, L., Temnikov, P., Tescaro, D., Teshima, M., Tonello, N., Torres, A., Torres, D. F., Turini, N., Vankov, H., Vitale, V., Wagner, R., Wibig, T., Wittek, W., Zanin, R. and Zapatero, J. 2006a, *Science*, 312, 1771

Albert, J., Aliu, E., Anderhub, H., Antoranz, P., Armada, A., Asensio, M., Baixeras, C., Barrio, J. A., Bartko, H., Bastieri, D., Bednarek, W., Berger, K., Bigongiari, C., Biland, A., Bisesi, E., Blanch, O., Bock, R. K., Bretz, T., Britvitch, I., Camara, M., Chilingarian, A., Ciprini, S., Coarasa, J. A., Commichau, S., Contreras, J. L., Cortina, J., Danielyan, V., Dazzi, F., De Angelis, A., De Lotto, B., Domingo-Santamaría, E., Dorner, D., Doro, M., Epler, O., Errando, M., Ferenc, D., Fernández, E., Firpo, R., Flix, J., Fonseca, M. V., Font, L., Galante, N., Garczarczyk, M., Gaug, M., Gebauer, J., Giller, M., Goebel, F., Hakobyan, D., Hayashida, M., Hengstebeck, T., Höhne, D., Hose, J., Jacon, P., de Jager, O. C., Kalekin, O., Kranich, D., Laille, A., Lenisa, T., Liebing, P., Lindfors, E., Longo, F., López, M., López, J., Lorenz, E., Lucarelli, F., Majumdar, P., Maneva, G., Mannheim, K., Mariotti, M.,

Martínez, M., Mase, K., Mazin, D., Merck, C., Merck, M., Meucci, M., Meyer, M., Miranda, J. M., Mirzoyan, R., Mizobuchi, S., Moralejo, A., Nilsson, K., Oña-Wilhelmi, E., Orduña, R., Otte, N., Oya, I., Paneque, D., Paoletti, R., Pasanen, M., Pascoli, D., Pauss, F., Pavel, N., Pegna, R., Peruzzo, L., Piccioli, A., Pin, M., Prandini, E., de los Reyes, R., Rico, J., Rhode, W., Riegel, B., Rissi, M., Robert, A., Rossato, G., Rügamer, S., Saggion, A., Sánchez , A., Sartori, P., Scalzotto, V., Schmitt, R., Schweizer, T., Shayduk, M., Shinozaki, K., Sidro, N., Sillanpää, A., Sobczynska, D., Stamerra, A., Stark, L., Takalo, L., Temnikov, P., Tescaro, D., Teshima, M., Tonello, N., Torres, A., Turini, N., Vankov , H., Vitale, V., Volkov, S., Wagner, R., Wibig , T., Wittek, W. and Zapatero, J. 2006b, *Astrophysical Journal*, 639, 761

Albert, J., Aliu, E., Anderhub, H., Antoranz, P., Armada, A., Baixeras, C., Barrio, J. A., Bartko, H., Bastieri, D., Becker, K., Bednarek, W., Berger, K., Bigongiari, C., Biland, A., Bock, R. K., Bordas, P., Bosch-Ramon, V., Bretz, T., Britvitch, I., Camara, M., Carmona, E., Chilingarian, A., Coarasa, J. A., Commichau, S., Contreras, J. L., Cortina, J., Costado, M. T., Curtef, V., Danielyan, V., Dazzi, F., De Angelis, A., Delgado, C., de los Reyes, R., De Lotto, B., Domingo-Santamaría, E., Dorner, D., Doro, M., Errando, M., Fagiolini, M., Ferenc, D., Fernández, E., Firpo, R., Flix, J., Fonseca, M. V., Font, L., Fuchs, M., Galante, N., García-López, R. J., Garczarczyk, M., Gaug, M., Giller, M., Goebel, F., Hakobyan, D., Hayashida, M., Hengstebeck, T., Herrero, A., Höhne, D., Hose, J., Hsu, C. C., Jacon, P., Jogler, T., Kosyra, R., Kranich, D., Kritzer, R., Laille, A., Lindfors, E., Lombardi, S., Longo, F., López, M., López, J., Lorenz, E., Majumdar, P., Maneva, G., Mannheim, K., Mansutti, O., Mariotti, M., Martínez, M., Mazin, D., Merck, C., Meucci, M., Meyer, M., Miranda, J. M., Mirzoyan, R., Mizobuchi, S., Moralejo, A., Nieto, D., Nilsson, K., Ninkovic, J., Oña-Wilhelmi, E., Otte, N., Oya, I., Panniello, M., Paoletti, R., Paredes, J. M., Pasanen, M., Pascoli, D., Pauss, F., Pegna, R., Persic, M., Peruzzo, L., Piccioli, A., Prandini, E., Puchades, N., Raymers, A., Rhode, W., Ribó, M., Rico, J., Rissi, M., Robert, A.,

Rügamer, S., Saggion, A., Saito, T., Sánchez, A., Sartori, P., Scalzotto, V., Scapin, V., Schmitt, R., Schweizer, T., Shayduk, M., Shinozaki, K., Shore, N., Sidro, N., Sillanpää, A., Sobczynska, D., Stamerra, A., Stark, L., Takalo, L., Temnikov, P., Tescaro, D., Teshima, M., Torres, D. F., Turini, N., Vankov, H., Vitale, V., Wagner, R. M., Wibig, T., Wittek, W., Zandanel, F., Zanin, R. and Zapatero, J. 2007, *Astrophysical Journal Letters*, 665, L51

Aliu, E. and The MAGIC Collaboration 2008, *Science*, 322, 1221

Amenomori, M., Ayabe, S., Chen, D., Cui, S. W., Danzengluobu, Ding, L. K., Ding, X. H., Feng, C. F., Feng, Z. Y., Gao, X. Y., Geng, Q. X., Guo, H. W., He, H. H., He, M., Hibino, K., Hotta, N., Hu, H., Hu, H. B., Huang, J., Huang, Q., Jia, H. Y., Kajino, F., Kasahara, K., Katayose, Y., Kato, C., Kawata, K., Labaciren, Le, G. M., Li, J. Y., Lu, H., Lu, S. L., Meng, X. R., Mizutani, K., Mu, J., Munakata, K., Nagai, A., Nanjo, H., Nishizawa, M., Ohnishi, M., Ohta, I., Onuma, H., Ouchi, T., Ozawa, S., Ren, J. R., Saito, T., Saito, T. Y., Sakata, M., Sasaki, T., Shibata, M., Shiomi, A., Shirai, T., Sugimoto, H., Takita, M., Tan, Y. H., Tateyama, N., Torii, S., Tsuchiya, H., Udo, S., Wang, H., Wang, X., Wang, Y. G., Wu, H. R., Xue, L., Yamamoto, Y., Yan, C. T., Yang, X. C., Yasue, S., Ye, Z. H., Yu, G. C., Yuan, A. F., Yuda, T., Zhang, H. M., Zhang, J. L., Zhang, N. J., Zhang, X. Y., Zhang, Y., Zhang, Y., Zhaxisangzhu, Zhou, X. X. and The Tibet ASγ Collaboration 2005, *Astrophysical Journal*, 635, L53

Andringa, S. and The Pierre Auger Collaboration 2010, To appear in the Conference proceedings Rencontres de Moriond 2010 *(electroweak)*

Asai, K., Dotani, T., Nagase, F. and Mitsuda, K. 2000, *Astrophysical Journal Supplement Series*, 131, 571

Atkins, R., Benbow, W., Berley, D., Blaufuss, E., Bussons, J., Coyne, D. G., DeYoung, T., Dingus, B. L., Dorfan, D. E., Ellsworth, R. W., Fleysher, L., Fleysher, R., Gisler, G., Gonzalez, M. M., Goodman, J. A., Haines, T. J.,

Hays, E., Hoffman, C. M., Kelley, L. A., Lansdell, C. P., a. L. J. T., McEnery, J. E., Miller, R. S., Mincer, A. I., Morales, M. F., Nemethy, P., Noyes, D., Ryan, J. M., Samuelson, F. W., Shoup, A., Sinnis, G., Smith, A. J., Sullivan, G. W., Williams, D. A., Westerhoff, S., Wilson, M. E., Xu, X. W. and Yodh, G. B. 2004, *Astrophysical Journal*, 608, 680

Ballesteros-Paredes, J., Klessen, R. S., MacLow, M. M. and Vazquez-Semadeni, E. 2006, in *Protostars & Planets V*, Part I, 63

Bauer, F. E., Brandt, W. N. and Lehmer, B. 2003, *Astronomical Journal*, 126, 2797

Becklin, E. E., Gatley, I., Matthews, K., Neugebauer, G., Sellgren, K., Werner, M. W. and Wynn-Williams, C. G. 1980, *Astrophysical Journal*, 236, 441

Beckmann, V., Soldi, S., Shrader, C. R. and Gehrels, N. 2005, *Astrophysical Journal*, 638, 642

Berry, D. 1995, *Sky & Telescope*, September, p.20

Bhattacharya, D., The, L. S., Kurfess, J. D., Clayton, D. D., Gehrels, N., Leising, M. D., Grabelsky, D. A., Johnson, W. N., Jung, G. V., Kinzer, R. L., Purcell, W. R., Strickman, M. S. and Ulmer, M. P. 1994, *Astrophysical Journal*, 437, 173

Biermann, P. L. and Strittmatter, P. A. 1987, *Astrophysical Journal*, 322, 643

Bigongiari, C. 2005, Proceedings of HEP2005 International Europhysics Conference on High Energy Physics, 21^{st} – 27^{th} July 2005, Lisboa, Portugal, *Proceedings of Science*, PoS(HEP2005)020/1, eds. T. Akesson, R. Barlow, G. Barreira (chairman), C. Berger, J. Bernabeu, H. Burkhardt, B. Foster, M.C.E. Huber, K. Hubner, D. Lee, R. Leitner, P. Levai, F. Linde, P. Osland, F. Pauss, S. Pokorski, E. Rabinovici, P. Sphicas, J. Tuominiemi, P. Vilain, D. Wark, N. Wermes, J. Wess, G. Wormser and F. Zwirner,

Blitz, L. and Williams, J. P. 1999, Proceedings of the Second Crete Conference "The Physics of Star Formation and Early Stellar Evolution", eds. C.L. Lada and N.D. Kylafis, *NATO Science Series C: Mathematical and Phisical Sciences*, 540, 3

Blom, J. J., Paglione, T. A. and Carramiñana, A. 1999, *Astrophysical Journal*, 516, 744

Böker, T., Förster-Schreiber, N. M. and Genzel, R. 1997, *Astronomical Journal*, 114, 1883

Böker, T., Krabbe, A. and Storey, J. W. V. 1998, *Astrophysical Journal Letters*, 498, L115

Böker, T., van der Marel, R. P. and Vacca, W. D. 1999, *Astronomical Journal*, 118, 831

Booth, C. M., Theuns, T. and Okamoto, T. 2007, *Monthly Notices of the Royal Astronomical Society*, 376, 1588

Bregman, J. N., Cox, C. and Tomisakam, K. 1993, *Astronomical Journal*, 415, L79

Brion, E. 2004, *Proceedings of the 22nd Texas Symposium on Relativistic Astrophysics,* 13$^{\rm th}$ − 17$^{\rm th}$ December 2004, Stanford University, USA, eds. P. Chen, E. Bloom, G. Madejski and V. Patrosian, eConf C041213, 2406, 1

Burrows, D. N., Hill, J. E., Chincarini, G., Tagliaferri, G., Campana, S., Moretti, A., Romano, P., Malesani, D., Racusin, J. L., Kobayashi, S., Zhang, B., Mészáros, P., O'Brien, P. T., Willingale, R., Osborne, J. P., Cusumano, G., Giommi, P., Angelini, L., Abbey, A. F., Angelo Antonelli, L., Beardmore, A. P., Capalbi, M., Covino, S., D'Avanzo, P., Goad, M. R., Kennea, J. A., Morris, D. C., Pagani, C., Page, K. L., Stella, L., Nousek, J. A., Wells, A. A. and Gehrels, N. 2005, *Astrophysical Journal*, 622, L85

Buta, R. J. and McCall, M. L. 1999, *Astrophysical Journal Supplement Series*, 124, 33

Carilli, C. L. 1996, *Astronomy & Astrophysics*, 305, 402

Carson, J. E., Kildea, J., Ong, R. A., Ball, J., Bramel, D. A., Covault, C. E., Driscoll, D., Fortin, P., Gingrich, D. M., Hanna, D. S., Lindner, T., Mueller, C., Jarvis, A., Mukherjee, R., Ragan, K., Scalzo, R. A., Williams, D. A. and Zweerink, J. 2007, *Astrophysical Journal*, 662, 199

Carter-Lewis, D. 1992, Whipple Collaboration Internal Memo

Cawley, M. F., Fegan, D. J., Harris, K., Hillas, A. M., Kwok, P. W., Lamb, R. C., Lang, M. J., Lewis, D. A., Macomb, D., Reynolds, P. T., Schmid, D. J., Vacanti, G. and Weekes, T. C. 1990, *Experimental Astronomy*, 1, 173

CERN Webpage 2010, *Press Release,* http://public.web.cern.ch/press/pressreleases /Releases2010/PR07.10E.html

Chen, A., Reyes, L. C. and Ritz, S. 2004, *Astrophysical Journal*, 608, 686

Cheng, K. S., Ho, C. and Ruderman, M. A. 1986, *Astrophysical Journal*, 300, 500

Cillis, A. N., Torres, D. F. and Reimer, O. 2005, *Astrophysical Journal*, 621, 139

Cogan, P. 2006, Ph.D. thesis, University College Dublin, Ireland

Cogan, P. and the VERITAS Collaboration 2004, Proceedings of conference "The Multiwavelength Approach to Unidentified Sources", *Astrophysics and Space Science*, 297, 275

Dahlem, M., Weaver, K. A. and Heckman, T. M. 1998, *Astrophysical Journal Supplement Series*, 118, 401

Dame, T. M., Hartmann, D. and P., T. 2001, *Astrophysical Journal*, 547, 792

Davies, J. M. and Cotton, E. S. 1957, *Journal of Solar Energy, Science and Engineering*, 1, 16

de Naurois, M. 2001, *AIP Conference Proceedings*, 558, 540

de Vaucouleurs, G. 1978, *Astrophysical Journal*, 224, 710

Diaz, J. R. 1995, *Sky & Telescope*, September, p.24

Dickey, J. M. and Lockman, F. J. 1990, *Annual Review of Astronomy & Astrophysics*, 28, 215

Domingo-Santamaría, E. and Torres, D. F. 2005, *Astronomy & Astrophysics*, 444, 403

Donea, A. C. and Protheroe, R. J. 2003, *Progress of Theoretical Physics Supplement*, 151, 186

Dowdall, C. 2003, M.Sc. thesis, Galway-Mayo Institute of Technology, Ireland

Dunlea, S. 2001, Ph.D. thesis, University College Dublin, Dublin, Ireland

Elmegreen, B. G. 2000, *Astrophysical Journal*, 530, 277

Engelbracht, C. W., Rieke, M. J., Rieke, G. H., a. K. D. M. and Achtermann, J. M. 1998, *Astrophysical Journal*, 505, 639

Enomoto, R., Tsuchiya, K., Adachi, Y., Kabuki, S., Edwards, P. G., Asahara, A., Bicknell, G. V., Clay, R. W., Doi, Y., Gunji, S., Hara, S., Hara, T., Hattori, T., Hayashi, S., Higashi, Y., Inoue, R., Itoh, C., Kajino, F., Katagiri, H., Kawachi, A., Kawasaki, S., Kifune, T., Kiuchi, R., Konno, K., Ksenofontov, L. T., Kubo, H., Kushida, J., Matsubara, Y., Mizumoto, Y., Mori, M., Muraishi, H., Muraki, Y., Naito, T., Nakamori, T., Nishida, D., Nishijima, K., Ohishi, M., Patterson, J. R., Protheroe, R. J., Sakamoto, Y., Sato, M., Suzuki, S., Suzuki, T., Swaby, D. L., Tanimori, T., Tanimura, H., Thornton, G. J., Watanabe, S., Yamaoka, T., Yamazaki, M., Yanagita, S., Yoshida,

T., Yoshikoshi, T., Yuasa, M. and Yukawa, Y. 2006, *Astrophysical Journal*, 638, 397

Fabbiano, G. and Trinchieri, G. 1987, *Astrophysical Journal*, 315, 46

Feng, H. and Kaaret, P. 2008, *Astrophysical Journal*, 675, 1067

Fermi Webpage 2008, http://fermi.gsfc.nasa.gov/news/2008/

Fichtel, C. E., Hartman, R. C., Kniffen, D. A., Thompson, D. J., Bignami, G. F., Ögelman, H., Özel, M. E. and Tümer, T. 1975, *Astrophysical Journal*, 198, 163

Gammell, S. 2004, Ph.D. thesis, University College Dublin, Ireland

Gao, Y. and Solomon, P. M. 2004a, *Astrophysical Journal*, 606, 271

Gao, Y. and Solomon, P. M. 2004b, *Astrophysical Journal Supplement Series*, 152, 63

Giacconi, R., Branduardi, G., Briel, U., Epstein, A., Fabricant, D., Feigelson, E., Forman, W., Gorenstein, P., Grindlay, J., Gursky, H., Harnden, Jr., F. R., Henry, J. P., Jones, C., Kellogg, E., Koch, D., Murray, S., Schreier, E., Seward, F., Tananbaum, H., Topka, K., Van Speybroeck, L., Holt, S. S., Becker, R. H., Boldt, E. A., Serlemitsos, P. J., Clark, G., Canizares, C., Markert, T., Novick, R., Helfand, D. and Long, K. 1979, *Astrophysical Journal*, 230, 540

Gingrich, D. M., Boone, L. M., Bramel, D., Carson, J., Covault, C. E., Fortin, P., Hanna, D. S., Hinton, J. A., Jarvis, A., Kildea, J., Lindner, T., Mueller, C., Mukherjee, R., Ong, R. A., Ragan, K., Scalzo, R. A., Théoret, C. G., Williams, D. A. and Zweerink, J. A. 2005, *IEEE Transactions on Nuclear Science*, 52, 2977

Gold, T. 1968, *Nature*, 218, 731

Goldreich, P. and Julian, W. H. 1969, *Astrophysical Journal*, 157, 869

Götting, N. 2006, Ph.D. thesis, University of Hamburg, Germany

Grimm, H. J., Gilfanov, M. and Sunyaev, R. 2002, *Astronomy & Astrophysics*, 391, 923

Harding, A. K., Stern, J. V., Dyks, J. and Frackowiak, M. 2008, *Astrophysical Journal*, 680, 1378

Harris, M. J. 2002, *Journal of the British Interplanetary Society.*, 55, 383

Hartman, R. C., Bertsch, D. L., Bloom, S. D., Chen, A. W., Deines-Jones, P., Esposito, J. A., Fichtel, C. E., Friedlander, D. P., Hunter, S. D., McDonald, L. M., Sreekumar, P., Thompson, D. J., Jones, B. B., Lin, Y. C., Michelson, P. F., Nolan, P. L., Tompkins, W. F., Kanbach, G., Mayer-Hasselwander, H. A., Mücke, A., Pohl, M., Reimer, O., Kniffen, D. A., Schneid, E. J., Von Montigny, C., Mukherjee, R. and Dingus, B. L. 1999, *Astrophysical Journal*, 123, 79

Helene, O. 1983, *Nuclear Instruments & Methods*, 212, 319

Hillas, A. M. 1985, *Proceedings of the 19th International Cosmic-Ray Conference,* La Jolla, 3, 445

Hillas, A. M., Akerlof, C. W., Biller, S. D., Buckley, J. H., Carter-Lewis, D. A., Catanese, M., Cawley, M. F., Fegan, D. J., Finley, J. P., Gaidos, J. A., Krennrich, F., Lamb, R. C., Lang, M. J., Mohanty, G., Punch, M., Reynolds, P. T., Rodgers, A. J., Rose, H. J., Rovero, A. C., Schubnell, M. S., Sembroski, G. H., Vacanti, G., Weekes, T. C., West, M. and Zweerink, J. 1998, *Astrophysical Journal*, 503, 744

Hirotani, K. 2001, *Astrophysical Journal*, 549, 495

Holder, J., Atkins, R. W., Badran, H. M., Blaylock, G., Bond, I. H., Boyle, P. J., Bradbury, S. M., Buckley, J. H., Carter-Lewis, D. A., Celik, O., Chow, Y. C. K., Cogan, P., Cui, W., Daniel, M. K., de la Calle Perez, I., Dowdall, C.,

Dowkontt, P., Duke, C., Ergin, T., Falcone, A. D., Fegan, D. J., Fegan, S. J., Finley, J. P., Fortson, L., Gammell, S., Gibbs, K., Gillanders, G. H., Grube, J., Hall, J., Hanna, D., Hays, E., Horan, D., Hughes, S. B., Humensky, T. B., Kaaret, P., Kenny, G. E., Kertzmann, M., Kieda, D., Kildea, J., Knapp, J., Kosack, K., Krawczynski, H., Krennrich, F., Lang, M. J., LeBohec, S., Linton, E., Lloyd-Evans, J., Maier, G., Manseri, H., Milovanovic, A., Moriarty, P., Mukherjee, R., Nagai, T. N., Ogden, P. A., Olevitch, M., Ong, R. A., Perkins, J. S., Petry, D., Pizlo, F., Pohl, M., Power-Mooney, B., Quinn, J., Quinn, M., Ragan, K., Reynolds, P. T., Rebillot, P., Rose, H. J., Schroedter, M., Sembroski, G. H., Steele, D., Swordy, S. P., Syson, A., Valcarcel, L., Vassiliev, V. V., Wagner, R. G., Wakely, S. P., Walker, G., Weekes, T. C., White, R. J., Williams, D. A. and Zweerink, J. 2005, *Proceedings of the 29th International Cosmic-Ray Conference,* Pune, India, 5, 379

Holder, J. and The CELESTE Collaboration 2001, *AIP Conference Proceedings*, 558, 635

Holmström, L. and Sain, S. R. 1997, *Technometrics*, 39, 91

Itoh, C., Enomoto, R., Yanagita, S., Yoshida, T., Asahara, A., Bicknell, G. V., Clay, R. W., Edwards, P. G., Gunji, S., Hara, S., Hara, T., Hattori, T., Hayashi, S., Hayashi, S., Kabuki, S., Kajino, F., Katagiri, H., Kawachi, A., Kifune, T., Kubo, H., Kushida, J., Matsubara, Y., Mizumoto, Y., Mori, M., Moro, H., Muraishi, H., Muraki, Y., Naito, T., Nakase, T., Nishida, D., Nishijima, K., Okumura, K., Ohishi, M., Patterson, J. R., Protheroe, R. J., Sakurazawa, K., Swaby, D. L., Tanimori, T., Tokanai, F., Tsuchiya, K., Tsunoo, H., Uchida, T., Watanabe, A., Watanabe, S. and Yoshikoshi, T. 2002, *Astronomy & Astrophysics*, 396, L1

Itoh, C., Enomoto, R., Yanagita, S., Yoshida, T., Asahara, A., Bicknell, G. V., Clay, R. W., Edwards, P. G., Gunji, S., Hara, S., Hara, T., Hattori, T., Hayashi, S., Hayashi, S., Kabuki, S., Kajino, F., Katagiri, H., Kawachi, A., Kifune, T., Kubo, H., Kushida, J., Matsubara, Y., Mizumoto, Y., Mori,

M., Moro, H., Muraishi, H., Muraki, Y., Naito, T., Nakase, T., Nishida, D., Nishijima, K., Okumura, K., Ohishi, M., Patterson, J. R., Protheroe, R. J., Sakurazawa, K., Swaby, D. L., Tanimori, T., Tokanai, F., Tsuchiya, K., Tsunoo, H., Uchida, T., Watanabe, A., Watanabe, S. and Yoshikoshi, T. 2007, *Astronomy & Astrophysics*, 462, 67

Itoh, C., Enomoto, R., Yanagita, S., Yoshida, T., Tanimori, T., Okumura, K., Asahara, A., Bicknell, G. V., Clay, R. W., Edwards, P. G., Gunji, S., Hara, S., Hara, T., Hattori, T., Hayashi, S., Hayashi, S., Kabuki, S., Kajino, F., Katagiri, H., Kawachi, A., Kifune, T., Kubo, H., Kushida, J., Matsubara, Y., Mizumoto, Y., Mori, M., Moro, H., Muraishi, H., Muraki, Y., Naito, T., Nakase, T., Nishida, D., Nishijima, K., Ohishi, M., Patterson, J. R., Protheroe, R. J., Sakurazawa, K., Swaby, D. L., Tokanai, F., Tsuchiya, K., Tsunoo, H., Uchida, T., Watanabe, A., Watanabe, S. and Yoshikoshi, T. 2003a, *Astronomy & Astrophysics*, 402, 443

Itoh, C., Enomoto, R., Yanagita, S., Yoshida, T. and Tsuru, T. G. 2003b, *Astrophysical Journal*, 584, L65

Kaufman Bernadó, M. M. 2004, Ph.D. thesis, University of Buenos Aires, Argentina

Kertzman, M. P. and Sembroski, G. H. 1994, *Nuclear Instruments & Methods in Physics Research* Section A, 343, 629

Kong, A. K. H. 2003, *Monthly Notices of the Royal Astronomical Society*, 346, 265

Koribalski, B., Whiteoak, J. B. and Houghton, S. 1995, *Astronomy Society of Australia*, 12, 20

Krismer, M., Tully, R. B. and Gioia, I. M. 1995, *Astronomical Journal*, 110, 1584

Kubota, A., Mizuno, T., Makishima, K., Fukazawa, Y., Kotoku, J., Ohnishi, T. and Tashiro, M. 2001, *Astrophysical Journal*, 547, L119

Longo, F. 2007, *Proceedings of the 1st GLAST Symposium,* Stanford University, 6$^{\rm th}$ February, 2007, *AIP Conference Proceedings*, 921, eds. C. Meegan, P. Michelson and S. Ritz, p. 75

Lucarelli, F., Konopelko, A., Aharonian, F., Hofmann, F., Kohnle, A., Lampeitl, H. and Fonseca, V. 2003, *Astroparticle Physics*, 19, 339

Mak, D. S. Y., Pun, C. S. J. and Kong, A. K. H. 2008, *Astrophysical Journal*, 686, 995

Manchester, R. N., Johnston, S., Lyne, A. G., D'Amico, N., Bailes, M. and Nicastro, L. 1995, *Astrophysical Journal Letters*, 445, L137

Mannheim, K. 1993, *Astronomy & Astrophysics*, 269, 67

McCall, M. L. 1989, *Astronomical Journal*, 97, 1341

Meier, D. S. and Turner, J. L. 2005, *Astrophysical Journal*, 618, 259

Melnick, J. and Mirabel, I. F. 1990, *Astronomy & Astrophysics*, 231, L19

Mereghetti, S., Barbiellini, G., Budini, G., Caraveo, P., Costa, E., Cocco, V., Di Cocco, G., Feroci, M., Labanti, C., Longo, F., Morelli, E., Morselli, A., Pellizzoni, A., Perotti, F., Picozza, P., Prest, M., Soffitta, P., Soli, L., Tavani, M., Vallazza , E. and Vercellone, S. 1999, Proceedings the GeV-TeV Gamma-ray Astrophysics Workshop "Towards a Major Atmospheric Cerenkov Detector VI", Snowbird, Utah, 13$^{\rm th}$ − 16$^{\rm th}$ August, *AIP Conference Proceedings*, 515, 467

Mohan, N. R., Anantharamaiah, K. R. and Goss, W. M. 2002, *Astrophysical Journal*, 574, 701

Morales, M. 2002, Ph.D. thesis, University of California, Santa Cruz

Mori, M. and The CANGAROO Collaboration 2001, *Proceedings of the Gamma-Ray Astrophysics Symposium,* $4^{\rm th}$ – $6^{\rm th}$ April 2001, Baltimore, USA, *AIP Conference Proceedings*, 587, 927

Moriarty, P. and Samuelson, F. W. 2000, Proceedings of the GeV-TeV Gamma-ray Astrophysics Workshop "Towards a Major Atmospheric Cerenkov Detector VI", Snowbird, Utah, $13^{\rm th}$ - $16^{\rm th}$ August 1999, *AIP Conference Proceedings*, 515, 338

Muslimov, A. G. and Harding, A. K. 2004, *Astrophysical Journal*, 606, 1143

Newton, K. 1980, *Monthly Notices of the Royal Astronomical Society*, 191, 169

Okada, K., Dotani, T., Makishima, K., Mitsuda, K. and Mihara, T. 1998, *Publications of the Astronomical Society of Japan*, 50, 25

Oser, S., Bhattacharya, L. M., Boone, M., Chantell, M. C., Connor, Z., Covault, C. E., Dragovan, M., Fortin, P., Gregorich, D. T., Hanna, D. S., Mukherjee, R., Ong, R. A., Ragan, K., Scalzo, R. A., Schuette, D. R., Théoret, C. G., Tümer, T. O., Williams, D. A. and Zweerink, J. 2001, *Astrophysical Journal*, 547, 949

Pacini, F. 1967, *Nature*, 216, 567

Padoan, P. and Nordlund, A. 2002, *Astrophysical Journal*, 576, 870

Padovani, P. 1997, Gamma-Ray Emitting AGN and Unified Schemes in *Very High Energy Phenomena in the Universe,* XXXII Rencontres de Moriond, Les Arcs, France, January 1997., ed. J. Than Vân Trân, Y. Giraud-Héraud p. 7

Paglione, T. A. D., Jackson, J. M. and Ishizuki, S. 1997, *Astrophysical Journal*, 484, 656

Paglione, T. A. D., Marscher, A. P., Jackson, J. M. and Bertsch, D. L. 1996, *Astrophysical Journal*, 460, 295

Paredes, J. M. 2005, *Astrophysics and Space Science*, 300:1-3, 267

Pellizzoni, A., Chen, A., Conti, M., Giuliani, A., Mereghetti, S., Tavani, M. and Vercellone, S. 2003, "High Energy Studies of Supernova Remnants and Neutron Stars" *Advances in Space Research, Proceedings of the 34th COSPAR Scientific Assembly,* E1.4, 33, 625

Persic, M., Rephaeli, Y. and Arieli, Y. 2008, *Astronomy & Astrophysics*, 486, 143

Pohl, M. 1994, *Astronomy & Astrophysics*, 287, 453

Puche, D. and Carignan, C. 1988, *Astronomical Journal*, 95, 1025

Punch, M. 1991, *22nd International Cosmic-Ray Conference,* Dublin, Ireland, 1, 464

Punch, M. and The H.E.S.S. Collaboration 2005, Proceedings of "Exploring the Cosmic Frontier Astrophysical Instruments for the 21$^{\rm st}$ Century", 18$^{\rm th}$ − 21$^{\rm st}$ May 2004, Berlin, Germany, eds. A.P. Lobanov, P.J. Diamond, C. Cesarsky and B. Leibundgut, p. 175

Quinn, J. 1997, Ph.D. thesis, University College Dublin, Ireland

Quinn, M. 2005, M.Sc. thesis, Galway-Mayo Institute of Technology, Ireland

Reynolds, P. T., Akerlof, C. W., Cawley, M. F., Chantell, M., Fegan, D. J., Hillas, A. M., Lamb, R. C., Lang, M. J., Lawrence, M. A., Lewis, D. A., Macomb, D., Meyer, D. I., Mohanty, G., O'Flaherty, K. S., Punch, P., Schubnell, M. S., Vacanti, G., Weekes, T. C. and Whitaker, T. 1993, *Astrophysical Journal*, 404, 206

Rickard, L. J. and Harvey, P. M. 1984, *Astronomical Journal*, 89, 1520

Romani, R. W. 1996, *Astrophysical Journal*, 470, 469

Rossa, J., van der Marel, R. P., Böker, T., Gerssen, J., Ho, L. C., Rix, H.-W., Shields, J. C. and Walcher, C.-J. 2006, *Astronomical Journal*, 132, 1074

Ruderman, M. A. and Sutherland, P. G. 1975, *Astrophysical Journal*, 196, 51

Sage, L. J. and Solomon, P. M. 1991, *Astrophysical Journal*, 380, 392

Saha, A., Claver, J. and Hoessel, J. G. 2002, *Astronomical Journal*, 124, 839

Sanders, D. B. and Mirabel, I. F. 1996, *Annual Review of Astronomy & Astrophysics*, 34, 749

Schinnerer, E., Böker, T. and Meier, D. S. 2003, *Astrophysical Journal*, 591, L115

Schinnerer, E., Böker, T., Meier, D. S. and Calzetti, D. 2008, *Astrophysical Journal*, 684, L21

Scott, D. W. 1992, *Multivariate Density Estimationn: Theory, Practice and Visualization*, p. 125

Seth, A., Agüeros, M., Lee, D. and Basu-Zych, A. 2008, *Astrophysical Journal*, 678, 116

Shields, J. C., Walcher, C. J., Böker, T., Ho, L. C., Rix, H.-W. and van der Marel, R. P. 2008, *Astrophysical Journal*, 682, 104

Sidro, N. and The MAGIC Collaboration 2006, *Proceedings of the VII Scientific Meeting of the Spanish Astronomical Society (SEA),* Barcelona, Spain, 12^{th} – 15^{th} September 2006, *Highlights of Spanish Astrophysics IV,* 2007, eds., F. Figuras, J.M. Girat, M. Hernanz and C. Jordi, eConf C060912

Smith, D. A., Brion, E., Britto, R., Bruel, P., Bussons Gordo, J., Dumora, D., Durand, E., Eschstruth, P., Espigat, P., Holder, J., Jacholkowska, A., Lavalle, J., Le Gallou, R., Lott, B., Manseri, H., Münz, F., Nuss, E., Piron, F., Rannot, R. C., Reposeur, T. and Sako, T. 2006, *Astronomy & Astrophysics*, 459, 453

Solomon, P. M., Rivolo, A. R., Barrett, J. and Yahil, A. 1987, *Astrophysical Journal*, 319, 730

Sreekumar, P., Bertsch, D. L., Dingus, B. L., Esposito, J., Fichtel, C. E., Hartman, R. C., Hunter, S. D., Kanbach, G., Kniffen, D. A., Lin, Y. C., Mattox, J. R., Mayer-Hasselwander, H. A., Michelson, P. F., Von Montigny, C., Nolan, P. L., Pinkau, K., Schneid, E. and Thompson, D. J. 1994, *Astrophysical Journal*, 426, 105

Strickland, D. K., Heckman, T. M., Weaver, K. A. and Dahlem, M. 2000, *Astronomical Journal*, 120, 2965

Strickland, D. K., Heckman, T. M., Weaver, K. A., Hoopes, C. G. and Dahlem, M. 2002, *Astronomical Journal*, 568, 689

Strickland, D. K. and Stevens, I. R. 2000, *Monthly Notices of the Royal Astronomical Society*, 314, 511

Sturrock, P. A. 1971, *Astrophysical Journal*, 164, 529

Sugai, H., Davies, R. I. and J., W. M. 2003, *Astrophysical Journal*, 584, L9

Swanenburg, B. N., Bennett, K., Bignami, G. F., Buccheri, R., Caraveo, P., Hermsen, W., Kanbach, G., Lichti, G. G., Masnou, J. L., Mayer-Hasselwander, H. A., Paul, J. A., Sacco, B., Scarsi, L. and Wills, R. D. 1981, *Astrophysical Journal*, 243, L69

Tanimori, T., Sakurazawa, K., Dazeley, S. A., Edwards, P. G., Hara, T., Hayami, Y., Kamei, S., Kifune, T., Konishi, T., Matsubara, Y., Matsuoka, T., Mizumoto, Y., Masaike, A., Mori, M., Muraishi, H., Muraki, Y., Naito, T., Oda, S., Ogio, S., Osaki, T., Patterson, J. R., Roberts, M. D., Rowell, G. P., Suzuki, A., Suzuki, R., Sako, T., Tamura, T., Thornton, G. J., Susukita, R., Yanagita, S., Yoshida, T. and Yoshikoshi, T. 1998, *Astrophysical Journal*, 492, L33

Tarchi, A., Henkel, C., Peck, A. B. and Menten, K. M. 2002, *Astronomy & Astrophysics*, 385, 1049

Tavani, M., Barbiellini, G., Caraveo, P., Di Pippo, S., Mereghetti, S., Morselli, A., Pellizzoni, A., Perrino, A., Picozza, P., Schiavon, P., Severoni, S., Tavecchio, F., Vacchi, A. and Vercellone, S. 1999, *Memorie della Societa Astronomica Italiana*, 70, N.1, 201

Torres, D. F. and Anchordoqui, L. A. 2004, *Reports on Progress in Physics*, 67, 1663

Torres, D. F. and Domingo-Santamaría, E. 2005, *Modern Physics Letters*, A20, 2827

Trümper, J. 1984, *Physica Scripta*, T7, 209

Turner, J. L. and Ho, P. T. P. 1985, *Astrophysical Journal*, 299, L77

Tzanavaris, P. and Georgantopoulos, I. 2007, *Astronomy & Astrophysics*, 468, 129

Ulvestad, J. S. and Antonucci, R. R. J. 1997, *Astrophysical Journal*, 488, 621

Urry, C. and Padovani, P. 1995, *Publications of the Astronomical Society of the Pacific*, 107, 803

Urry, C. M. 2004, Proceedings of "AGN Physics with the Sloan Digital Sky Survey", $27^{\rm th} - 31^{\rm st}$ July 2003, NJ, USA, *ASP Conference Series*, 311, 49, eds. G.T. Richards, P.B. Hall,

Van Bever, J. and Vanbeveren, D. 2000, *Astronomy & Astrophysics*, 358, 462

van Eldik, C. 2006, Proceedings of the $41^{\rm st}$ Rencontres de Moriond on Electroweak Interactions and Unified Theories, La Thuile, Aosta Valley, Italy, $11^{\rm th} - 18^{\rm th}$ March 2006

Very Large Array Webpage 2008, http://www.vla.nrao.edu/

Walcher, C. J., Böker, T., Charlot, S., Ho, L. C., Rix, H.-W., Rossa, J., Shields, J. C. and van der Marel, R. P. 2006, *Astrophysical Journal*, 649, 692

Weaver, K. A., Heckman, T. M., Strickland, D. K. and Dahlem, M. 2002, *Astrophysical Journal*, 576, L19

Weekes, T. C. 2003, *VHE Gamma Ray Astronomy.* IoP Series in astronomy and astrophysics, ISBN 0750306580., Institute of Physics Publishing, Bristol, U.K.

Weekes, T. C., Cawley, M. F., Fegan, D. J., Gibbs, K. G., Hillas, A. M., Kowk, P. W., Lamb, R. C., Lewis, D. A., Macomb, D., Porter, N. A., Reynolds, P. T. and Vacanti, G. 1989, *Astrophysical Journal*, 342, 379

Williams, J. P., Blitz, L. and McKee, C. F. 1999, in *Protostars & Planets IV*, University of Arizona Press, Tucson, Part I, 97

Zhang, S., Collmar, W. and Schönfelder, V. 2002, *Astronomy & Astrophysics*, 396, 923